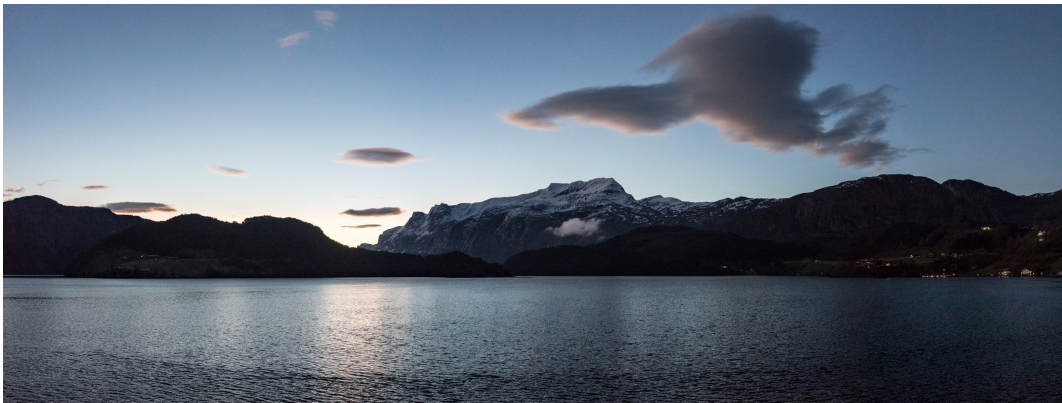


Late winter response to atmospheric and tidal forcing  
in the Førdefjord,  
inferred from mooring observations



Master's Thesis in Physical Oceanography  
Katrine Hiorth

Friday 1<sup>st</sup> June, 2018



UNIVERSITY OF BERGEN  
GEOPHYSICAL INSTITUTE

---

**Front figure** - Viewed from the northwest, the inner sill in the Førdefjord, the Ålasund, is in the centre part of the photo. Russenes is to the left, Kvammen to the right, and in the background is the mountain Heilefjell, and the peak Blægja (image courtesy of Yannick Rouven Kern).

## Abstract

The Førdefjord is a narrow fjord on the western coast of Norway. A shallow sill is situated at the Ålasund, in the centre part of the fjord. A deep basin, 3 km north of the sill, has been approved as a deposit site for mine tailings from the Engebø mountain. The late winter conditions in the Førdefjord are investigated using data from five moorings covering the period from February 3 to March 5, 2017, in addition to vertical profiles of hydrography and microstructure obtained during the deployment cruise (February 2-10, 2017). The response of the Førdefjord to atmospheric and tidal forcing is discussed, with a special focus on the sill region and the future deposit site.

The Førdefjord has a thin and fresh, dynamic surface layer with a deep, quiescent layer below. The currents in the fjord are generally weak, with the strongest currents recorded during spring tides at the surface, and near the Ålasund sill. The currents are mainly directed along the fjord. Tides dominate the current variability in the fjord, and the semidiurnal  $M_2$  tide is the dominating constituent.

In late winter, the Førdefjord is classified as a wave fjord. Semidiurnal internal tides are generated at the Ålasund sill, in addition to overtides of higher harmonics, such as the  $M_4$  and  $M_6$  tides. Synoptic sections collected across the sill show high dissipation rates and formation of hydraulic jumps, indicating occurrence of critical conditions during floods in spring tides. Northward winds together with changing stratification at the coast, were observed to lead to non-local effects into the Førdefjord, including an intermediate layer cold water intrusion. The tongue of cold water reaches the Ålasund sill region, contributing to the stratification variability in the inner fjord. The intermediate layer in the outer part of the Førdefjord is regularly ventilated during winter. Near the bottom, at the suggested deposit site, the currents are weak and directed out-fjord. However, large vertical isothermal displacements are observed during neap tides, and are consistent with an internal seiche event. Longer period observations, covering all seasons, are needed to quantify the possible effect of seiches, or the influence of sill processes on the deposit site.





## **Acknowledgments**

First of all I want to thank my supervisor, Ilker Fer, for all the motivation, guidance and helpful feedback, and believing in the thesis when I did not. I also want to thank my co-supervisor Kjersti Birkeland Daae, for always setting aside time to help and answer my questions, and for invaluable proofreading. I appreciate all the time and effort the two of you have given me and this project.

And to my fellow students, for making the last five years at GFI memorable, for all the lunch breaks, volleyball sessions, good discussions, ice cream breaks and welcomed distractions.

To my sister, Monika Hiorth, for all the encouragements and phone calls the last year.

I would also like to thank the crew and everyone on Kristine Bonnevie for a great cruise, and surprising me with a birthday cake and song. And Eivind Kolås for providing a good-looking Latex template.



# Contents

<b>Contents</b>	<b>i</b>
<b>List of Tables</b>	<b>iii</b>
<b>List of Figures</b>	<b>v</b>
<b>1 Introduction</b>	<b>1</b>
<b>2 Background</b>	<b>3</b>
2.1 Physical oceanography of fjords . . . . .	3
2.1.1 Physical forcing and fjord circulation . . . . .	4
2.1.2 Vertical mixing . . . . .	7
2.2 The Førdefjord . . . . .	9
2.2.1 Geography and social aspect . . . . .	9
2.2.2 Previous oceanographic studies in the Førdefjord . . . . .	12
<b>3 Data and Methods</b>	<b>15</b>
3.1 Moorings . . . . .	15
3.1.1 Instruments . . . . .	17
3.1.2 Mooring details . . . . .	19
3.1.3 Data preparation and data quality . . . . .	21
3.2 Hydrography measurements from ship . . . . .	21
3.3 Physical forcing . . . . .	22
3.4 Methods . . . . .	23
3.4.1 Conservative Temperature and Absolute Salinity . . . . .	23
3.4.2 Frequency spectra . . . . .	23
3.4.3 Harmonic analysis of tides . . . . .	24
3.4.4 Vertical modes . . . . .	25
3.4.5 Other . . . . .	25

<b>4</b>	<b>Physical forcing and environmental conditions</b>	<b>27</b>
4.1	Weather conditions . . . . .	27
4.2	Water level . . . . .	29
4.3	Hydrography . . . . .	29
4.3.1	Outside the Førdefjord . . . . .	29
4.3.2	Inside the Førdefjord . . . . .	30
<b>5</b>	<b>Results</b>	<b>33</b>
5.1	Hydrography . . . . .	33
5.2	Currents . . . . .	37
5.2.1	Frequency spectra . . . . .	40
5.3	Normal modes . . . . .	43
5.4	Tides . . . . .	44
5.4.1	Tidal elevation . . . . .	44
5.4.2	Tidal currents . . . . .	45
5.4.3	Residual currents . . . . .	49
5.5	Sill processes . . . . .	52
5.5.1	Froude number . . . . .	52
5.5.2	Baroclinic currents . . . . .	53
5.6	Wind-driven circulation . . . . .	56
5.6.1	Sill region . . . . .	56
5.6.2	Deposit site . . . . .	58
<b>6</b>	<b>Discussion</b>	<b>61</b>
6.1	Wind-driven circulation . . . . .	61
6.1.1	Surface wind stress . . . . .	61
6.1.2	Cold tongue intrusion . . . . .	62
6.1.3	Seiche event . . . . .	63
6.2	Tidal forcing . . . . .	64
6.2.1	Tidal currents across the Ålasund . . . . .	64
6.2.2	The barotropic tide . . . . .	65
6.2.3	The baroclinic tide . . . . .	66
6.3	Processes at the sill . . . . .	66
6.4	Processes at the deposit site . . . . .	69
<b>7</b>	<b>Conclusions</b>	<b>71</b>
<b>8</b>	<b>Bibliography</b>	<b>73</b>
	<b>Appendix</b>	<b>79</b>

# List of Tables

3.1	Mooring deployment details . . . . .	16
3.2	Technical details of instruments . . . . .	19
3.3	Instrument details on moorings F1-F5 . . . . .	20
5.1	Amplitude and phase of the main tidal constituents at F5, F1 and F4 . . . . .	44
5.2	Ellipse parameters of the barotropic tide at F5, F1 and F4 . . . . .	46



# List of Figures

2.1	Overview of external forces and physical processes in fjords . . . . .	3
2.2	Overview of the Førdefjord and surroundings . . . . .	11
3.1	Deployment positions of moorings F1-F5. . . . .	16
3.2	ADCP instrument and the Janus configuration . . . . .	18
3.3	Map of CTD casts . . . . .	22
4.1	Air temperature and air pressure from ship and the Ytterøyane Lighthouse . .	28
4.2	Wind from ship and the Ytterøyane Lighthouse . . . . .	28
4.3	Water level at the Ålasund . . . . .	29
4.4	Conservative Temperature, $\Theta$ , and Absolute Salinity, $S_A$ , depth profiles outside the Førdefjord . . . . .	30
4.5	Along-fjord transect of Conservative Temperature, $\Theta$ . . . . .	31
4.6	Cross-fjord transect of Conservative Temperature, $\Theta$ , Section H . . . . .	32
4.7	Cross-fjord transect of Conservative Temperature, $\Theta$ , Section C . . . . .	32
5.1	Conservative Temperature, $\Theta$ , depth profiles from CTD and mooring data . .	34
5.2	Absolute Salinity, $S_A$ , density, $\rho$ , and buoyancy frequency, $N$ , depth profiles from CTD data . . . . .	35
5.3	Time series of Conservative Temperature, $\Theta$ , F1-F5 . . . . .	36
5.4	Along-fjord current velocity at F1 - F5 . . . . .	38
5.5	Progressive vector diagrams at F5 . . . . .	39
5.6	Time series of wind and currents at F1 . . . . .	40
5.7	Velocity spectra for F1, F4 and F5 . . . . .	42
5.8	Horizontal modes at F1, F4 and F5 . . . . .	43
5.9	Amplitude of barotropic tidal currents across the Ålasund sill . . . . .	46
5.10	Tidal ellipses at F5 . . . . .	48
5.11	Tidal ellipses at F4 . . . . .	49
5.12	Tidal and residual currents at F5 . . . . .	50
5.13	Tidal and residual currents at F4 . . . . .	51

5.14 Froude numbers at moorings F2-F3 . . . . .	52
5.15 Baroclinic current velocities at mooring F4 . . . . .	54
5.16 Ensemble averaging of baroclinic current velocities at moorings F1 and F4 . .	56
5.17 Wind forcing at the Ålasund . . . . .	57
5.18 Vertical isothermal displacement at mooring F5 . . . . .	59
6.1 Dissipation rates at the Ålasund . . . . .	68



# 1 | Introduction

The western coast of Norway is characterized by high mountains and a coastline interrupted by long and deep fjords, carved by glaciers at the end of the last ice age. The Førdefjord is one of these fjords, located in the county of Sogn og Fjordane (see a more detailed description in Section 2.2.1, and the map in Figure 2.2). The Førdefjord is narrow (1.5 km), with a length of 50 km, running approximately east-west, with a mean depth of 200 m. The fjord has two sills, an outer sill north of Svanøy (180 m deep), and an inner sill in the Ålasund (50 m deep).

Geographic constraints, combined with external forces, such as the freshwater input, winds, tides and hydrography of the ocean outside the fjord, set the scene for the physical processes found in fjord systems (Inall and Gillibrand, 2010). The vertical mixing between fresh surface water and the saline deeper layers, lowers the overall density in the water column within the fjord. The resulting density difference between the coastal waters and the fjord, leads to a ventilation of the fjord through inflow of dense, nutrient- and oxygen-rich water, which is important for the marine life (Gade and Edwards, 1980). Vertical mixing occurs through processes such as the surface wind stress, acceleration of flow through constrictions, or through generation of internal tides at constrictions, which may transport energy toward sloping boundaries where it is available for mixing (Farmer and Freeland, 1983).

Oceanographic processes in fjords have been studied for over a century, with some of the earliest studies conducted by e.g. Ekman (1875) and Helland-Hansen (1906) in Scandinavian fjords. Notable studies within fjord oceanography, are of the Canadian fjord Knight Inlet (Freeland and Farmer, 1980), the Scottish fjord Loch Etive (Inall et al., 2004), and the Scandinavian fjords the Gullmarfjord and the Oslofjord (Gade, 1970; Saelen, 1967; Arneborg and Liljebladh, 2001a). An extensive review of the physical oceanography of fjords is given in Farmer and Freeland (1983), and a more recent review is given in Inall and Gillibrand (2010) and Stigebrandt (2012). Physical processes are sometimes easier to study in fjords than in the deep ocean, and knowledge obtained from fjords may be applied to other parts of the ocean, serving as a laboratory for oceanographic processes (Stigebrandt, 1999a).

In 2015, a Norwegian mining company (Nordic Mining) was granted permission to ex-

tract rutile from the Engebø mountain (Figure 2.2), and deposit the mine tailings in the fjord (Nordic Mining ASA, 2017). In Norway, fjords are an important part of the national identity, and the area received national, as well as international interest, due to the potential environmental impact of depositing mine tailings in the fjord (Vevring og Førdefjorden Miljøgruppe, 2016). Previous oceanographic studies in the Førdefjord are limited to reports related to the planned mining activity. This study was motivated by the effect the future depositions plans could have on marine life in the Førdefjord, with the purpose of investigating other processes that might impact the site, not included in previous studies.

This thesis investigates how the physical forcings, with an emphasize on the wind and tides, affect the fjord in late winter. The aim is to better understand the general circulation in the Førdefjord, with an emphasize on processes occurring at the sill and at the suggested deposit site. The thesis is an observational study, using a data set obtained during a student cruise I took part in, led by the Geophysical Institute at the University of Bergen, in February 2017. The seasonal focus of the study, late winter, is not set by a scientific hypothesis, but due to the time span of the related course. The data set includes vertical profiles of hydrography, current and microstructure, in addition to five bottom anchored moorings covering the period between February 3 and March 5, 2017. The focus area of the student cruise stretched from Svanøy to just east of the Ålasund (Figure 2.2). The analysis presented in this study is based on mooring data, but examples of hydrographic sections and microstructure measurements at the Ålasund sill are shown for setting the scene and for discussion purposes.

Processes generated by the interaction of the barotropic tide with the sill, or generated by local and non-local wind forcing, can potentially impact the deposit site. The processes, such as internal waves and internal seiches, may induce strong vertical mixing at the deposit site, which might cause re-suspension of the mining residual and consequently harm the marine life in the Førdefjord. Previous environmental assessments related to the mining activity, found that there would be little effects to the deposit site (Sundfjord and Bjerkeng, 2008; Endresen et al., 2014). However, these studies have mostly focused on current measurements at the deposit site, and not connected processes that occur elsewhere, e.g at the Ålasund sill or by non-local wind, to the deposit site, which is attempted in this thesis. Nevertheless, this data set has temporal and spatial limitations, and conclusions regarding the deposit site remain uncertain.

This thesis is organized as follows; Chapter 2 expands on the theoretical backdrop of fjord oceanography, with a more comprehensive description of the Førdefjord, and an overview of previous studies conducted in the fjord. Chapter 3 describes the data and methods used. The results of the study are split into two chapters, Chapter 4 is the forcing conditions which set the scene for the results obtained from the mooring record in Chapter 5. The main findings are discussed in Chapter 6, followed by a conclusion in Chapter 7.

## 2 | Background

### 2.1 Physical oceanography of fjords

A typical fjord is a deep, long and narrow inlet with the inner part of the fjord termed 'head' and the opening towards the ocean termed 'mouth' (Farmer and Freeland, 1983). The water masses in a fjord are typically characterized by a fresh surface layer and a more saline bottom layer. One or more submarine sills are common features, and typically, a shallow sill is located at the mouth, blocking a free water exchange with the open ocean. Fjords are carved by glaciers during the last ice age, and can therefore be found in mid and high latitudes (Inall and Gillibrand, 2010). Important oceanographic processes found in fjords are shown in Figure 2.1, a selection of which is summarised in the following sections.

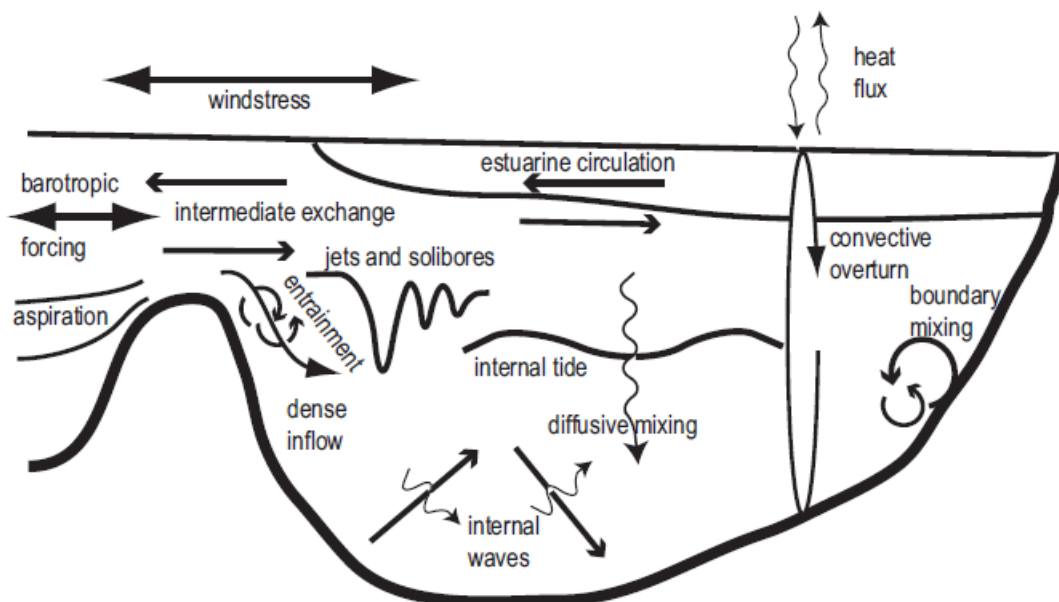


**Figure 2.1** – Overview of external forces and physical processes in fjords (Inall and Gillibrand, 2010). Freshwater runoff at the fjord head is not shown.

### 2.1.1 Physical forcing and fjord circulation

Physical processes in a fjord system are driven by external forces, such as the freshwater input, wind, tides and the hydrography and stratification of the coastal area outside the fjord (Inall and Gillibrand, 2010). The bathymetry, and thus the slope of the fjord, and the rotation of the Earth, also have an affect on certain processes. These external forces help to maintain a vertical stratification of the water column, often with three different water masses (Stigebrandt, 2012); the surface layer (a couple of meters), intermediate layer (from the base of the surface layer to the sill depth) and the deep layer (below sill depth). A fjord may contain all or some of them.

The fresh surface layer result from both precipitation and river input (Inall and Gillibrand, 2010). The main freshwater input is usually from rivers, typically at the head of the fjord. The freshwater input, together with surface heating or cooling, vertically stratifies the water column.

The orographic features of a fjord channel the wind along the fjord (Cushman-Roisin et al., 1994). The wind exerts a stress on the upper layer of the fjord, and depending on the wind strength and duration, it can initiate a surface current in the same direction. The surface current is therefore either towards the mouth (out-fjord) or the head (in-fjord), and will cause a reverse flow in the layer below, leading to an along-fjord tilt of the pycnocline (Inall and Gillibrand, 2010).

The combination of freshwater input and an along-fjord wind stress drive an estuarine circulation (Stigebrandt, 2012). The input of freshwater at the head of the fjord cause a difference in surface elevation between the mouth and the head, creating a pressure gradient and outflow of the surface layer. Wind stress leads to vertical mixing and entrainment at the interface between the surface layer and the semi-stagnant layer below. Water from the deeper layer is entrained upwards into the surface layer, decreasing the density of the water column (Gade and Edwards, 1980). To conserve volume, the water that is mixed upward must be replaced by water outside the fjord, closing the circulation.

The intermediate layer is only present in fjords with deep sills. Flow in this layer is related to the difference in stratification between the coastal water and the water in the fjord, creating horizontal pressure gradients (Stigebrandt, 2012), and is called an intermediary circulation. The effect of non-local winds can change the depth of the pycnocline at the coast through Ekman transport (Klinck et al., 1981). On the northern hemisphere the net wind-induced transport of the surface layer, induced by the wind, is to the right of the wind direction due to the rotation of the earth, called Ekman transport (Ekman, 1905; Gill, 1982; Cushman-Roisin and Beckers, 2011). A northern (southern) wind along the western coast of Norway will induce a divergence (convergence) of the surface Ekman layer at the coast which lead to a coastal upwelling (downwelling), and changes in the pycnocline

depth at the coast. The combination of vertical mixing within the fjord, and changing pycnocline depth at the coast, can cause deep water renewals, which are important for ventilating the deeper parts of the fjord. Deep water renewal occurs when dense water outside the fjord crosses the sill into the fjord (Gade, 1973; Gade and Edwards, 1980). If the water at sill depth outside the fjord is denser than water at the same depth in the fjord, the water will cross the sill. Depending on how dense the coastal water is, it may displace some or all of the water in the deeper parts of the fjord (Inall and Gillibrand, 2010). The strength of the deep water renewal is dependent on the orientation, duration and strength of the coastal and local wind, that cause changes in the pycnocline depth at the coast, and induce vertical mixing in the fjord, respectively.

Local winds and the rotation of the Earth can also cause up- and/or downwelling at the sides of a fjord if certain conditions are met (Cusman-Roisin et al., 1994). The wind needs to be sufficiently strong and/or last for a sufficient time period for upwelling to occur. Furthermore, the fjord has to be stratified and sufficiently wide, such that the width exceeds the first baroclinic radius of deformation defined by:

$$R = \frac{c_1}{f}, \quad (2.1)$$

where  $f$  is the Coriolis parameter given by:

$$f = 2\Omega \sin \phi, \quad (2.2)$$

where  $\Omega$  is the rotation rate of the Earth and  $\phi$  is latitude. And  $c_1$  is the phase speed of the first internal mode given by:

$$c_1 = \sqrt{g' H_e}, \quad (2.3)$$

where  $g'$  is the reduced gravity, and  $H_e$  is the equivalent depth, given by:

$$g' = g \frac{\rho_1 - \rho_2}{\rho_2}, \quad (2.4)$$

$$H_e = \frac{h_1 - h_2}{H}, \quad (2.5)$$

where  $h_1$  and  $h_2$  are the depth, and  $\rho_1$  and  $\rho_2$  are the density of the upper and lower layer, respectively,  $H$  is the total depth.

The Moon and the Sun's position in the sky relative to the Earth, exert gravitational forces that act on the ocean (Pugh and Woodworth, 2014). These forces are periodic and deterministic variations of surface elevation and consequently currents in the ocean. The response is due to different astronomic tidal constituents, some of the most significant are  $K_1$ ,  $M_2$ ,  $S_2$ ,  $N_2$ ,  $O_1$ , named for their origin and recurrence of the tide. In the deep, open

ocean the effect is linear and almost equal to the equilibrium tide. In coastal regions, the response is disrupted by shallow topography through bottom friction. Inside the fjord the tide will cause a periodic oscillation of the surface elevation, but the presence of a sill will reduce the amplitude of the tide and/or generate higher harmonics (Stigebrandt, 1980). Different processes occur as the barotropic tide interacts with the ocean topography, further discussed in Section 2.1.2. Noted here however, is the generation of internal waves of tidal frequencies, called internal tides, and internal tides of higher frequencies, such as multiples or sums of the dominating tidal constituents, called overtides and compound tides, respectively (Pugh and Woodworth, 2014). Overtides commonly observed in the ocean are the  $M_4$  (twice the frequency of  $M_2$ ) and  $M_6$  (thrice the frequency of  $M_2$ ). The weakest tidal currents are expected to occur at slack tide (when the tide turns), and the strongest tidal currents occur at mid-tide during flood (low to high tide) and ebb (high to low tide).

In fjords where the tidal forcing is weak, atmospheric forcing can play a more significant role in the dynamics of the fjord in the form of surface and/or internal seiches (Arneborg and Liljebladh, 2001a). A strong wind, directed in-fjord, may lead to a propagation of the barotropic and baroclinic signal toward the head. If the signal is not dampened by friction at the boundaries of the fjord, the signal is reflected at the fjord head, creating standing waves travelling in opposite directions, called seiches. In a surface seiche, the wind displaces the water toward the head of the fjord, and when the wind weakens, the surface elevation oscillates back and forth due to gravity. The length of the wave is long compared to the water depth, and the linear long-wave phase speed is given by  $\sqrt{gH}$ , where  $g$  is the gravitational acceleration and  $H$  is the depth of the basin. The surface seiche period depends on the size and depth of the basin, and is given by Merian's formula (Boegman and Ivey, 2012):

$$T = \frac{2L}{\sqrt{gH}}, \quad (2.6)$$

where  $L$  is the length of the basin. The formula assumes that the basin is a one-dimensional channel with constant depth. For internal seiches, the denominator is replaced by  $c_1$  (Equation 2.3) (Boegman and Ivey, 2012).

Seiches are found in enclosed (lakes) and semi-enclosed basins (bays, harbours, fjords). Seiches are important due to their efficiency at vertical mixing, in lakes they bring oxygen down and nutrients up, and in fjords they facilitate deep-water renewal by decreasing the density in the basin (Thorpe, 1974; Wiegand and Chamberlain, 1987; Arneborg and Liljebladh, 2001b). In fjords, the ocean takes part in the oscillations, and the fjord is only half of the seiche length, the node of the seiche is located at the mouth, and the antinode is located at the head of the fjord. The total seiche period is therefore twice the period cal-

culated from Merian's formula for a semi-enclosed basin (Leppäranta and Myrberg, 2009). If the wind duration is the same as the seiche periods or one of the natural frequencies of the internal seiche modes, given by Equation 2.6, resonance occurs, which results in large-amplitude motions (Arneborg and Liljebladh, 2001a). Internal seiches often have a larger amplitude, and a slower velocity than surface seiches, due to the weaker stratification (Wuest and Farmer, 2002). Resonance of internal seiches, and consequently an increase in amplitude, may lead to enhanced dissipation and diapycnal mixing in the basin interior, or at the boundaries which may cause sediment re-suspension (Boegman and Ivey, 2012; Arneborg and Liljebladh, 2001b).

### 2.1.2 Vertical mixing

Vertical mixing is a crucial component driving fjord circulation and ventilation of deeper layers. The water column is homogenized through vertical mixing, where heavy water is mixed upwards, and light water is mixed downwards (Inall and Gillibrand, 2010). Aside from general vertical mixing driven by winter convection or wind-induced mixing at the base of the upper mixed layer, the following theory concentrate on mixing processes near a sill and on sloping boundaries.

The velocities of tidally and/or wind driven currents increase over sills and through narrow straits. At the sill, energy can be extracted from the barotropic tide through several processes including friction against boundaries, barotropic form drag, and baroclinic wave drag (Stigebrandt, 1980). The extracted energy is then made available for vertical mixing in the fjord. The dominating process depends on the forcing conditions, the stratification and the geometry of the fjord. Investigation of these parameters give insight to what hydrodynamic processes are present at the sill, such as super or subcritical conditions relative to long internal waves, regime transitions, internal wave or jet response, and hydraulic phenomena such as hydraulic jump and lee waves.

In fjords with a shallow and long sill, energy is dissipated at the sill by friction against the boundaries (Tinis and Pond, 2001). A reduction in tidal amplitude and a phase lag is often observed across the sill, termed tidal choking (Stigebrandt, 1980). Another mechanism by which energy can be extracted from the barotropic tide, is barotropic form drag, resulting from variations in the cross-sectional area of the fjord (Stigebrandt, 1999b; Inall et al., 2004). Lastly, in deep-silled fjords the largest energy sink is usually the generation of internal tides (Stigebrandt, 1976, 1980; Freeland and Farmer, 1980; Stacey, 1984).

The Froude number,  $F$ , may indicate what processes occur at the sill (Stigebrandt, 1980; Farmer and Freeland, 1983). The Froude number is the ratio of the barotropic flow velocity to the characteristic phase speed of the internal tide, and is used to classify fjords into wave or jet fjords (Stigebrandt and Aure, 1989).



In this thesis, the densimetric Froude number is utilized:

$$F = U/c_1, \quad (2.7)$$

where  $U$  is the current speed, and  $c_1$  is the phase speed of the lowest mode internal wave (Equation 2.3).

If the Froude number is below unity, the fjord is said to be subcritical, and is classified as a wave fjord, where energy is extracted from the barotropic tide by baroclinic wave drag. For Froude numbers above unity, the fjord is supercritical and classified as a jet fjord, where energy is extracted from the barotropic tide through barotropic form drag. At criticality,  $F = 1$ , there is typically a transition from a supercritical to a subcritical condition, often accompanied by a hydraulic jump. An explanation of the characteristics of a wave and jet fjord follows in the next paragraphs.

In a wave fjord, internal waves are generated in stratified water at the sill by the barotropic tide oscillating up and down the sill every tidal cycle (Stigebrandt, 1976, 1980). The internal waves, of tidal frequencies, are called internal tides and have a characteristic phase speed given by Equation 2.3. The internal tides can either have the same frequency as the barotropic tide, or internal tides of higher harmonics can be generated. The higher harmonics have shorter wavelengths, propagate at steeper angles in the vertical, and break more easily at sloping boundaries (Inall et al., 2004). The internal tides propagate away from the sill at either side, and transport energy into the fjord. The energy is eventually dissipated by turbulence and diapycnal mixing at sloping bottoms in the fjord (Stigebrandt and Aure, 1989; Stigebrandt, 1976). The slope of the bottom topography, and the slope at which internal waves propagate, indicates whether the internal waves are reflected, amplified, or eventually dissipated as they encounter the sides of the fjord (Gemmrich and Klymak, 2015). The slope of the linear internal waves are calculated from the stratification of the water column and the forcing mechanism. Firstly, the Brunt-Vaisala frequency,  $N$ , is calculated from the stratification using Equation 2.8, and then the slope,  $\alpha$ , at which internal waves propagate is calculated using Equation 2.9.

$$N = \sqrt{-\frac{g}{\rho_0} \frac{\partial \rho}{\partial z}}, \quad (2.8)$$

where  $g$  is the gravitational acceleration,  $\rho$  is the potential density, and  $\rho_0$  is a reference density.

$$\alpha = \sqrt{\frac{\omega^2 - f^2}{N^2 - \omega^2}}, \quad (2.9)$$

where  $\omega$  is the frequency of the semidiurnal tidal component and  $f$  is the Coriolis parameter (Equation 2.2). The slope of propagation for internal waves,  $\alpha$ , is then related to the



slope of the bottom topography. If the slope of internal waves are greater (less) than the slope of the bottom topography, it is defined as a supercritical (subcritical) slope. Internal waves that encounter a subcritical slope are reflected onshore, while at supercritical slopes the internal waves are reflected back to the interior and may cause mixing in the deeper part of the fjord. When  $\alpha$  is equal to the slope of the bottom topography, the slope is critical. At these locations, the internal waves are amplified and increased mixing occurs.

In a jet fjord, topographic variations control the flow, flow accelerates through a constriction, such as a strait or a sill, followed by an expansion of the flow as the fjord widens. The accelerated flow may cause large-scale eddies separating from the mean flow and the bottom boundary, e.g a tidal jet on the leeward side of the sill (Stigebrandt, 1980). The jet may induce internal hydraulic jumps and high frequency internal waves, depending on the sill depth and thickness of the upper layer in the fjord (Farmer and Freeland, 1983). The hydraulic jump can generate internal waves of high frequencies that propagate into the fjord, called internal solitary waves (Farmer and Smith, 1978). This flow regime loses energy in the sill region, and cause high vertical mixing in the vicinity of the sill.

## 2.2 The Førdefjord

### 2.2.1 Geography and social aspect

The Førdefjord is a narrow fjord, approximately 1.5 km, running east-west on the western coast of Norway (Figure 2.2). The fjord is approximately 50 km long, and separates into two branches at the mouth, the Brufjord and the Stavfjord, running north and south of Svanøy, respectively. The mean depth is approximately 200 m, and the deepest part is located north of the Flokenes at 400 m depth. The fjord has a 180 m deep sill north of Svanøy, and a second sill, the Ålasund sill, 20 km further in-fjord, with a depth of 50 m. On each side, the fjord is flanked by mountains, where the southern side is steeper than the northern side.

Large towns surrounding the fjord are Førde, at the head of the fjord, and Naustdalen 10 km further west. Førde is the largest town and the commercial centre in the county of Sogn og Fjordane, and has around 13,000 inhabitants (Kleiven, 2017). There are other smaller villages scattered around the fjord, e.g Vevring and Kvammen close to the Ålasund.

Two major rivers have their outlet in the Førdefjord. Jølstra is at the head of the fjord, running through Førde centre, and Nausta, a protected national salmon river system, running through Naustdalen (Lesto, 2016).

The inner part of the Førdefjord, from the Ålasund and toward the head, is defined as a National Salmon fjord (Urke, 2008), i.e. no fish farming sites are allowed within that zone.

West of the Ålasund, there are currently four fish farming sites for salmon and cod; two located close to the Flokenes, one across the fjord from Vevring and one at the Russenes close to the Ålasund sill. Commercial fisheries also operate in the area, and there are several fishing grounds in the Førdefjord, for cod, pollack and tusk (Urke, 2008).

The area received national, as well as international interest, when Nordic Mining announced they intended to extract rutile from the mountain Engebø, close to Vevring (Nordic Mining ASA, 2017). Rutile is a mineral used in the production of pigment, in e.g. paint, plastic and paper, and titanium metal, used in e.g. the ship and aerospace industry. The mine tailings from the excavation will be deposited in a deep basin in the Førdefjord, close to the Engebø mountain. Environmental agencies and local organisations opposed the mining plans on the grounds that it might be harmful for the fjord biology (Vevring og Førdefjorden Miljøgruppe, 2016). Nevertheless, in 2015, Nordic Mining was granted permission by the Norwegian Ministry of Climate and Environment (Klima og Miljødepartementet, 2015), based on several scientific studies (see next section).

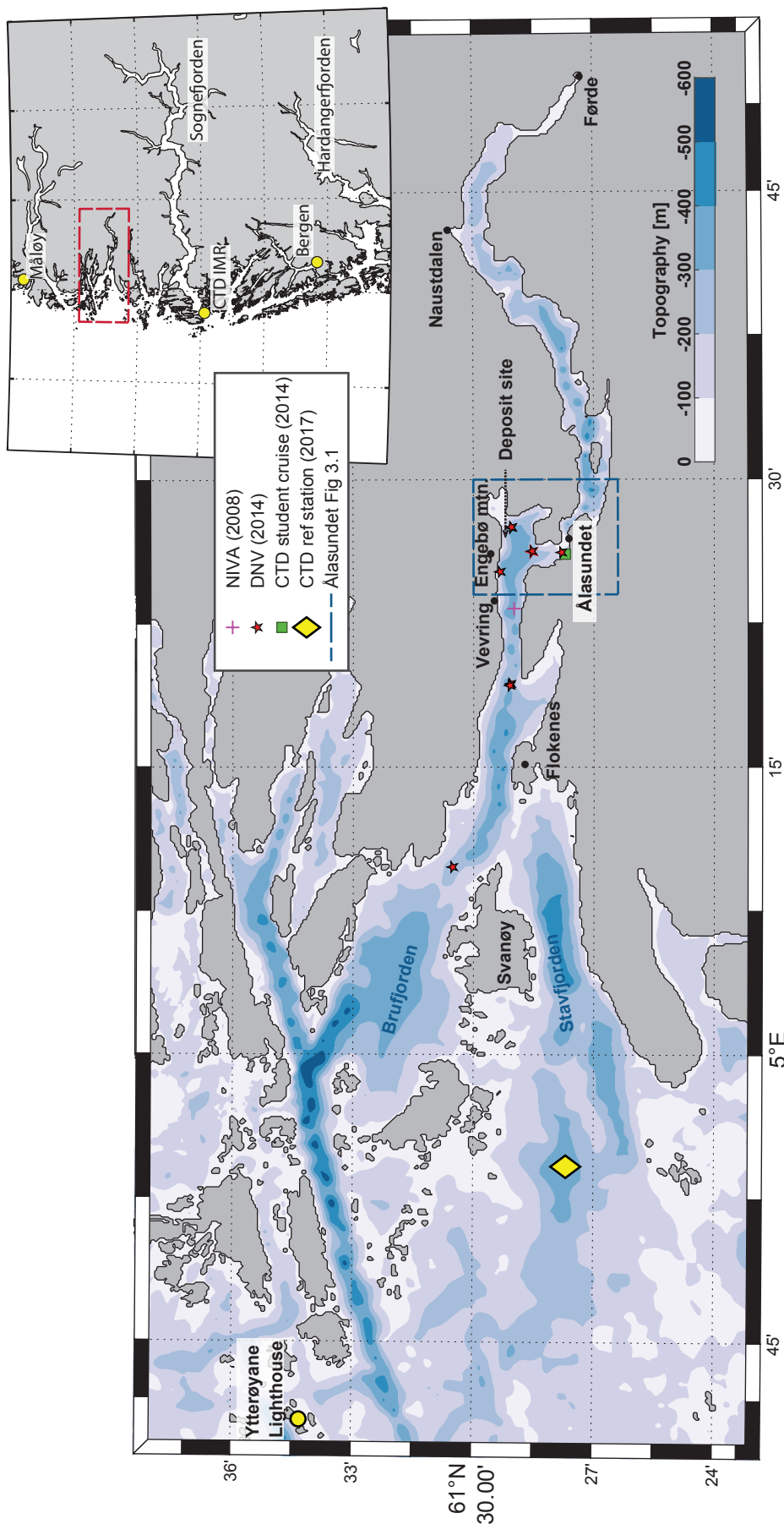


**Figure 2.2** – Overview of the Førdefjord bathymetry and surroundings. Blue shading indicates depth. Included in the map are deployed moorings and CTD stations from previous studies, as well as the meteorological station, the Ytterøyane Lighthouse, and the water level station at Måløy. The location of the CTD reference station obtained during the cruise in 2017 is also shown (yellow diamond). The blue rectangle marks the location of Figure 3.1. The inset map shows the location of the fjord on the west coast of Norway (indicated by a red, dashed line), north of Bergen and the Sognefjord.

### 2.2.2 Previous oceanographic studies in the Førdefjord

Previous oceanographic studies in the Førdefjord are limited to reports related to the planned mining activity and an earlier student cruise led by the Geophysical Institute at the University of Bergen in 2014. The Norwegian Institute for Water Research (NIVA) and Det Norske Veritas (DNV) have, on behalf of Nordic Mining, undergone several environmental impact assessments of the fjord (Sundfjord and Bjerkgeng, 2008; Endresen et al., 2014). The reports concluded that the currents in the fjord are sufficiently weak at the deposit site, and that re-suspension of the mining residual will not be a problem.

The first study in the area was conducted by NIVA in 2007 and 2008 (Sundfjord and Bjerkgeng, 2008). They measured currents, turbidity, hydrography and oxygen concentration. Current measurements covered three month-long periods, September 2007, March 2008 and May 2008, from one mooring located in the deep basin close to the mining site (Figure 2.2). The mooring measured at two depths, 335 m (close to the bottom) and 305 m. Vertical profiles of salinity, temperature, oxygen and turbidity were obtained before and after the deployment of the mooring. Current measurements showed that the semidiurnal tide dominated. The average current velocity varied between 1.6 and 3.5  $\text{cm s}^{-1}$ , directed along-fjord, the strongest occurred in March, with a maximum velocity of 13  $\text{cm s}^{-1}$ . In September, the current was directed in-fjord at 335 m and out-fjord at 305 m. The current was directed out-fjord at both depths in March and in-fjord in May. The salinity and temperature measurements showed little variation in the deeper parts of the fjord. During spring, a deep-water renewal most likely occurred, which caused a substantial movement of water masses upward. The oxygen level in the deep basin had 60 - 90% saturation, which indicated that such overturning of the deep water occurred regularly.

In 2010 and 2011, the Norwegian Institute of Marine Research (IMR) studied spawning grounds for cod in the Førdefjord (van der Meeren and Otterå, 2011). In several reports and letters following these cruises, IMR pointed out that the measurements obtained by Sundfjord and Bjerkgeng (2008) were not sufficient to conclude how a deposit site would affect the fjord. Their main objection was that Sundfjord and Bjerkgeng (2008) delivered apparent knowledge-based conclusions when the uncertainties were too high. van der Meeren and Otterå (2011) criticised the assessment on lack of emphasis on the potential spreading of the smallest particles and how this might harm the fish and ecosystem. They also pointed out that the measurement period was too short to resolve the seasonal variations. Based on this, the Norwegian Environment Agency demanded more extensive current measurements and modelling of the potential spreading of finer particles in the fjord.

This led to the second environmental impact assessment in 2014, conducted by DNV on behalf of Nordic Mining (Endresen et al., 2014). The study period covered a full year from July 2013 to June 2014, with in-situ measurements of currents, temperature and salin-

ity. DNV deployed six current meter moorings between the Ålasund and the outer part of the Førdefjord, four of which had two instruments at different depths (Figure 2.2). Towards June 2014, a seventh mooring was deployed at the suggested deposit site. In addition, 11 CTD (Conductivity, Temperature, Depth) stations were sampled seven times during the year. The current measurements showed a seasonal change, with periods of layered flow. At the suggested deposit site velocities of  $3 - 7 \text{ cm s}^{-1}$  were recorded at 200 – 300 m depth, which is slightly higher than what Sundfjord and Bjerkeng (2008) recorded at 305 – 335 m. During the year, the upper and middle part of the water column were regularly replaced, but a full deep water renewal was only observed during spring. The residual current in the fjord was weak, and DNV conclude that the tides were the dominating driver in the fjord. The report also included a model of the currents in the fjord, and potential dispersion of the mining waste from the deposit site. The current model, SINMOD developed by SINTEF (SINTEF, 2017), is a high resolution model, used together with in-situ measurements for validation. The model showed that internal tides could be substantial in the Førdefjord. The current data from SINMOD was implemented in the dispersion model DREAM (Dose related Risk and Effect Assessment Model). The results showed that particles would be carried toward west most of the year, except between April and June when they would be transported southeast. The particles would not spread vertically, and deposition of mining waste above  $6 \text{ mm yr}^{-1}$  would only happen within 1 km of the site. The model results for future scenarios (after 25 and 50 yrs), showed an increase in dispersion of particles. DNV therefore concluded that moving the deposition point after some time should be considered.

Besides the above mentioned research conducted on behalf of Nordic Mining and IMR, the Geophysical Institute at UiB conducted a student cruise in the area in 2014. The cruise was part of a field course in physical oceanography, GEOF332 (GEOF332 Students, 2014). The fieldwork took place between January 31st and February 5th, 2014 and data measurements include several CTD stations and one mooring (Figure 2.2). Note that this is not the student cruise and field work conducted in 2017, used in this study.



## 3 | Data and Methods

The data set analysed in this thesis was obtained during a student cruise on board the research vessel *Kristine Bonnevie*. The cruise lasted eight days from February 2-10, 2017. The data was collected as part of the course, GEOF337 - Physical oceanography in fjords, led by the Geophysical Institute at the University of Bergen. The focus area stretched from Svanøy to just east of the Ålasund, with a special emphasis on the Ålasund sill and the deposit site (Figure 2.2). During the cruise, several measurements were made with a Conductivity, Temperature, Depth instrument (CTD), Micro Structure System (MSS), and vessel-mounted Acoustic Doppler Current Profiler (VMADCP). In addition, five bottom anchored moorings (F1-F5) were deployed between February 3 and March 5, consisting of current meters, and temperature, salinity and pressure loggers. The main focus of this thesis is to analyse the mooring data set. Further information about the cruise is given in the cruise report (GEOF337 Students, 2017).

### 3.1 Moorings

The moorings were located in the Ålasund area, in the centre part of the fjord (Figure 3.1). Mooring F5 was located farthest out-fjord and in the potential deposit site, at 284 m depth and extends 176 m above bottom. Mooring F1 to F4 were located across the Ålasund sill, with increasing numbers moving in-fjord. Mooring F1 was located northwest of the sill, at 210 m depth, and extends 185 m above bottom. Mooring F2 was located on the sill, west of the saddle point at 64 m depth, and extends 10 m above bottom. Mooring F3 was placed on the sill, east of the saddle point at 50 m depth, and extends 40 m above bottom. Mooring F4 was placed east of the sill, at 214 m depth, and extends 130 m above bottom. The data record lasted from 12:30, February 3 to 14:30, March 5. Mooring F1 was moved unintentionally at 12:00, February 21 by a fishing boat, therefore no data was recovered from F1 after this time. Detailed information on the moorings is provided in Table 3.1, and in Section 3.1.2. A drawing for each mooring is included in the Appendix.

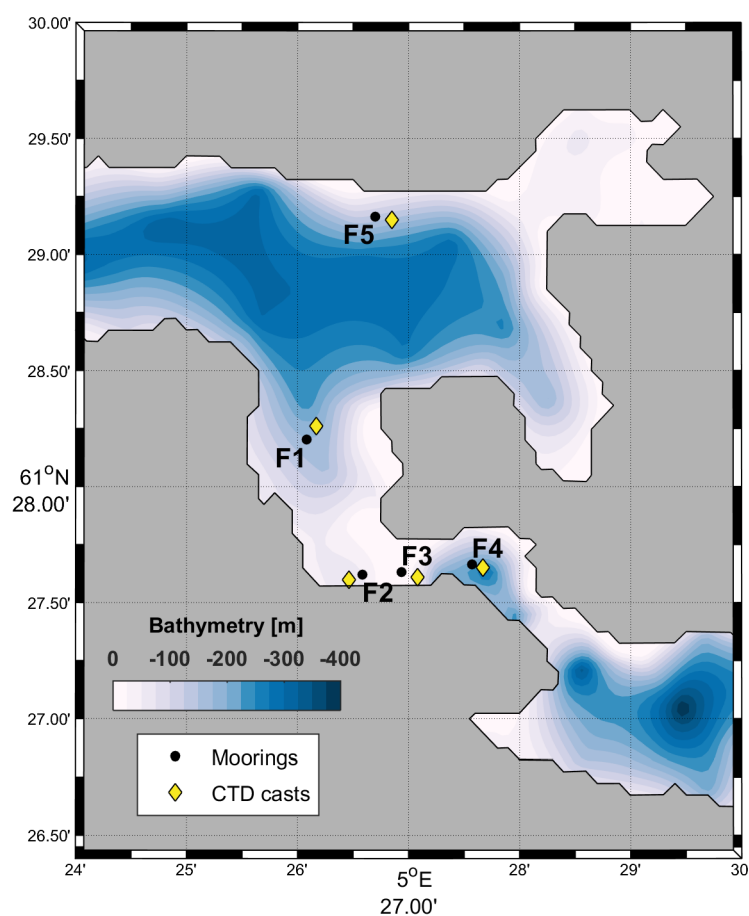


**Figure 3.1** – Deployment positions of moorings F1-F5. See Figure 2.2 for location in the Fårdefjord. F5 is located close to the deposit site, F2 and F3 on either side of the Ålasund sill and F1 and F4 in the basin on each side of the sill. The depth at the Ålasund sill is 50 m, and the basins on either side are approximately 300 m deep. The location of CTD casts close to each mooring is shown by diamond-shaped (yellow) markers.

**Table 3.1** – Mooring deployment details. Given depth is calculated from pressure measurements of the lowest instrument and known lengths to the bottom. F3 did not record any pressure measurements, and the target depth is written in the table. All times are in Coordinated Universal Time (UTC) in 2017.

Moorings	Latitude	Longitude	Depth (m)	Deployment (Date / Time)	Recovered (Date / Time)
F1	61° 28.20' N	5° 26.08' E	210	Feb 3 / 09:07	Feb 21 / 12:00
F2	61° 27.62' N	5° 26.58' E	64	Feb 3 / 10:36	March 5 / 16:30
F3	61° 27.63' N	5° 26.93' E	50	Feb 3 / 11:51	March 5 / 14:30
F4	61° 27.67' N	5° 27.57' E	214	Feb 3 / 12:58	March 5 / 17:20
F5	61° 29.16' N	5° 26.70' E	284	Feb 3 / 14:28	March 5 / 14:30



### 3.1.1 Instruments

The moorings are equipped with Acoustic Doppler Current Profilers (ADCP), Seaguards from Aanderaa Data Instruments (AADI), and instruments from Sea-Bird Electronics (SBE). There are four different types of ADCP instruments; the Nortek Signature250 (S250), AADI 600 kHz Recording Doppler Current Profiler (RDCP), Teledyne RD Instruments (RDI) 300 kHz Workhorse Sentinel and 500 kHz (RDI V50) 5-beam ADCPs. The Seaguards (SG) from AADI measure currents, and are also equipped with CTD sensors. In addition, one Seaguard was equipped with a water level sensor (SG WLR). Instruments from Sea-Bird Electronics include the SBE 37 MicroCAT C-T (P) Recorder, SBE 39 Temperature (P) Recorder and SBE 56 Temperature Logger.

The ADCP and SG instruments use the Doppler effect to record velocity (Gordon, 1996). The Doppler effect is the change in frequency of a wave due to movement relative to the wave source. The ADCP transmits a "ping" at a constant frequency and record the frequency of the waves scattered back to the instrument by suspended particles in the water column. The shift in frequency is used to calculate how fast and in what direction the particles move. The particles are assumed to move at the same speed and direction as the surrounding water, and can therefore represent currents. The return signal arrives back to the instrument over a period, with echoes close to the instrument arriving back first, and successive echoes arriving from further and further away (Gordon, 1996). The signal is split into successive bins, called range-gating, and the velocity measurement is therefore an average over a depth range.

A minimum of three beams are required to measure velocities in three dimensions. However, most ADCPs come with four beams in a Janus configuration for a more correct measurement of velocities. The four beams are arranged in opposing pairs and at an angle to the vertical. The velocity measured by each beam can be decomposed to horizontal and vertical velocity through trigonometry and then to Cartesian coordinates. The measurements from the two opposing beams are combined by assuming horizontal homogeneity, as the distance between the beams is short. The Janus configuration will decrease the errors in horizontal velocities introduced by the tilting of the ADCP (Gordon, 1996). Some ADCPs also have a fifth beam oriented on the vertical axes of the instrument. This beam can improve the spatial resolution of velocity measurements, give direct measurements of the vertical velocity, and enhance the detection of the sea surface (Wanis, 2013). The RDCP and RDI Sentinels have four beams, and the RDI V50 has five beams (four in a Janus configuration, and one directed vertically). The S250 has three beams for horizontal current measurements, and a fourth beam which is directed vertically (not utilized). The RDCP, RDI Sentinel and the RDI V50 utilize the Janus configuration. The set-up of a Janus configuration and a four-beam ADCP is shown in Figure 3.2.

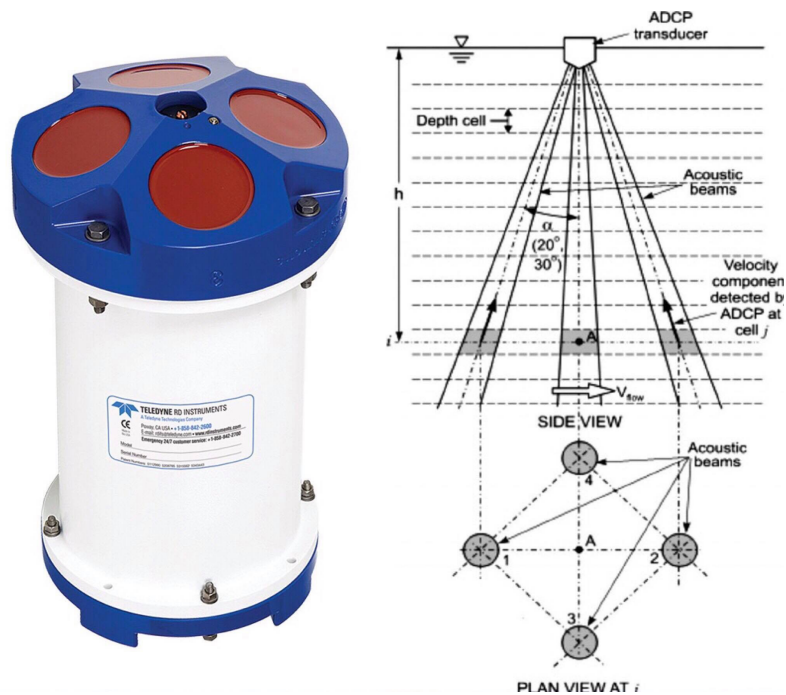


**Figure 3.2** – The ADCP from Teledyne RDI 300 kHz Workhorse Sentinel with 4 beams (image courtesy of Teledyne RDI), and the Janus configuration (from Tokyay et al. (2009)).

Most of the instruments provide pressure data. The pressure sensors are based on a silicon piezo-resistive bridge sampling. In addition to a pressure sensor, the Seaguard Water Level Recorder (SG WLR) also contains a tide and wave sensor (Aanderaa Data Instruments AS, 2008). The pressure sensor measures the hydrostatic pressure at the instrument deployment depth. In case of large variation due to surface waves, pressure from the tide sensor can be used. These pressure measurements are an average of the hydrostatic pressure measured over the integration time, 10 s to 8 min, determined by the user. Tide pressure thus smoothes the measurements and removes surface variations.

Details of the accuracy of each sensor on the different instruments are given in Table 3.2.

**Table 3.2** – Technical details of each instrument. Velocity refers to horizontal velocity, and accuracy of vertical velocities are shown if applicable.

<b>Instrument</b>	<b>Sensor</b>	<b>Accuracy</b>
S250	Velocity	1% of measured value $\pm 0.5 \text{ cm s}^{-1}$
	Direction	$\pm 2^\circ$ for tilt $\pm <30^\circ$
RDI / RDI V50	Velocity (Horizontal/Vertical)	0.5/0.3% of measured value $\pm 0.5/0.3 \text{ cm s}^{-1}$
	Direction	$\pm 2^\circ$ for tilt $\pm <15^\circ$
RDCP	Velocity (Horizontal/Vertical)	1.5% of measured value $\pm 0.5/1 \text{ cm s}^{-1}$
	Direction	$\pm 4^\circ$ for tilt $\pm <35^\circ$
SG	Velocity	1% of measured value $\pm 0.15 \text{ cm s}^{-1}$
	Direction	$\pm 2^\circ$
	Temperature	$\pm 0.03^\circ\text{C}$
	Conductivity	$\pm 0.0018 \text{ S m}^{-1}$
	Pressure (P/WLR)	$\pm 0.02/0.02\%$
SBE	Temperature	$\pm 0.002^\circ\text{C}$
	Conductivity	$\pm 0.0003 \text{ S m}^{-1}$
	Pressure	$\pm 0.1\%$

### 3.1.2 Mooring details

The instrumental set-up of moorings F1 to F5 is summarized in Table 3.3. Two SBE 56 and one SBE 39 instruments on mooring F4, and one SBE 39 on mooring F5 did not record any data (not included in Table 3.3).

**Table 3.3** – Instrument details on moorings F1 to F5. Sensors are temperature (T), pressure (P), conductivity (C) and horizontal velocity (U). The ADCPs, except S250, also measured vertical velocities.  $\Delta t$  is the sampling interval in seconds.

Mooring	Depth (m)	Instrument	Serial no.	Sensors	$\Delta t$ (s)	Comments
F1	27	SG	1925	T,P,C,U	300	-
	50	SBE56	4325	T	30	-
	70	SBE56	4326	T	30	-
	83	SBE39	6134	T,P	30	-
	103	RDI 300	10149	T,P,U	300	Upward range 84 m
	105	SBE37	5451	T,P,C	30	-
	187	SG	1930	T,P,C,U	300	-
F2	49	RDI V50	24010	T,P,U	600	Upward range 36 m
	54	SBE37	14667	T,P,C	30	-
F3	40	RDCP 600	229	T,C,U	300	Upward range 36 m
	45	SBE37	8000	T,C	30	-
F4	77	RDI V50	24015	T,P,U	600	Upward range 3 m
	113	SBE37	14666	T,P,C	30	-
	150	RDI 300	13771	T,U	300	Upward range 64 m
	150	SBE56	5195	T	30	-
	195	SG WLR	501	T,P,C,U	300	-
F5	108	RDI 300	17319	T,P,U	300	Upward range 88 m
	108	S250	100396	T,P,U	300	Downward range 100 m
	130	SBE37	8970	T,P,C	30	-
	232	SBE39	6146	T,P	30	-
	263	SG	1929	T,P,C,U	300	-

### 3.1.3 Data preparation and data quality

Frequency spectra from current measurements show that white noise dominates at frequency higher than 1 cph (cycles per hour). The data is therefore hourly averaged for comparison between instruments and moorings.

Some of the velocity depth bins from the ADCPs had to be removed for various reasons. When the echo from the transducers reach the sea surface (or bottom) for an upward (downward) pointing ADCP, the reflected signal is much stronger than what suspended particles could produce (Gordon, 1996). Velocity bins close to the boundaries are therefore removed from the ADCP data. In addition, bins with less than 70% good data are removed. Lastly, we removed bins with values that did not relate to the surrounding values. The depth ranges of the ADCP instruments given in Table 3.3 do not include the removed bins.

Temperature measurements from the Seaguard and Sea-Bird Electronics instruments, have a higher degree of accuracy than temperature measurements from the ADCP instruments (Table 3.2). These instruments are often mounted close to the ADCPs, to increase confidence in the temperature measurements (Appendix).

## 3.2 Hydrography measurements from ship

CTD profiles are obtained using a SBE 911plus CTD rosette from SeaBird Electronics. Additional sensors mounted on the rosette is a Benthos PSA-916 Series Sonar Altimeter (200 kHz), SBE 43 Dissolved Oxygen Sensor and WET Labs ECO-AFL/FL fluorometer. The Benthos altimeter measures the distance from the CTD rosette to the bottom, allowing profiling close to the bottom. The SBE 911plus CTD provide in-situ temperature,  $T$  and practical salinity,  $S$ . For further analysis, in-situ temperature is converted to Conservative Temperature,  $\Theta$ , and practical salinity to Absolute Salinity,  $S_A$ , see Section 3.4.1. The accuracy of the conductivity, temperature and pressure sensors are  $\pm 0.0003 \text{ S m}^{-1}$ ,  $\pm 0.001 \text{ }^\circ\text{C}$ ,  $\pm 0.015\%$ , respectively. The CTD rosette was operated from the vessel and recorded data on both down and upcast.

Several cross-fjord sections, 12-hour repeat stations, and one along-fjord transect were obtained (Figure 3.3). In addition, a reference station was obtained outside the Førdefjord, west of the Stavfjord (Figure 2.2). Five CTD casts were used to validate the mooring data, at moorings F4 and F5 these casts were obtained prior to deployment. Similar CTD cast were not obtained for moorings F1 to F3, instead CTD casts obtained later, close to the location of the moorings, are used (see Figure 3.1 for location relative to moorings).

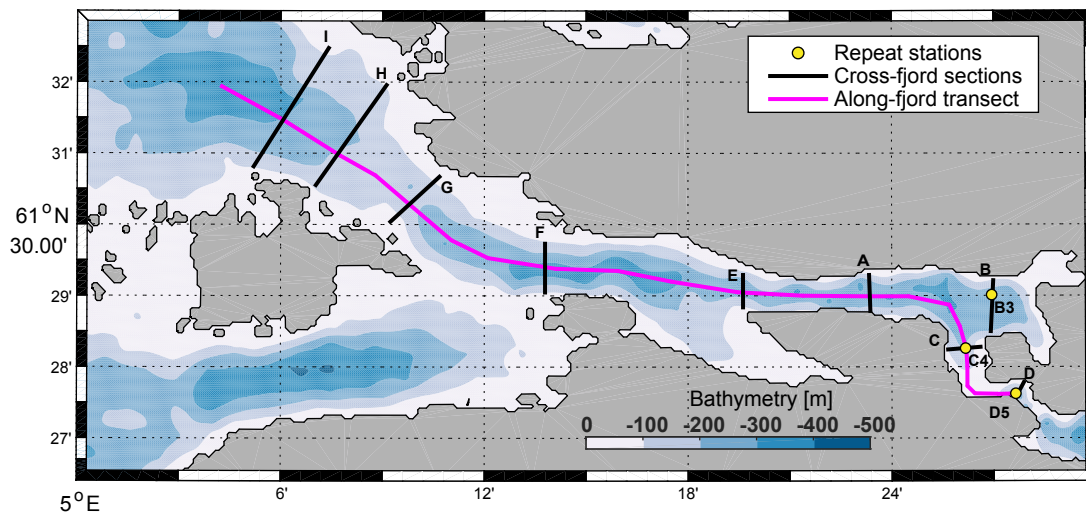


**Figure 3.3** – Overview of CTD sections, 12 –hour repeat stations and the along-fjord transect. The CTD reference station at the entrance to the Fjørdefjord is shown in Figure 2.2.

Sections I, H and G cover the outer sill, north of Svanøy, and consist of five CTD casts each. Sections A, B, E and F are located in the middle part of the fjord, between the outer sill and the Ålasund sill, and consist of seven, six, three and five CTD casts, respectively. Sections C and D are located on each side of the Ålasund sill and consist of six and eight CTD casts, respectively. Section A and parts of Section B were done twice. Each cross-fjord section was completed within 1 – 2 hours. The along-fjord transect consists of 21 casts, and was completed within 12 hours.

### 3.3 Physical forcing

The ship logged air temperature, air pressure and wind data from instruments mounted on a mast, approximately 15 m above sea level, typically every minute. Data prior to arriving (00:00, February 3) and after leaving the Fjørdefjord (00:00, February 10) are removed from the time series.

The meteorological station at the Ytterøyane Lighthouse (located 25 km north of Svanøy) is representative of the atmospheric forcing conditions in the Fjørdefjord. The weather station is operated by the Norwegian Meteorological Institute, which also has a station located at the head of the fjord in Førde (Figure 2.2). The weather stations provide time series of temperature, pressure and wind velocity. The measurements are from an altitude of 26 m above ground, and at a time interval of 6 hours.

The characteristics of the hydrography outside of the Fjørdefjord, can be obtained from CTD casts provided by IMR. IMR has obtained monthly CTD measurements at fixed sta-

tions along the Norwegian coast for over 50 years. The station closest to the Førdefjord, is Sognesjøen, located roughly 50 km south, see inset map of Figure 2.2. During our measurement period, IMR collected two CTD profiles; February 12 and March 3, 2017.

The freshwater input to the fjord is mostly from the rivers Nausta and Jølstra, both with outlets close to the head of the fjord. Their run-off is obtained from the Norwegian Water Resources and Energy Directorate (NVE). Jølstra has a specific run-off of  $273 \text{ m}^3 \text{ s}^{-1}$  and Nausta has a specific run-off of  $24.5 \text{ m}^3 \text{ s}^{-1}$  (Pettersson, 2010; Drageset, 2000).

The water level inside the Førdefjord is based on measurements from a water level gauge station located at Måløy, roughly 50 km north of the Førdefjord (see inset map of Figure 2.2). The water level at the Ålasund lags the time series from Måløy with 5 minutes. The station is operated by the Hydrographic Service of the Norwegian Mapping Authority.

The bottom matrix shown in maps is computed from the bathymetry data provided by IMR and their operational model NorKyst800 (personal communication Lars Asplin, 2017).

## 3.4 Methods

### 3.4.1 Conservative Temperature and Absolute Salinity

In situ temperature and practical salinity measurements are converted to Conservative Temperature,  $\Theta$ , and Absolute Salinity,  $S_A$ , using the Gibbs-SeaWater (GSW) Oceanographic toolbox (McDougall and Barker, 2011). Conservative Temperature and Absolute Salinity are the new standards adopted by the oceanographic community in 2010, previously potential temperature and practical salinity were used. Conservative Temperature is proportional to potential enthalpy and represents the heat content of seawater better than potential temperature. Absolute Salinity is the mass fraction of dissolved material in seawater, in units of  $\text{g kg}^{-1}$ , and is calculated from the density of the water parcel (IOC et al., 2010). Absolute Salinity is required to calculate Conservative Temperature. At depths where this is not available, an average between neighbouring salinity instruments is used, with negligible error.

### 3.4.2 Frequency spectra

Frequency spectra are computed to find the dominant time scale of variability at each mooring location. The method used in this thesis is the multi-taper method (Lilly, 2017). This method utilize Slepian tapers, where the number of tapers control the degree of smoothing of the data. Here, six Slepian tapers are applied to the data. After inspection of the frequency spectra, the data is averaged to time intervals of 1 hour.



### 3.4.3 Harmonic analysis of tides

Harmonic analysis of the tides is performed using the toolbox `t_tide` in MATLAB (Pawlowicz et al., 2002). The equilibrium tide can be written as a sum of harmonic components, each component has its own frequency, relative phase and amplitude. The tidal signal is decomposed into constituents by harmonic analysis, modelling the tidal response using Equation 3.1 for  $N$  constituents.

$$x(t) = b_0 + b_1 t + \sum_{k=1, \dots, N} a_k e^{i\sigma_k t} + a_{-k} e^{-i\sigma_k t}, \quad (3.1)$$

where each constituent has a frequency  $\sigma$  and a complex amplitude  $a_k$ . To minimize the difference between observed and computed results a least-squares fitting is applied to determine the coefficients.

$$E = \sum_m |x(t_m) - y(t_m)|^2 = \|Ta - y\|^2, \quad (3.2)$$

where  $y(t)$  is the observed time series,  $a = [b_0, b_1, a_1, a_{-1}, a_2, a_{-2}, \dots, a_{-N}]$  and  $T$  is a  $M \times 2N + 2$  matrix of linear and sinusoidal basis functions evaluated at observation times.

Tidal analysis of current velocity with `t_tide` provides ellipse parameters (the tip of the velocity vector trace out an ellipse during one tidal period). When the analysis include constituents whose ellipses are aligned in an east/west direction, the inclination parameter may fluctuate between  $0^\circ$  and  $180^\circ$ . These values do not represent true physical values, but are an artefact of restricting the definition of the inclination to the northern axis (Pawlowicz et al., 2002).

`T_tide` provide 45 astronomical and 101 shallow-water constituents for the calculations. The standard analysis includes all astronomical and 45 of the shallow-water constituents, and additional shallower-water constituents can be specified. To resolve all the tidal constituents, a time series of 18.6 years is needed to account for decadal variations. For shorter time scales, `t_tide` accounts for this by nodal corrections.

The package also include confidence intervals for the estimated tidal parameters. Error estimates help decide whether a constituent represents true tidal energy or is a result of broad-band non-tidal processes. First, an estimate of the characteristics of non-tidal noise affecting the  $a_k$  need to be calculated, which are then converted to confidence intervals through non-linear mapping. When the error is calculated, a signal-to-noise power ratio (SNR) can be computed based on the square of the ratio of tidal amplitude to amplitude error. For this thesis, a SNR above 1 is accepted for the different constituents, that is, out of the all the calculated constituents only those with  $\text{SNR} > 1$  are utilized.



### 3.4.4 Vertical modes

The vertical structure of the baroclinic tidal currents were obtained by normal mode analysis. The vertical velocity profiles are projected onto an orthogonal basis of vertical modes, with vertical structure,  $G_j$ , using (Phillips, 1977):

$$\frac{d^2 G_j(z)}{dz^2} + \left[ \frac{N^2(z)}{c_j^2} \right] G_j(z) = 0, \quad (3.3)$$

where  $c_j$  is the eigenspeed of mode  $j$ . The equation is derived from the linearised governing equations of fluid motion. In addition, a boundary condition is stated of a rigid lid at the surface and a horizontal bottom.

$$G_j(-H) = G_j(0) = 0 \quad (3.4)$$

where  $H$  is the total depth.

Together, Equation 3.3 and Equation 3.4 form an eigenvalue problem. This equation has an infinite set of solutions  $G_j$ , eigenfunctions, with corresponding eigenvalues  $c_j$ . The zero mode is the barotropic mode and higher modes are baroclinic modes;  $n = 1$  is the first baroclinic mode,  $n = 2$  second baroclinic mode etc. The  $n$ th vertical mode of horizontal velocity has  $n$  zero crossings in  $z$ .

This eigenvalue problem is solved numerically using an observed buoyancy frequency,  $N$  profile, calculated from vertical profiles of Conservative Temperature and Absolute Salinity using Equation 2.8. The temperature and salinity profiles are from CTD casts obtained close to the moorings. The eigenspeeds are approximately the phase velocity of each mode.

### 3.4.5 Other

Progressive vector diagrams (PVD) is a way to plot velocity time series (Thomson and Emery, 2014). A PVD display the trajectory of a water parcel as it would move in time at that specific location. Although the measurements are from a single point (Eulerian) it gives the impression of a measurement that follows the particle (Lagrangian). Nevertheless a PVD can be useful for long-term vector-mean currents and rotational behaviour. PVDs are also used to determine if measurements from closely mounted instruments agree.

When the presentation and analysis of data did not focus on tidal signal, time series are filtered. A low-pass filter of 25 hours from J.M. Lilly's toolbox is used to remove tidal effects from the data series (Lilly, 2017). The function calculates averages over moving windows with Hanning filters.



## 4 | Physical forcing and environmental conditions

Weather conditions, the water level, and the hydrography and stratification of the coastal area outside the fjord, recorded during the study period, control the oceanographic processes in the F rdefjord. In this chapter, the forcing conditions are described, which set the scene for the results presented in the next chapter.

### 4.1 Weather conditions

Atmospheric forcing during the mooring observation period, is inferred from data collected at the meteorological station at the Ytter yane Lighthouse. A comparison of the atmospheric data from the cruise, and the meteorological station for the same period agrees (Figure 4.1 and Figure 4.2), hence the data from the Ytter yane Lighthouse are representative of the atmospheric conditions during the mooring observation period. However, the wind speed and direction at the Ytter yane Lighthouse can be quite different from the wind inside the F rdefjord, due to topographic effects.

Air temperature, air pressure and wind velocity from the ship's mast and the Ytter yane Lighthouse, between February 2 and March 8, are shown in Figure 4.1 and Figure 4.2. During the cruise the weather was fair, with mostly blue skies and sun. Between February 4 and February 8, air temperature dropped from approximately 10 C to 0 C, and the pressure increased by 40 hPa. A period of relatively cold temperatures and high air pressure followed until February 16, when the pressure dropped to below 1000 hPa for the rest of the mooring observation period. After February 16, the air temperature fluctuated around 5 C, except for a drop to 0 C accompanied by an increase in pressure on February 24.

The prevailing wind direction was toward north, except in a period between February 19 and February 27, when the wind was stronger with a variable direction. At this time, the wind speed reached 15 m s<sup>-1</sup>, and the direction changed from north toward south on February 20, and again on February 23.

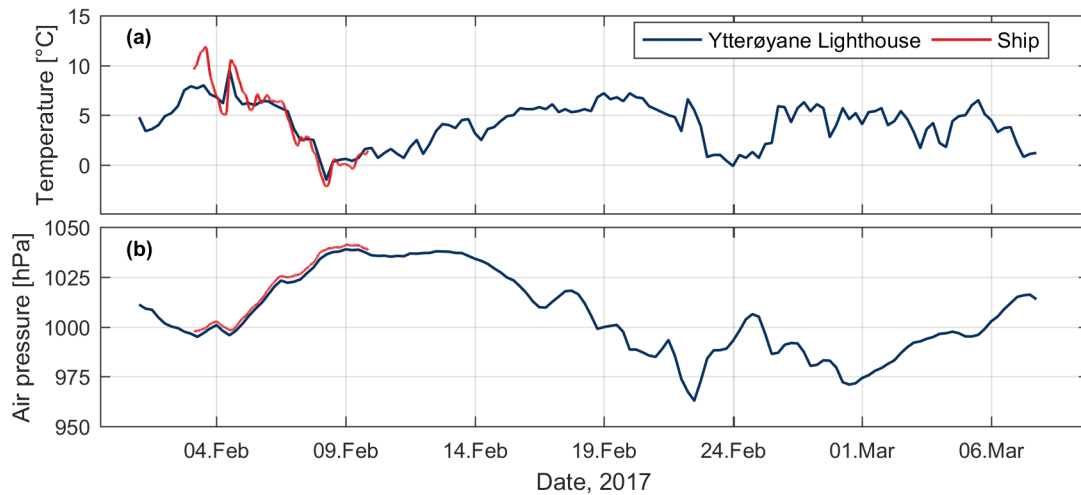


**Figure 4.1** – Time series of (a) air temperature, and (b) air pressure measured from the ship’s mast during the cruise (red) and at the Ytterøyane Lighthouse (blue) for the duration of the mooring observation period. The measurements from the Ytterøyane Lighthouse are from 26 m above sea level with a 6–hour temporal resolution. The shipboard measurements are from 15 m above sea level with a 1–min temporal resolution, and averaged to 6 hour intervals for comparison. The two datasets are not adjusted vertically to account for the height difference.

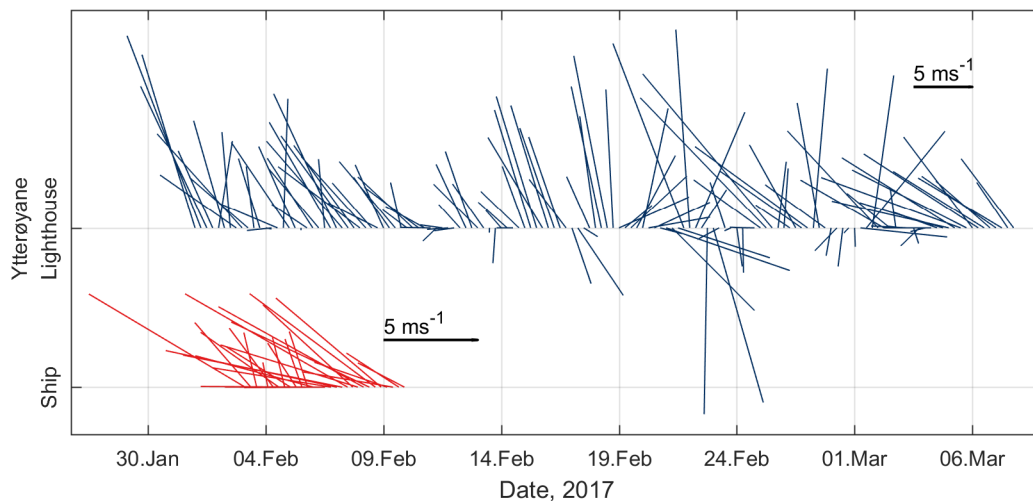


**Figure 4.2** – Time series of wind velocity vectors measured from the ship’s mast during the cruise (red) and at the Ytterøyane Lighthouse (blue) for the duration of the mooring observation period. Arrows pointing upward represent wind toward the north and arrows pointing horizontally to the left represent wind to the west.

## 4.2 Water level

The water level in the Førdefjord is dominated by the semidiurnal tide, with an amplitude range of 1.5 m during spring tides, and 0.5 m during neap tides (Figure 4.3a). The mooring period covers two spring-neap cycles, spring tides reach a peak on February 13 and March 1, and neap tides occur on February 6 and February 21.

The water level is decomposed into variability caused by deterministic tides and a residual, related to variability caused by e.g. atmospheric forcing, using harmonic analysis (Section 3.4.3, (Pawlowicz et al., 2002)). During the first spring tide, between February 6 and February 20, the water level is suppressed compared to the next spring tide (Figure 4.3b). At the same time, high atmospheric pressure is measured at the Ytterøyane Lighthouse (Figure 4.1). An increase in variability is observed in the atmospheric forcing on February 4, and again on February 22, which corresponds well to periods of strong wind observed at the Ytterøyane Lighthouse (Figure 4.2).

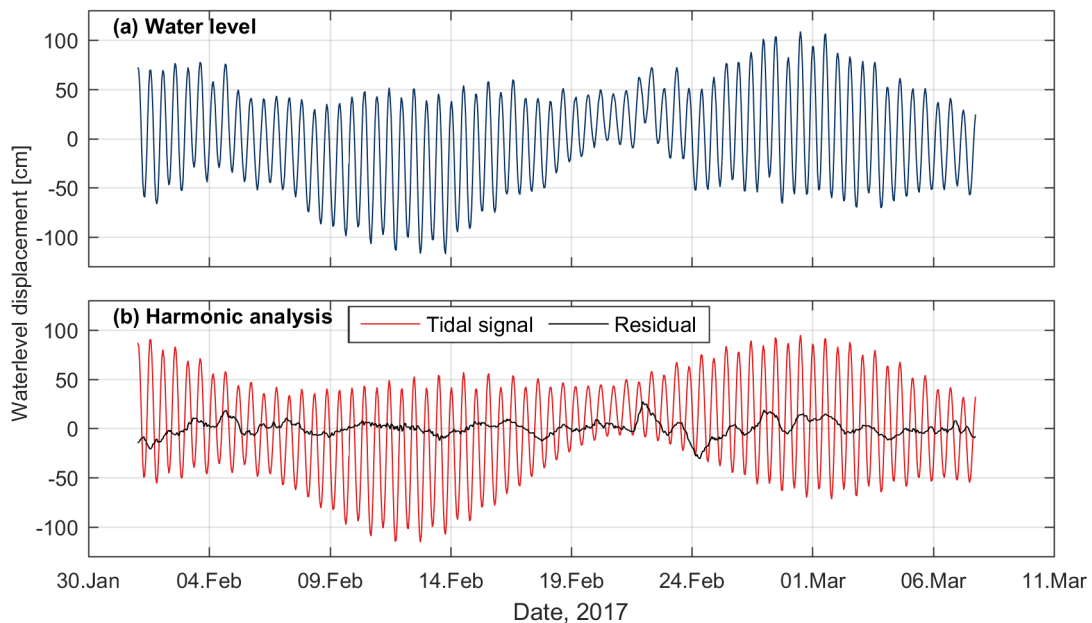


**Figure 4.3** – Time series of (a) water level calculated from sea-level gauge measurements at Måløy, and (b) the water level decomposed into tidal and atmospheric forcing.

## 4.3 Hydrography

### 4.3.1 Outside the Førdefjord

The hydrography of the coastal water during the mooring period is represented by CTD casts obtained outside the Førdefjord. Three CTD casts are considered, two casts obtained

by IMR in the Sognesjø during the mooring period, and one cast obtained outside the Stavfjord during the deployment cruise (Figure 4.4, see Figure 2.2 for geographical location).

The reference station from the cruise has a distinct surface layer, which is  $2\text{ }^{\circ}\text{C}$  colder and  $2\text{ g kg}^{-1}$  less saline than the measurements from the Sognesjø. A steep thermocline at 15 m depth, separates the thin surface layer from the layer below. Below 100 m in all three casts, the water column is relatively uniform, with a temperature and salinity of approximately  $8.5\text{ }^{\circ}\text{C}$  and  $35.3\text{ g kg}^{-1}$ , respectively. Above 100 m depth, the temperature and salinity decrease toward the surface by approximately  $2\text{ }^{\circ}\text{C}$  and  $2\text{ g kg}^{-1}$ . In the Sognesjø, the CTD profile from February 12 shows warmer temperatures at the surface, than what is observed three weeks later, on March 4. During the three weeks, the temperature dropped by almost  $1\text{ }^{\circ}\text{C}$  at 50 m depth. The water column lost substantial amounts of heat through vertical mixing in response to the strong winds recorded at the Ytterøyane Lighthouse between February 21 and March 1.

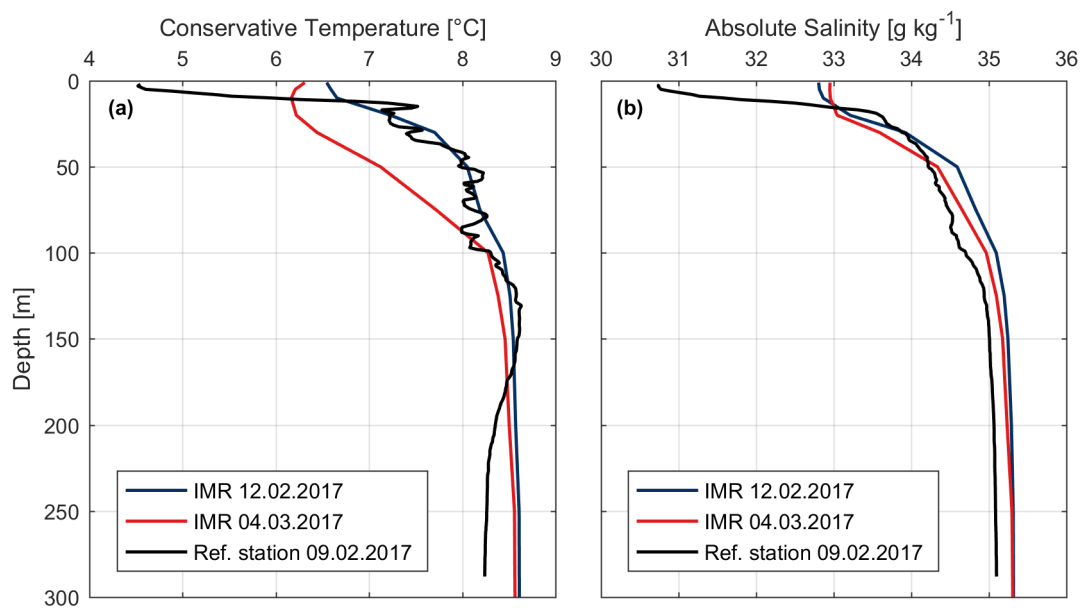


**Figure 4.4** – Depth profiles of (a) Conservative Temperature,  $\Theta$ , and (b) Absolute Salinity,  $S_A$ , from three CTD casts; two from the IMR standard station in the Sognesjø and one from outside the Førdefjord obtained during the deployment cruise.

### 4.3.2 Inside the Førdefjord

A transect of Conservative Temperature from the Ålasund toward the outer sill, obtained on February 7 between 02:00 and 11:00, is shown in Figure 4.5. The transect starts east of the Ålasund sill during slack tide, and the subsequent CTD casts were obtained during flood tide, except for the last three, which were obtained at the start of the next ebb tide

(upper panel Figure 4.5). The surface layer (upper 10 m) is approximately  $3\text{ }^{\circ}\text{C}$  colder and  $5\text{ kg m}^{-3}$  fresher (not shown) than the rest of the fjord. A cold water mass intrudes toward the Ålasund from the coast, at roughly 50 m depth. The cold tongue is approximately  $1\text{ }^{\circ}\text{C}$  colder than the surroundings, and is indicated with a white contour in Figure 4.5. The  $\sigma_{\Theta} = 26.5\text{ kg m}^{-3}$  isopycnal drops by 30 m across the Ålasund sill with distance in-fjord, at the start of flood tide.

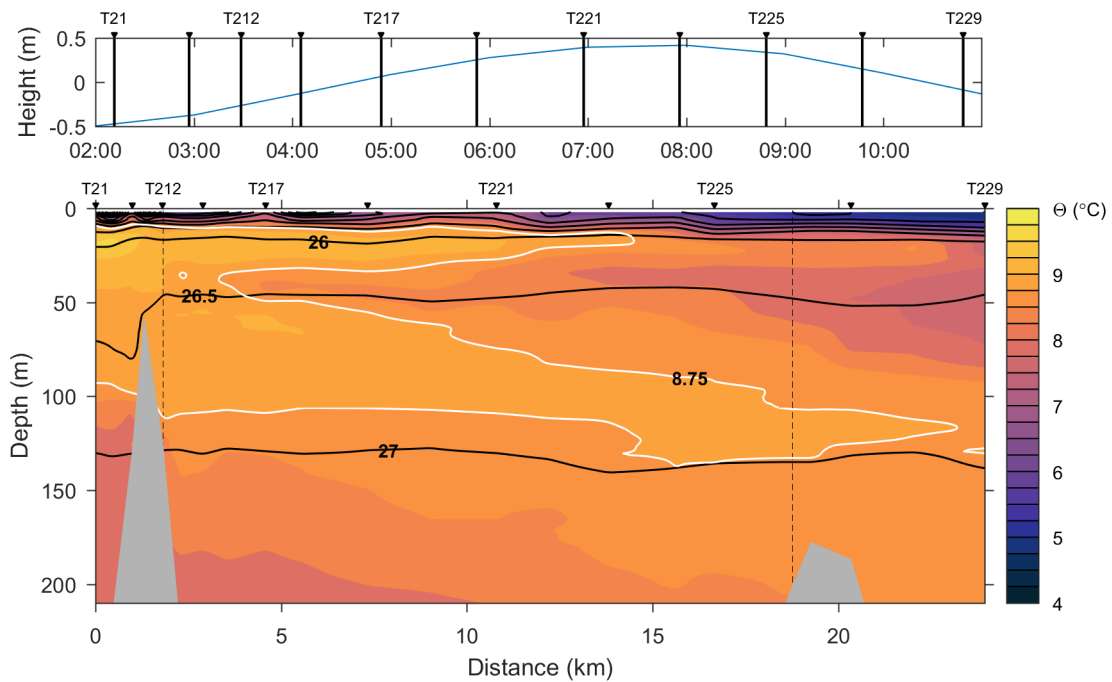


**Figure 4.5** – Along-fjord transect of Conservative Temperature,  $\Theta$ , overlain with isopycnals. Black triangles at the top show the locations of CTD casts. The Ålasund sill and the outer sill are shown in grey, and the x-axis is the distance from the start of the transect, with the Ålasund sill at  $x = 1\text{ km}$  and the outer sill at  $x = 20\text{ km}$ . The vertical dotted lines represent Section C (at  $x = 2\text{ km}$ , Figure 4.7) and Section H (at  $x = 19\text{ km}$ , Figure 4.6). There is little variation in temperature in the deep part of the fjord, therefore only the upper 220 m of the water column is shown. The upper panel shows a time series of the water level during the transect, together with the CTD casts (vertical lines).

The cold tongue observed in Figure 4.5, can also be detected in the cross-fjord sections collected at different locations in the fjord. At Section H, located west of the outer sill, the water at approximately 50 m depth is colder than the surroundings. The  $8.75\text{ }^{\circ}\text{C}$  isotherm, marked with a white contour in Figure 4.5, is observed close to the Ålasund sill at Section C (Figure 4.7). The temperature is generally colder at Section H than at Section C. In both sections the surface layer is significantly colder and fresher than the deeper parts of the fjord. Note that the dip in isopycnals toward the sides of the fjord is likely an artifact introduced by interpolation. Section H was obtained during ebb tide at 14:00, February 7 after the along-fjord transect was done. Section C was obtained at 05:00, February 4, three days

before the transect. In both sections the isopycnals are relatively flat, suggesting that there is no geostrophic circulation in this narrow fjord.

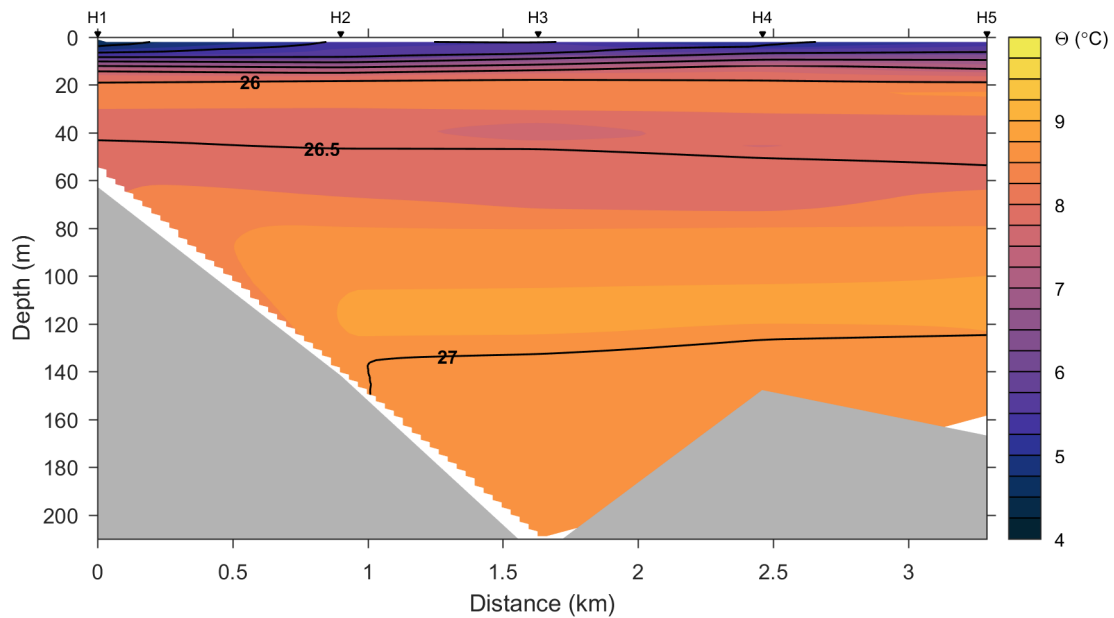


Figure 4.6 – As in Figure 4.5 but for Section H, located on the ocean side of the outer sill.

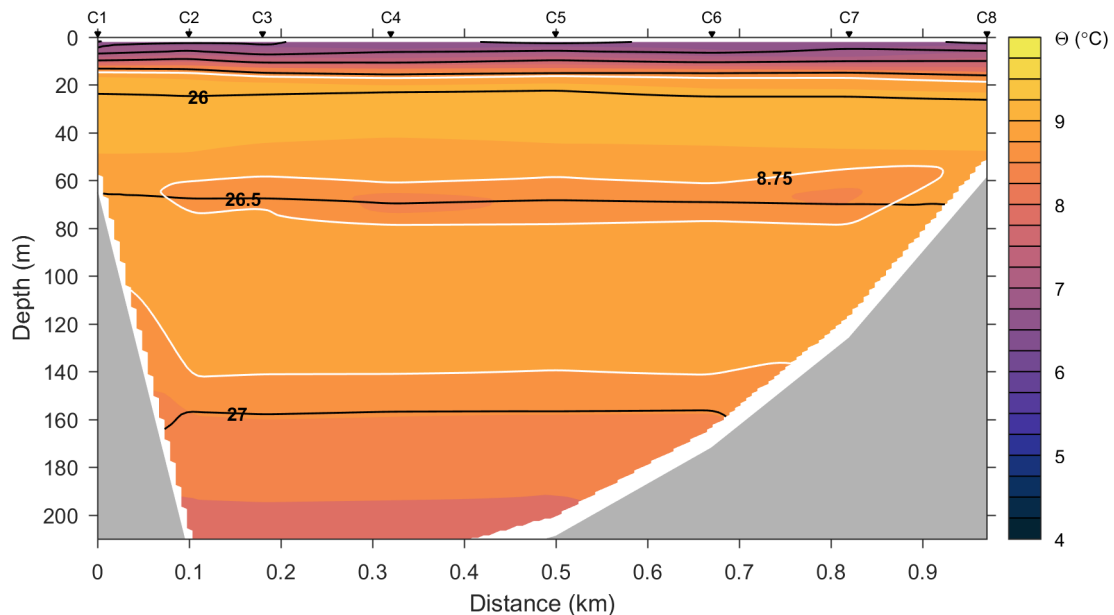


Figure 4.7 – As in Figure 4.5 but for Section C, located close to mooring F1.



## 5 | Results

In this chapter, results obtained from the mooring data are presented. The main features of the hydrography and currents in the Førdefjord, are summarized, followed by a more detailed analysis of the hydrography, currents and tidal signal.

In late winter, the Førdefjord has a fresh and cold surface layer of approximately 10 to 20 m depth, separated from the layer below by a sharp pycnocline. A homogeneous intermediate layer, observed in the temperature profiles, stretches from 20 m to 120 m depth west of the Ålasund sill, and down to 90 m depth east of the sill. On both sides of the Ålasund sill, the depth of the intermediate layer is deeper than the sill depth (approximately 50 m depth). Below the intermediate layer, the basins on either side of the Ålasund sill is filled with cold and high saline water.

The main current direction in the Førdefjord is along-fjord, and changes direction approximately every 12 hours due to semidiurnal tides. The strongest currents are found at shallow depths and in the sill region. The inner part of the fjord, east of Flokenes, is approximately 2 km wide. The Rossby radius of deformation, calculated with Equation 2.1, is approximately 6 km. Consequently, the width of the fjord is less than the deformation radius, and the fjord is classified as narrow (Cusman-Roisin et al., 1994), with minimal rotational effects in the fjord, and weak cross-fjord components.

### 5.1 Hydrography

Temperature records from the moorings highlight the temporal variability. First, vertical profiles of CTD data and mooring data are presented, for an independent validation of the mooring data. The vertical profiles agree (black and blue profiles in Figure 5.1), and the mooring data can be used with confidence for the duration of the deployment period. Moorings F2 and F3 are not shown, as there are few temperature sensors mounted on these moorings.

A 20 m thick surface layer is found at all locations, with  $\Theta = 7^\circ\text{C}$  the layer is significantly colder compared to the water below (black profiles Figure 5.1). A uniform intermediate layer of  $8.9^\circ\text{C}$  is found below the thermocline at moorings F1, F4 and F5. West of the

Ålasund sill, at moorings F1 and F5, the intermediate layer is found down to 120m depth, and interrupted by the cold tongue intrusion at 50 m depth. East of the sill, at mooring F4, the intermediate layer is found down to a depth of approximately 90 m, with no indications of a cold tongue intrusion. A steep temperature gradient at 100 m depth at mooring F4, separates the intermediate layer from the homogeneous bottom water with  $\Theta = 8^\circ\text{C}$ . West of the Ålasund sill, below the intermediate layer, the temperature drops gently until 230 m depth, below which there is a homogeneous layer with  $\Theta = 8^\circ\text{C}$  at mooring F5. The mean temperature conditions (red profile in Figure 5.1), are different at mooring F4 east of the Ålasund sill compared to moorings F1 and F5 west of the sill. The mean temperatures at moorings F1 and F5 are colder than what is observed during the cruise, while at mooring F4 the mean temperature is warmer.

The surface layer is significantly fresher, with  $S_A = 28 \text{ g kg}^{-1}$ , and lighter compared to the water below (Figure 5.2a and Figure 5.2b). Below the thermocline the water is homogeneous. The buoyancy frequency, calculated from the density profile, is high at the surface where the stratification is strong, and it quickly drops to zero at 5 m depth.

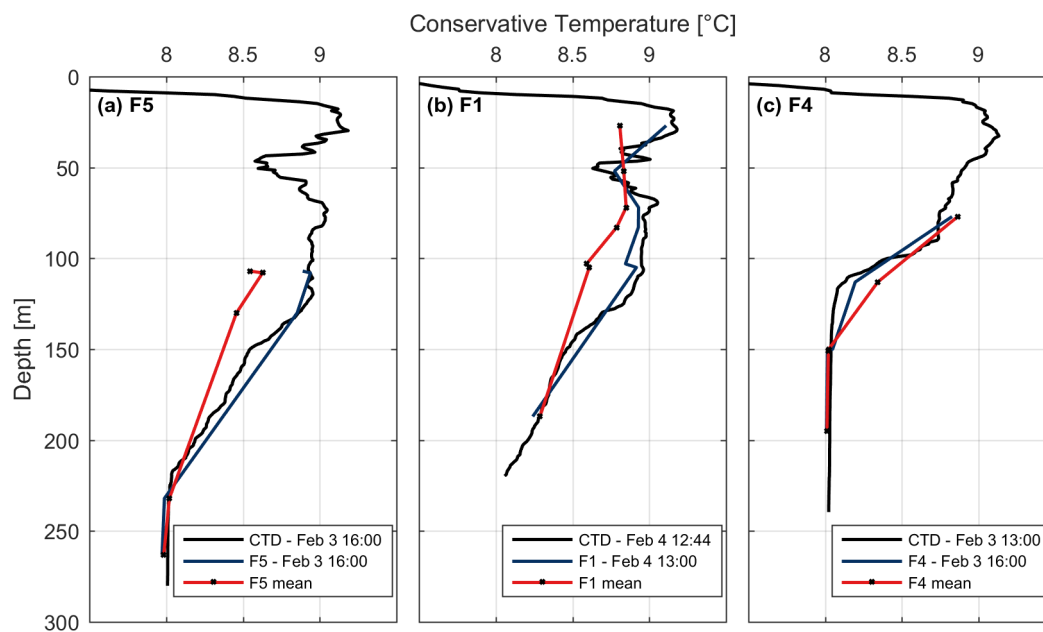


**Figure 5.1** – Conservative Temperature,  $\Theta$ , profiles at moorings (a) F5, (b) F1 and (c) F4. Data are from CTD casts (black), and from mooring measurements at approximately the same time as the CTD casts (blue) and time averaged temperature for the whole mooring observation period (red). Instrument locations are indicated by the black dots.

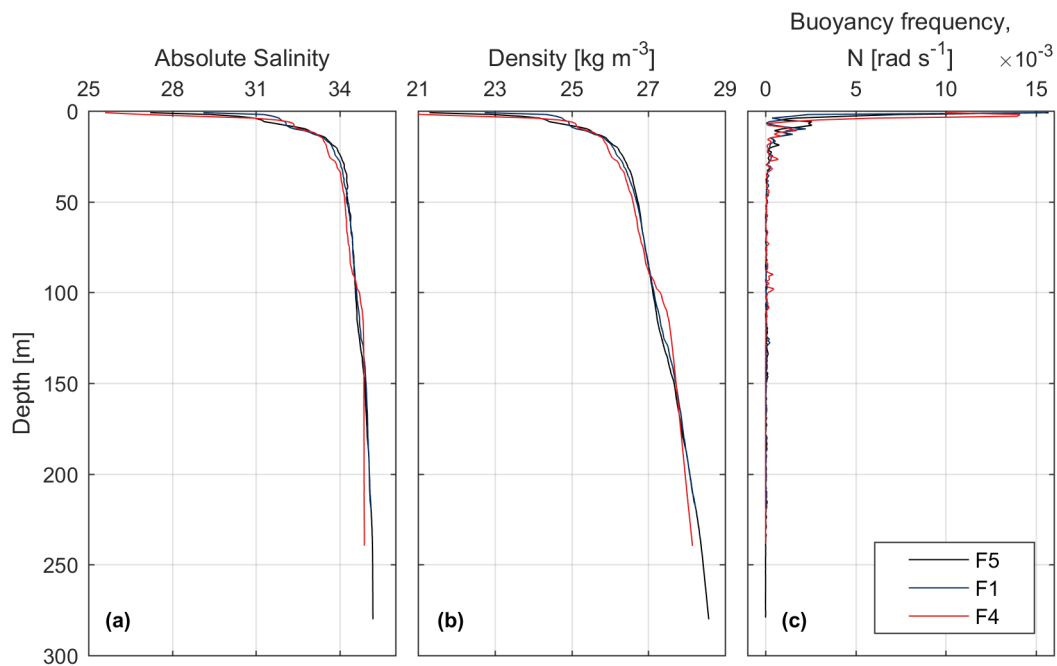


**Figure 5.2** – Vertical profiles of (a) Absolute Salinity,  $S_A$ , (b) density,  $\rho$  and (c) buoyancy frequency,  $N$  at mooring locations F1, F4 and F5. The profiles are calculated from data obtained by CTD casts close to each mooring.

Early in the record, the upper part of the water column, on the western side of the Ålasund sill, is warmer than what is observed later (Figure 5.3). Across the sill at mooring F4 the same warm period is not observed. The temperatures fluctuate with a 12 hour period, which is especially distinct at mooring F4 during spring tides, indicating that the semidiurnal tide dominates. Between February 19 and March 1, the temperature fluctuates with a lower frequency at mooring F5, and at the same time, there is an increase in temperature and variability at F2 and F3. On the Ålasund sill, the temperature is higher at mooring F2 (to the west), compared to mooring F3 (to the east). Note that the moorings do not have temperature measurements at the same depths, and the vertical axis is therefore different in the panels. The cold tongue at 50 m depth, between February 4 and February 7, can be observed at mooring F1, and it reappears on February 9, February 17 and February 20. Before these cold periods, strong southerly winds are observed at the Ytterøyane Lighthouse. The cold tongue is not observed at moorings F4 or F5, as there are no measurements at this depth.

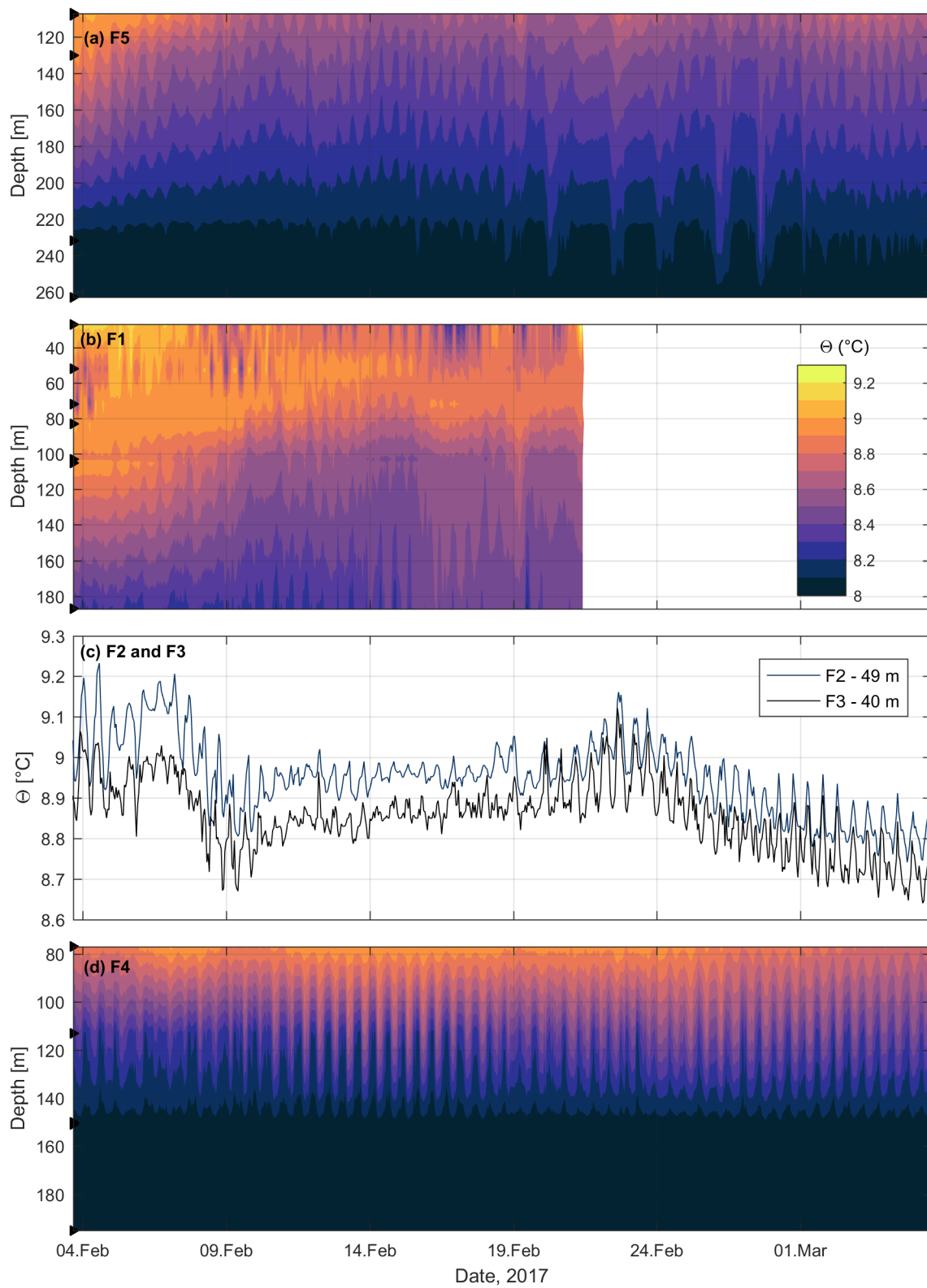


**Figure 5.3** – Time series of Conservative Temperature,  $\Theta$ , at moorings (a) F5, (b) F1, (c) F2 and F3, and (d) F4. The black triangles on the vertical axis indicate the depths of temperature recorders. Moorings F2 and F3 each has two temperature sensors, one of which is shown by a line plot. Note that the vertical depth range is not the same in each panel.

## 5.2 Currents

The strongest currents in the Fjørdefjord are observed in the along-fjord direction (Figure 5.4), and the velocities measured in the cross-fjord direction are weak (not shown). At the location of moorings F5, F2, F3 and F4, the fjord is roughly oriented east/west, and the east component is representative of the along-fjord velocity. At the location of mooring F1 the fjord is roughly oriented north/south, and the north component is representative of the along-fjord velocity.

The current velocity changes direction approximately every 12 hours west of the Ålasund sill, but the pattern is complex east of the sill, at mooring F4. The highest velocities are found at the sill, with currents of  $20 \text{ cm s}^{-1}$  directed out-fjord, but weaker in-fjord directed currents below  $10 \text{ cm s}^{-1}$ . At moorings F5, F1 and F4 the currents are weaker compared to at the Ålasund sill, and the velocity rarely exceeds  $5 \text{ cm s}^{-1}$ , except at shallow depths. The velocity above and below the sill depth at mooring F1, have oppositely directed currents. The same pattern can be seen at moorings F5 and F3 during periods of strong surface currents.

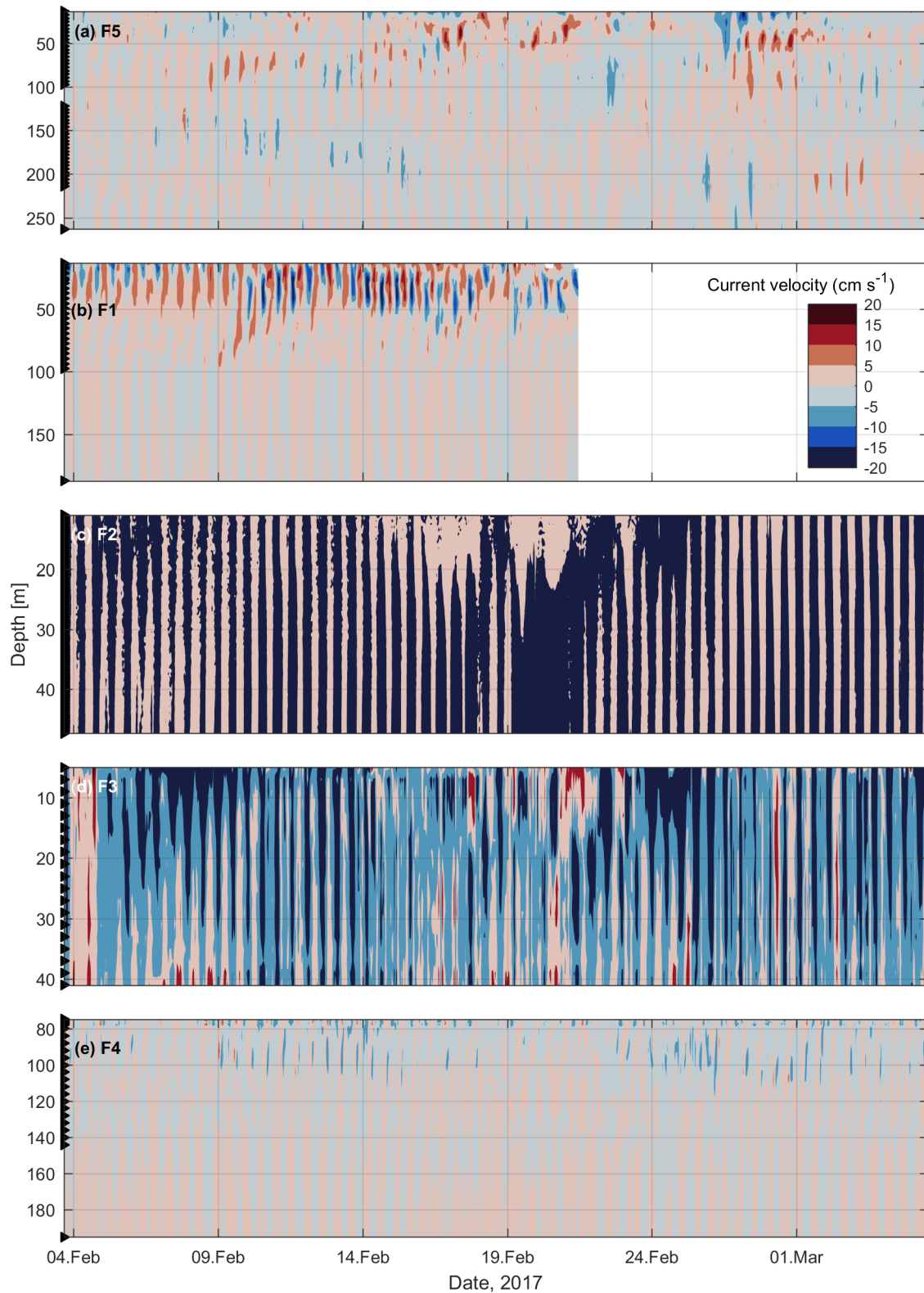


**Figure 5.4** – Time series of along-fjord velocity at moorings (a) F5, (b) F1, (c) F2, (d) F3, and (e) F4. Positive values (red) are currents directed in-fjord, while negative values (blue) are currents directed out-fjord. The black triangles on the vertical axis indicate the depths of velocity measurements. Note that the vertical depth range is not the same in each panel.

In the deepest part of the water column at mooring F5, close to the planned deposit site, the dominant current direction is along-fjord, also visible in the progressive vector diagrams (Figure 5.5). At mid-depth, here represented by 134 m depth (red), the current does not lead to a net displacement of the water parcels. The strongest currents are found at shallow depths. However, there is strong directional shear, the main current direction at 50 m depth is toward the east, while close to the surface at 18 m depth, the main direction is toward west. The upper level is representative for the surface layer of relatively fresh water, whereas at 50 m depth, the cold water intrusion is observed (Figure 4.5 and Figure 5.2a). The opposing current directions between 18 m and 50 m depth, suggest an estuarine type circulation.

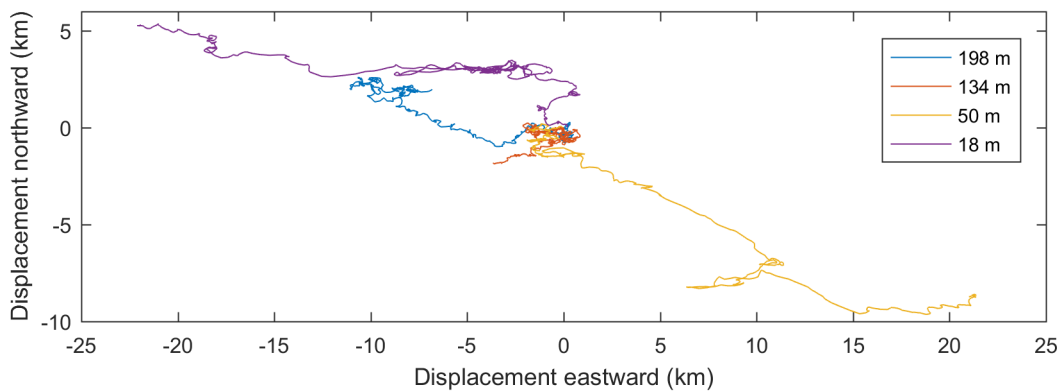


**Figure 5.5** – Progressive vector diagrams at selected depths at mooring F5. Currents toward east is directed to the left and currents toward north is directed upwards in the plot.

South of mooring F5, at mooring location F1, the direction of the surface currents varies, but at the same time northward winds are recorded at the Ytterøyane Lighthouse. In addition, on February 12, which coincides with spring tides (Figure 4.3a), the winds weaken, and the current velocity increases, as do the variability in direction. The layer below, at approximately 50 m depth, is directed in-fjord at the beginning of the observation period, indicating that the cold tongue intrusion reaches mooring F1 (Figure 5.2b). The currents in the bottom layer have a higher variability in velocity and direction than at shallower depths (Figure 5.6), but can simply be noise as the currents are close to  $1 \text{ cm s}^{-1}$ , the noise level of the ADCP.

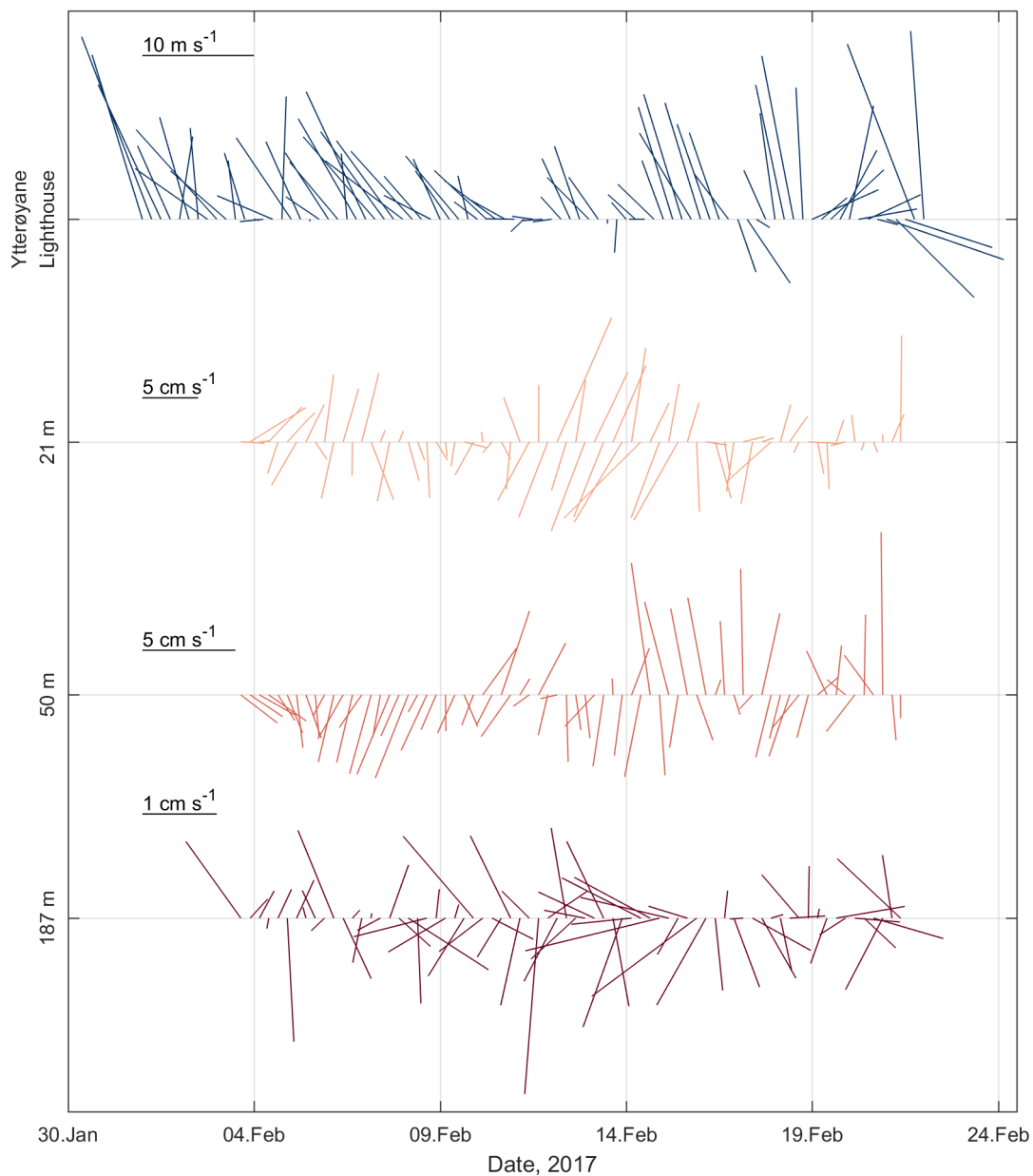


**Figure 5.6** – From top to bottom; time series of velocity vectors of wind from the Ytterøyane Lighthouse, and currents from mooring F1 at 21 m, 50 m and 187 m depth. Arrows pointing upward represent wind or currents toward the north and arrows pointing horizontally to the left represent wind or current to the west.

### 5.2.1 Frequency spectra

The distribution of energy at different frequencies is found by calculating the current velocity spectra (see Section 3.4.2 for the method used). The spectra are calculated using full time resolution (not hourly averaged), to show the noise level and difference between point measurements and the profilers. The spectra show a peak in energy at 12 hours, in-



dicating a strong semidiurnal tidal signal in the fjord (horizontal  $M_2$  line in Figure 5.7). The tidal signal is presented in detail in Section 5.4. The diurnal tide, with a period of 24 hours, is not observed in the data at any of the moorings. The highest energy is found at low frequencies, and near the surface. The energy decreases with increasing frequency. Enhanced energy is observed at 6 hours at all moorings, representing the  $M_4$  tide, a harmonic overtide of the  $M_2$  tide. The velocity spectra from mooring F4, located east the Ålåsund sill, also show peaks at higher frequencies (3 hour and 4 hour) not seen in the other moorings. In addition, a slight increase in energy can be observed in the range 1 – 3 hours (horizontal, black line in Figure 5.7c).

Note that the noise level is typically reached at 1 hour (white noise spectra), justifying the choice of 1 hour averaging period. The low frequency S250 has the highest noise level of the different instruments, as expected, whereas the point current meters (SGs) resolve lower frequencies.

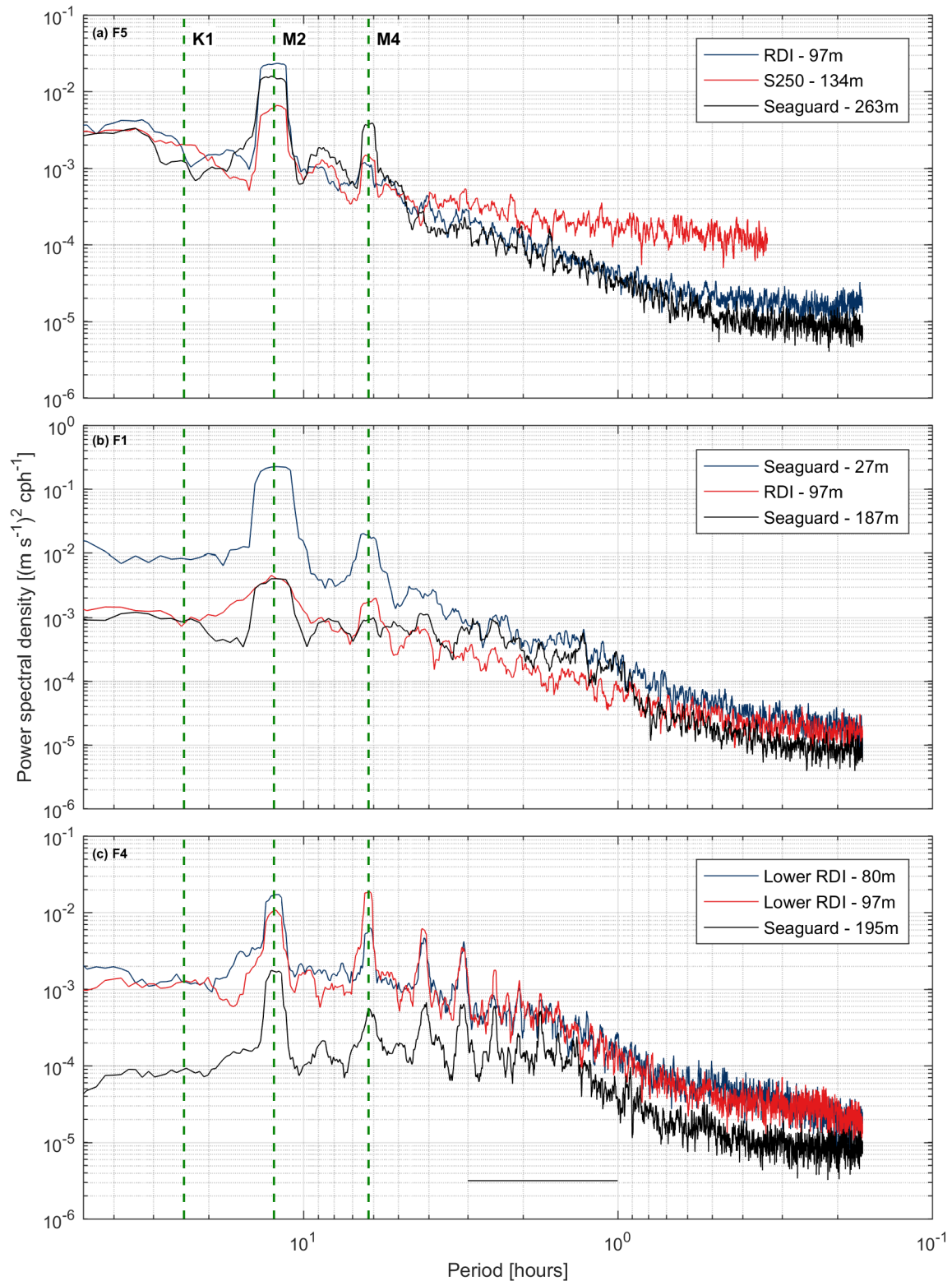


**Figure 5.7** – Velocity spectra for moorings (a) F5, (b) F1 and (c) F4. Three selected depth levels are shown for each mooring. Periods of tidal constituents  $K_1$ ,  $M_2$  and  $M_4$  are indicated by vertical dashed lines. Refer to Section 5.5.2 for an explanation of the horizontal, black line in (c).

## 5.3 Normal modes

The vertical structures of the baroclinic horizontal currents for the first three modes are shown in Figure 5.8. The difference in vertical structures between the moorings are due to differences in stratification. The modal amplitudes are highest at the surface, where the stratification is strongest. The baroclinic velocity is at its minimum at the depth of the zero-crossing for the first baroclinic mode (indicated by the horizontal dashed lines in Figure 5.8). The zero crossings occur at 134 m, 101 m and 96 m depth for moorings F5, F1 and F4, respectively. Near the zero-crossing depth, the contribution of the baroclinic currents is minimal, by definition. Current velocities at these depths are therefore used to approximate the barotropic tide at each mooring, using harmonic analysis of current records. In this thesis, the baroclinic current is approximated by removing the barotropic tide from total measured velocity. Note that this assumes a dominant contribution from mode one, as higher modes do not necessarily have a small amplitude at the chosen zero-crossing level.

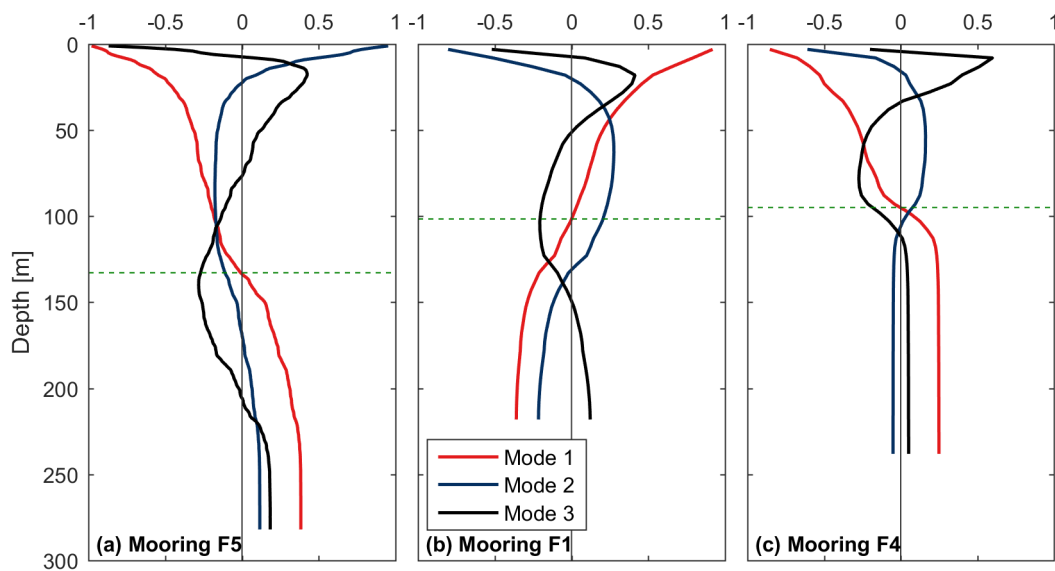


**Figure 5.8** – Vertical profiles of the first three normal modes for horizontal velocity at moorings (a) F5, (b) F1 and (c) F4. Dashed horizontal lines show the zero-crossing of the first baroclinic mode.

## 5.4 Tides

### 5.4.1 Tidal elevation

Near-bottom pressure records from moorings F5, F1, and F4 are decomposed into different tidal constituents, using harmonic analysis (Section 3.4.3, (Pawlowicz et al., 2002)). In total 16, 18 and 8 tidal constituents at moorings F5, F4 and F1, respectively, had a SNR greater than unity. Mooring F1 covers a shorter time period than the other moorings, and fewer tidal constituents can be resolved. Tidal constituents calculated at F4 and F5, and for the same time span as F1, are not significantly different from calculating the constituents using the whole period. Therefore, the whole record at F4 and F5 are used to calculate the tidal constituents in Table 5.1.

The principal lunar semidiurnal tidal constituent,  $M_2$ , with a period of 12 hours and 25 minutes, is the dominant tidal constituent in the fjord. The largest contributors to elevation changes are the semidiurnal tidal constituents ( $M_2$ ,  $S_2$ ,  $N_2$ ), which combined contribute approximately 81% and 85% of the total tidal amplitude at F5 and F1, respectively. At mooring F4 across the Ålasund sill, the contribution from the semidiurnal tidal constituents is only 46%, and a larger portion of the tidal variability is due to higher harmonics (not shown).

**Table 5.1** – Amplitude and phase of the main tidal constituents at moorings F5, F1 and F4, calculated from near-bottom pressure measurements from the Seaguard instrument mounted at 263 m, 187 m and 195 m depth, respectively.

Constituents		$O_1$	$K_1$	$M_2$	$S_2$	$N_2$
F5	Amplitude (m)	0.03	0.04	0.54	0.21	0.09
	Phase (°)	50	299	39	273	189
	Contribution (%)	3	3	52	20	9
F1	Amplitude (m)	0.04	0.04	0.55	0.20	-
	Phase (°)	276	328	315	336	-
	Contribution (%)	4	4	62	23	-
F4	Amplitude (m)	0.02	0.02	0.55	0.20	0.10
	Phase (°)	9	224	11	244	169
	Contribution (%)	1	1	30	11	5

### 5.4.2 Tidal currents

As described in Section 5.3, barotropic tidal currents are obtained from harmonic analysis of velocity records close to the zero-crossing level of the first baroclinic mode. Properties of the tidal ellipses, such as amplitudes (major and minor axes) and the inclinations (with respect to north), for the different constituents of the barotropic currents, are summarized in Table 5.2.

The amplitude of the  $M_2$  tide at mooring F5 is twice the height of the  $M_2$  tide at mooring F4 across the Ålasund sill (Table 5.2). Instead, the amplitudes of higher harmonics ( $M_4$  and  $M_6$ ) increase from F5 and F1 to F4. This is also evident when comparing the baroclinic velocity (i.e., detided current) at 80 m depth from moorings F1 and F4, with the barotropic tide (Figure 5.9). The harmonic overtides,  $M_6$  and  $M_8$ , are not observed at mooring F1, but contribute significantly to the barotropic and baroclinic amplitudes at mooring F4.

At moorings F1, F4 and F5, the mean currents are aligned with the fjord (last column in Table 5.2), as seen in Section 5.2. Note that moorings F4 and F5 do not have velocity measurements in the upper 70 m, while at mooring F1, velocity measurements also cover the surface layer. Here, we find that the currents are strongest near the surface, which could explain why the mean current at F1 is higher than at F4 and F5, where the surface currents are not resolved.

An alternative to estimate the barotropic tidal current from the zero-crossing, is to depth-average the current velocity. The barotropic tidal currents estimated from the two methods differ in magnitude. However, the differences are not consistent at each mooring. At mooring F4 the depth-averaged barotropic current is approximately 50% weaker than the barotropic current estimated from the zero-crossing, except for the  $M_2$  current, which compares well using the two methods. At moorings F5 and F1, the  $M_2$  depth-averaged barotropic current is approximately 50% weaker and 550% stronger than the  $M_2$  current estimated from the zero-crossing, respectively. The remaining constituents at the two moorings, show no differences between the two methods. However, because of the strong baroclinic currents and scattered velocity measurements at depth, depth-averaging can be biased, and the zero-crossing method is used to estimate the barotropic currents in this thesis.

**Table 5.2** – Semi- major and minor axes and inclination of barotropic tidal ellipses at moorings F5, F1 and F4.  $M_6$  at F5, and  $S_2$  at F1, have a SNR < 1 and are not significant constituents (see Section 3.4.3). The direction of the mean current at each mooring is shown in the last column. North is up, e.g. the mean current at F1 is towards the south and F4 is towards the west.

Constituents		$M_2$	$S_2$	$M_4$	$M_6$	Mean current ( $\text{cm s}^{-1}$ )
F5	Semimajor ( $\text{cm s}^{-1}$ )	1.1	0.2	0.3	-	←
	Semiminor ( $\text{cm s}^{-1}$ )	0	-0.1	0.1	-	
	Inclination ( $^\circ$ )	7	133	166	-	
F1	Semimajor ( $\text{cm s}^{-1}$ )	0.6	-	0.5	0.2	↓
	Semiminor ( $\text{cm s}^{-1}$ )	0	-	0.3	0.1	
	Inclination ( $^\circ$ )	65	-	118	5	
F4	Semimajor ( $\text{cm s}^{-1}$ )	0.5	0.5	1.1	0.6	←
	Semiminor ( $\text{cm s}^{-1}$ )	0.1	0.1	0.1	0.1	
	Inclination ( $^\circ$ )	161	5	4	5	

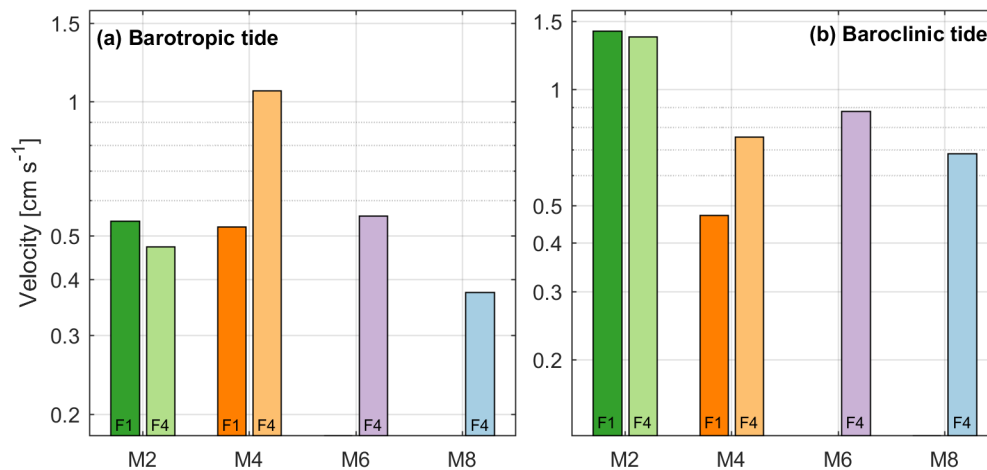


**Figure 5.9** – Bar plot of (a) barotropic tidal velocity inferred from velocity measurements at the zero-crossing of the first baroclinic mode, and (b) baroclinic tidal velocity at 80 m depth for moorings F1 (dark colors) and F4 (light colors). At mooring F1, the amplitudes of the  $M_6$  and  $M_8$  tidal constituents are small and therefore not shown. Note that the vertical axis is logarithmic, and not the same for the two panels.

The tidal ellipses for four of the main tidal constituents,  $M_2$ ,  $S_2$ ,  $M_4$  and  $M_6$ , are shown in Figure 5.10 and Figure 5.11, for moorings F5 and F4, respectively. The ellipse parameters are calculated from the total measured velocity (barotropic tide is not removed). At both mooring locations, the tidal ellipses are nearly rectilinear, and the major axes are oriented in the east/west direction. The main current is therefore directed along-fjord, with weak variability in the cross-fjord direction, indicating that rotation is not important (see beginning of Chapter 5). The tidal ellipses at mooring F5, show little variation with depth for all four tidal constituents, which indicates dominance of the barotropic tidal signal (Figure 5.10). The strongest currents are associated with the  $M_2$  tide, which is strongest at approximately 95 m depth. Across the Ålasund sill, at mooring F4, the strongest currents are observed in the upper part of the water column (at 80 m depth), and the currents are weaker in the deeper layers, which indicates a baroclinic tidal signal (Figure 5.11). In addition, the  $M_4$  and  $M_6$  constituents increase in strength across the sill, compared to the tidal ellipses at mooring F5 (Figure 5.10), and the ellipse parameters for F1 (Figure 5.9).

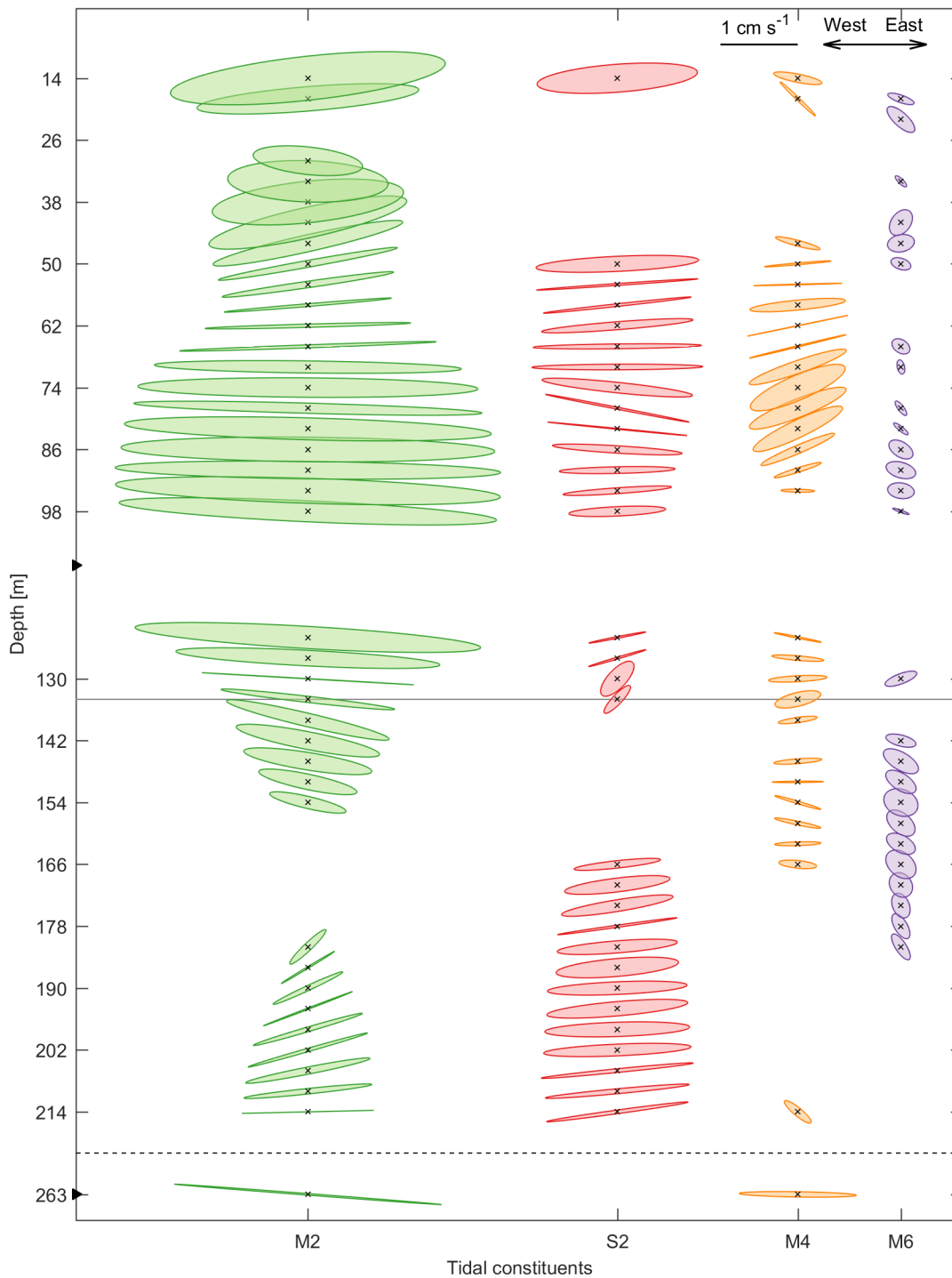


**Figure 5.10** – Tidal ellipses for the four main tidal constituents,  $M_2$ ,  $S_2$ ,  $M_4$  and  $M_6$ , at mooring F5. The horizontal grey line represent the depth of the zero-crossing for the first horizontal baroclinic mode. The black triangles on the vertical axis indicate the depths of velocity instruments, the upper one represents two ADCPs on a flotation buoy (one upward pointing and one downward pointing). Note that the scale on the vertical axis is discontinuous from the last measurement at 214 m depth to the Seaguard at 263 m depth, indicated by the dashed line. Levels that do not have a significance level above 95% for the major axis, are not plotted.



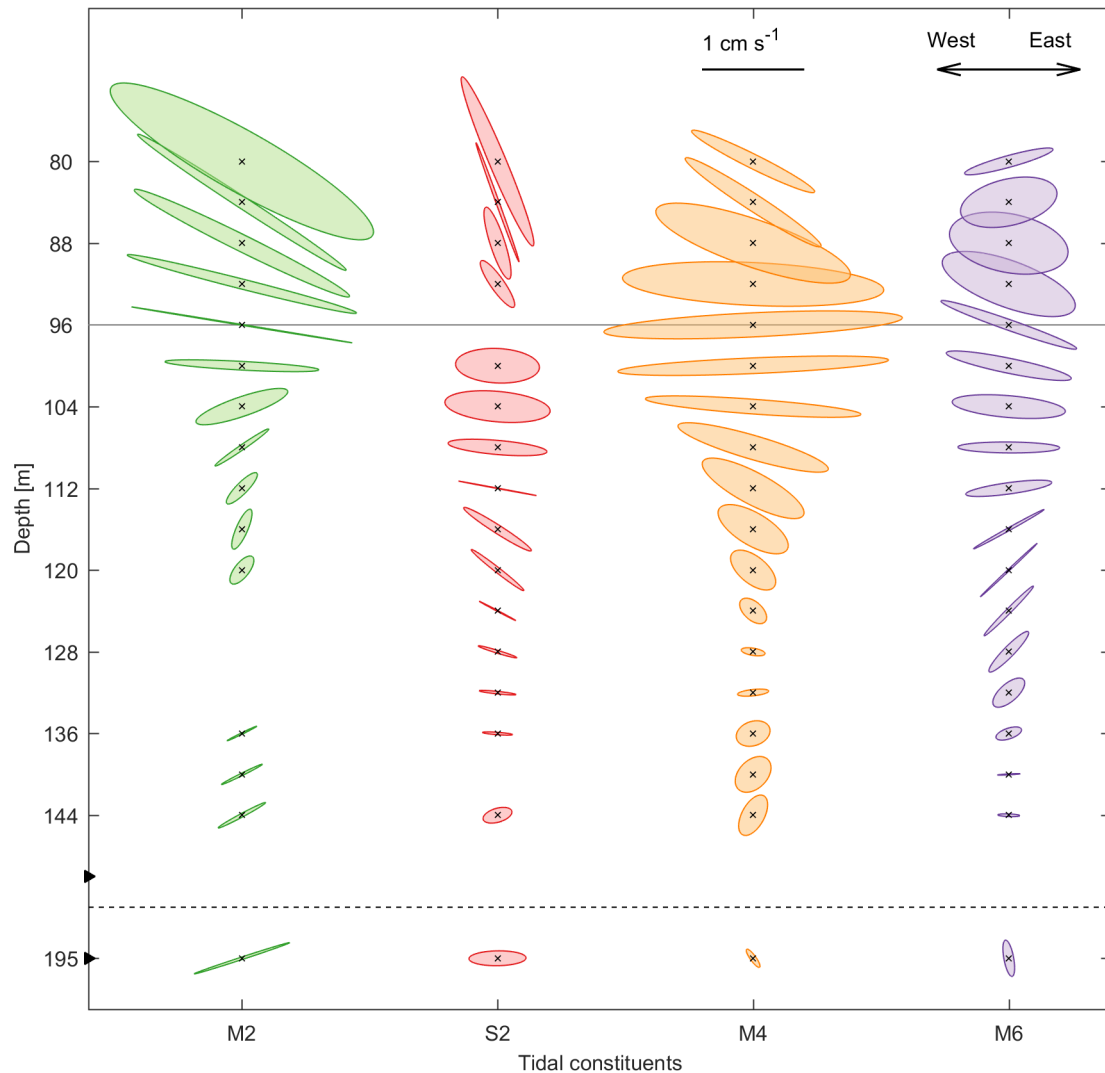


**Figure 5.11** – As in Figure 5.10, but for mooring F4. Velocity data are from two instruments, one ADCP and one Seaguard.

### 5.4.3 Residual currents

Time series of the tidal signal estimated from total velocity and the residual current for three depth levels at mooring F5 (97 m, 134 m and 263 m depth) and F4 (80 m, 96 m and 195 m depth) are shown in Figure 5.12 and Figure 5.13. The central panel, in both figures, show the tidal signal from the depth of the zero-crossing for the first baroclinic mode, and can be interpreted as the barotropic tide. The strongest tidal signal is observed at approximately 100 m depth at both moorings. The residual current appears to be larger at mooring F4 than at mooring F5, and has a strong variability throughout the record.

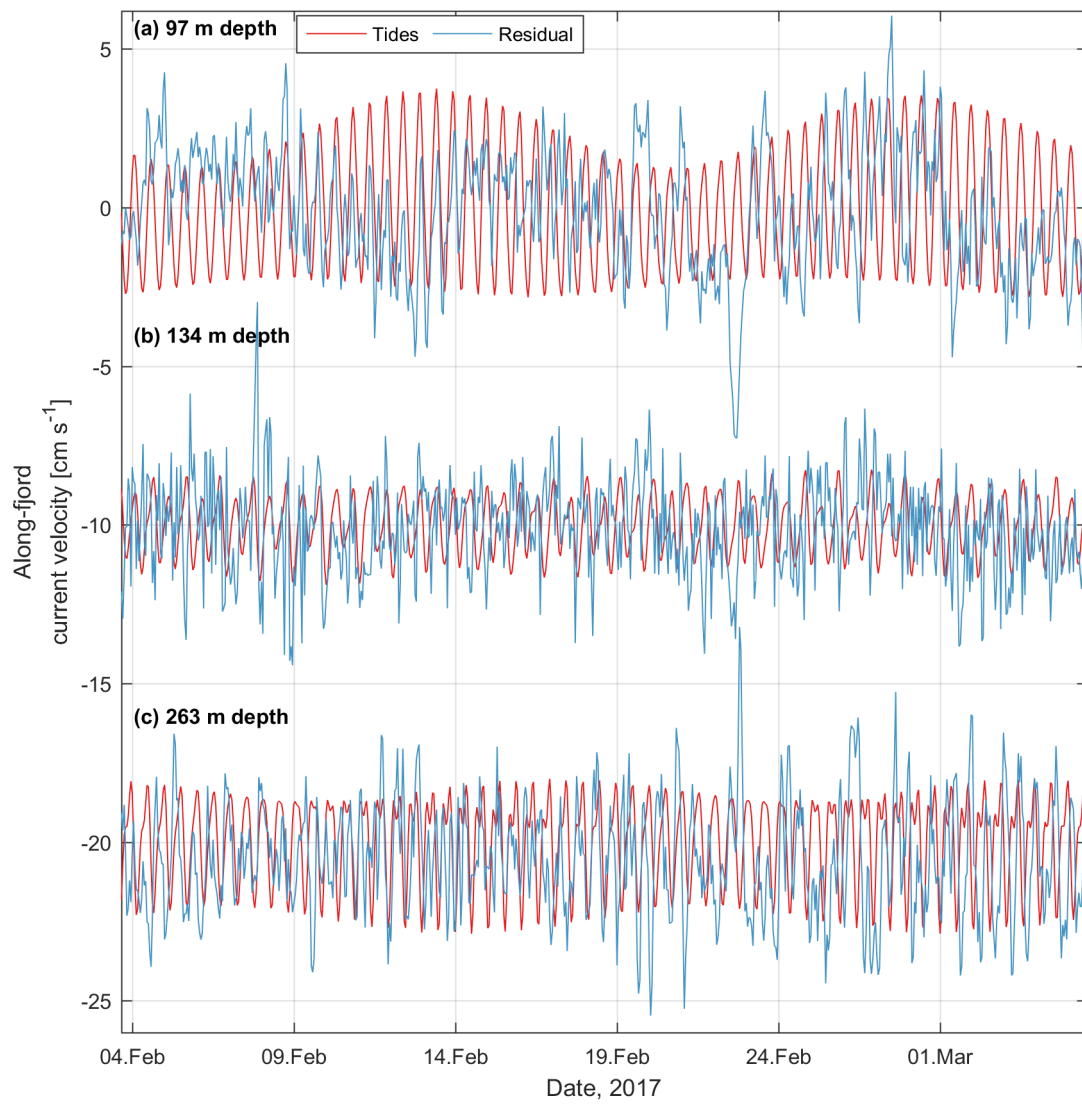


**Figure 5.12** – Time series of tidal (red) and residual (blue) currents at mooring F5, (a) 97 m depth, (b) 134 m depth (offset of  $-10$ ) and (c) 263 m depth (offset of  $-20$ ). The tidal currents are calculated from total velocity and only the dominant component is shown.

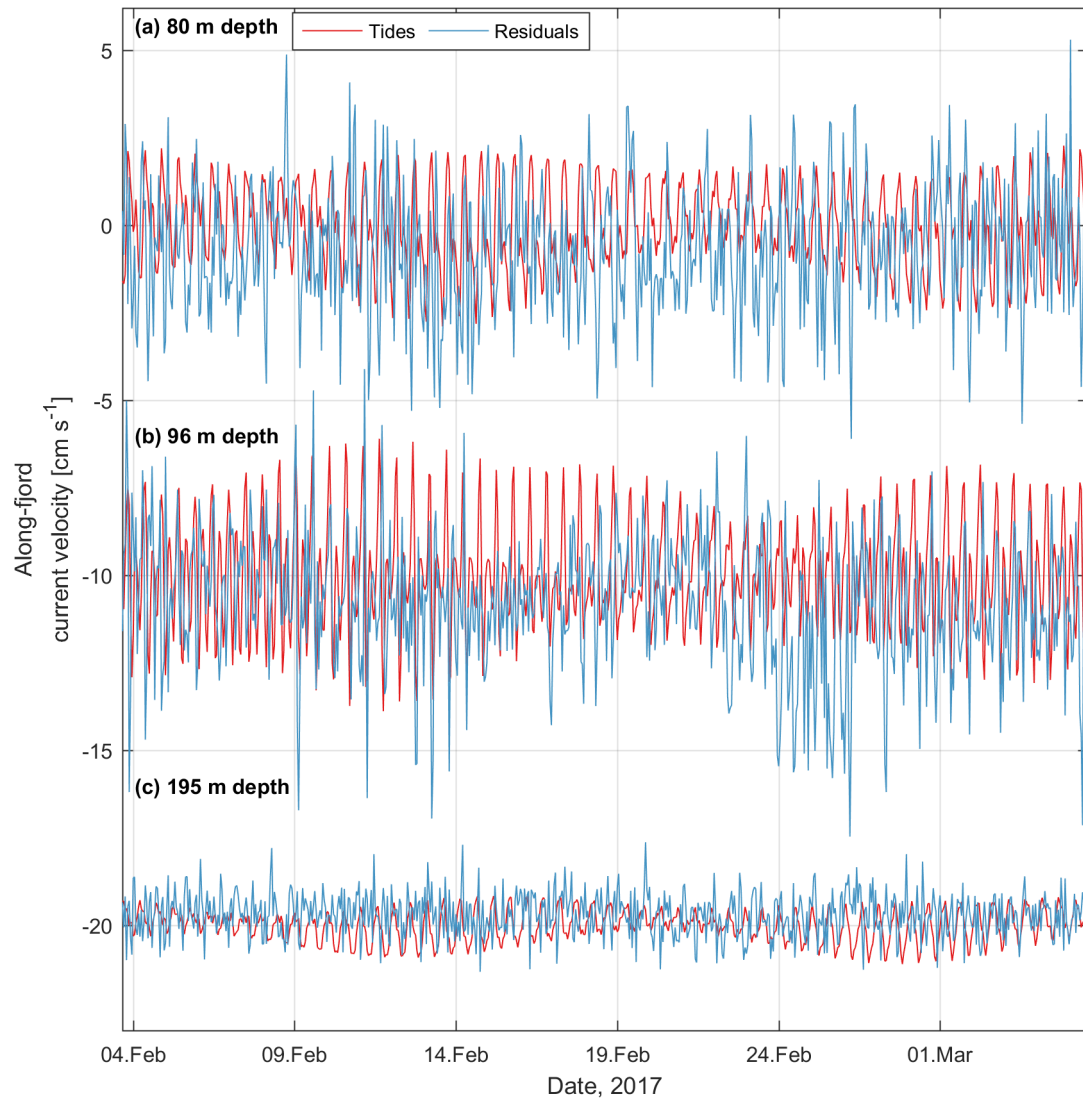


**Figure 5.13** – As in Figure 5.12, but for mooring F4, (a) 80 m depth, (b) 96 m depth and (c) 195 m depth.

## 5.5 Sill processes

### 5.5.1 Froude number

The moorings located close to the Ålasund sill, F2 and F3, have Froude numbers below unity, for the duration of the mooring period (Figure 5.14). The Froude numbers at moorings F1 and F4, rarely exceeds 0.1 (not shown). The Froude numbers are estimated from current speed and phase speed of the first baroclinic mode using Equation 2.7. The phase speed is obtained from the normal mode analysis, by numerically solving the Sturm-Louville eigenvalue problem, using the observed buoyancy frequency profile (see Section 3.4.4). The phase speed of the first internal mode at mooring F1 is  $c_1 = 0.56 \text{ ms}^{-1}$ , and it is used in the Froude number calculations for both moorings F1 and F2. The phase speed of the first internal mode at mooring F4 is  $c_1 = 0.62 \text{ ms}^{-1}$ , and it is used in the Froude number calculations for both moorings F3 and F4. The measured current velocity, rarely exceeds  $0.5 \text{ ms}^{-1}$  at any mooring or measurement depth. The highest Froude numbers are at the sill moorings, F2 and F3, where the strongest currents are found. A Froude number below unity, indicates that the Førdefjord is a wave fjord during our measurement period in late winter (Section 2.1.2).

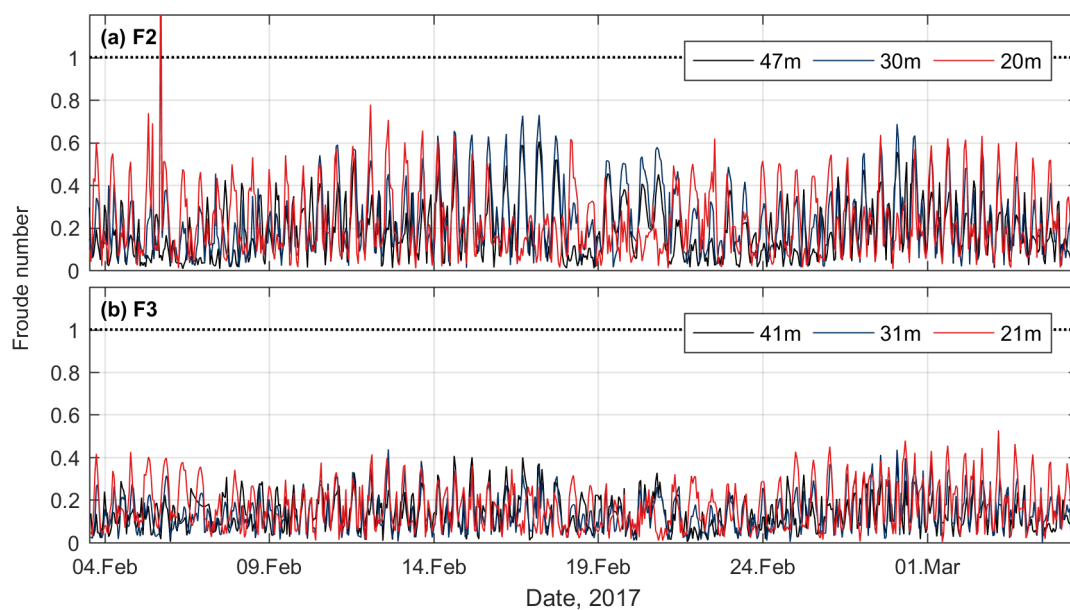


**Figure 5.14** – Time series of Froude numbers at moorings (a) F2, and (b) F3, shown for three different depths.

### 5.5.2 Baroclinic currents

On the eastern side of the Ålasund sill (represented by mooring F4), the velocity spectra show energy peaks at high frequencies,  $M_4$  and  $M_6$ , which are not observed on the western side of the sill (represented by mooring F1) (Figure 5.7 in Section 5.2.1). Figure 5.7 shows an enhancement of energy in the period between 1 and 3 hours. The baroclinic velocities at this frequency is extracted by band-pass filtering. Tidal ellipses from moorings F4 and F5 show the same transfer of energy toward higher frequencies from F5 (Figure 5.10), on the western side of the sill, to F4 (Figure 5.11), on the eastern side. The baroclinic velocities in the along-fjord direction on either side of the sill, are investigated further.

The highest baroclinic velocities at mooring F4 are observed at 80 m depth (the shallowest depth of current measurements), which is also observed in the tidal ellipses in Figure 5.11. The strength and variability of the baroclinic velocities, at all depths, increase during spring tides (Figure 5.15b). The velocity peaks are especially pronounced toward the end of spring tides, which coincides with an increase in variance of the band-passed data (Figure 5.15c). The highest variance is observed at 80 m depth, which is also the depth of the strongest observed tidal currents (Figure 5.11). The presence of higher frequencies on the eastern side of the sill, imply an energy cascade from the driving  $M_2$  tide, and will likely contribute to turbulence.

The bottom panels (Figure 5.15d-g), show details of two periods at the end of the first and second spring tides. The barotropic and baroclinic currents are oppositely directed at 80 m depth. There is a strong baroclinic current directed out-fjord before low tide, by the end of ebb tide. As the tide turns, there are strong baroclinic currents in-fjord, at the beginning of flood tide. Between the two velocity maxima, during high tide, the baroclinic currents are weak. The band-passed baroclinic velocity shows the same pattern, but the strength of the current is weaker. The barotropic current is oppositely directed, there is a strong in-fjord current before low tide, and a strong out-fjord current after low tide, whereas the baroclinic velocity is weak in between the two strong current periods.

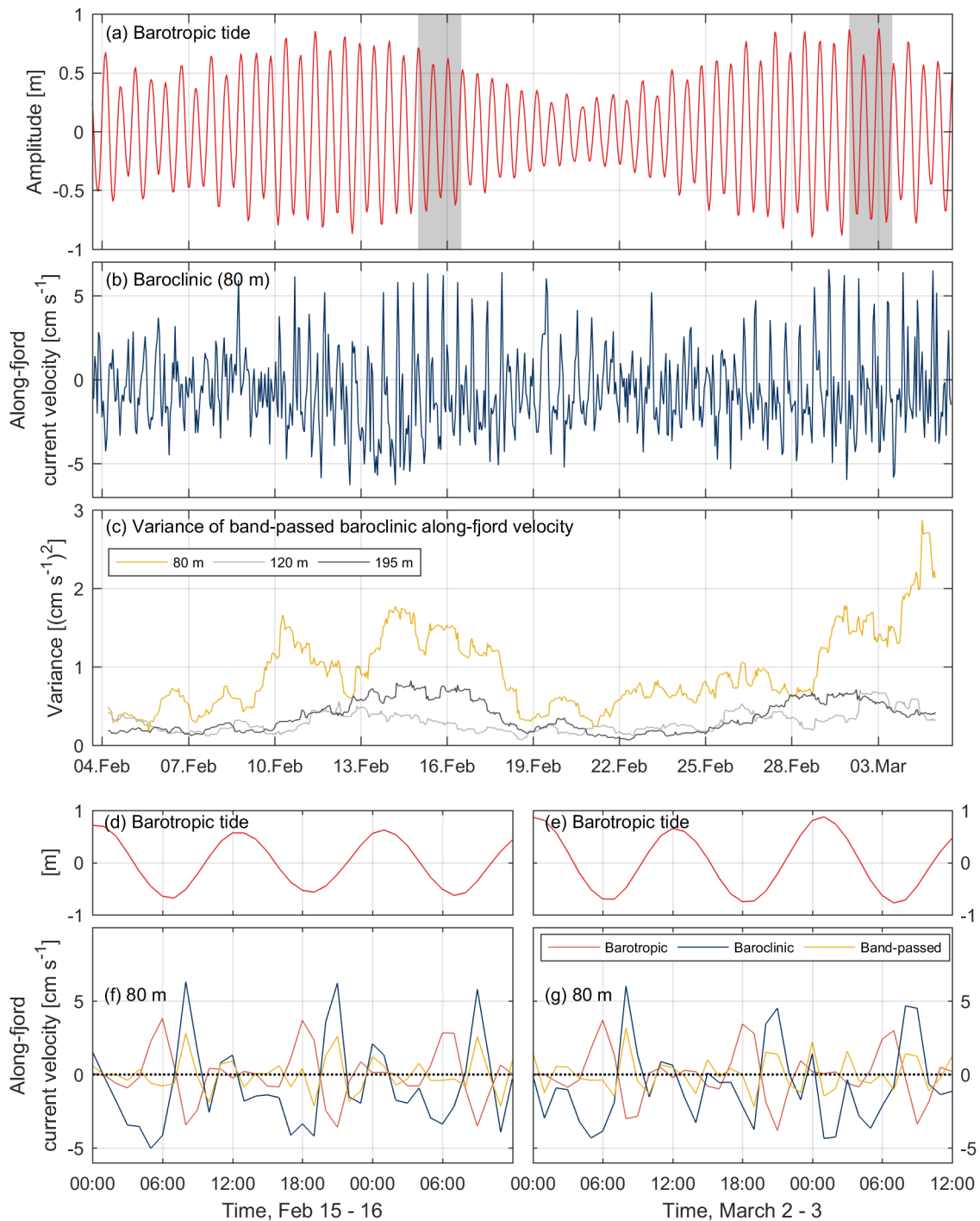


**Figure 5.15** – Time series at mooring F4 of (a) barotropic tide from pressure measurements, (b) along-fjord baroclinic velocity at 80 m depth, (c) variance of 1 –3 hour band-passed along-fjord baroclinic velocity at three depths. Time series from February 15 to February 16 (indicated by the first grey box in (a)) of, (d) barotropic tide from pressure measurements and (f) barotropic, baroclinic and band-passed along-fjord baroclinic velocity. Time series from March 2 to March 3 (indicated by the second grey box in (a)) of, (e) barotropic tide from pressure measurements and (g) barotropic, baroclinic and band-passed along-fjord baroclinic velocity. The along-fjord current is represented by the east component at mooring F4.

Figure 5.15d-g only show two isolated events, and by creating a composite of the baroclinic velocity on moorings F1 and F4, we increase the confidence in the pattern of the signal. The composites are based on ten flood events, centred at high tide, toward the end of spring tide, and support the interpretation of tidally driven high-frequency variance generation (Figure 5.16).

The baroclinic velocity at 80 m depth on mooring F4, shows the same pattern as in the isolated events, as discussed above. There is no clear sinusoidal wave-like signal at mooring F4, instead peaks of inflow are followed by longer periods of weak outflow. The peaks of inflow occur approximately 2 hours after the tide turns from low tide. Each peak inflow is accompanied by an increase in high-frequency variance.

At mooring F1, the baroclinic velocities at 40 and 80 m depth are oppositely directed, e.g. when in-fjord baroclinic currents are recorded at 40 m depth, out-fjord baroclinic currents are recorded at 80 m depth. At 80 m depth, the baroclinic currents are approximately 180° out of phase with the vertical displacement of the barotropic tide. The baroclinic currents at F1 are directed in-fjord for most of the tidal cycle, with the strongest currents occurring at low tide, while the out-fjord baroclinic current reaches a peak one hour before high tide. The baroclinic velocity at 40 m depth is directed in-fjord during flood tide, and out-fjord during ebb tide. At mooring F1, the band-passed velocity is weak, which indicates that the high frequencies are generated at the Ålasund sill by the barotropic tides.

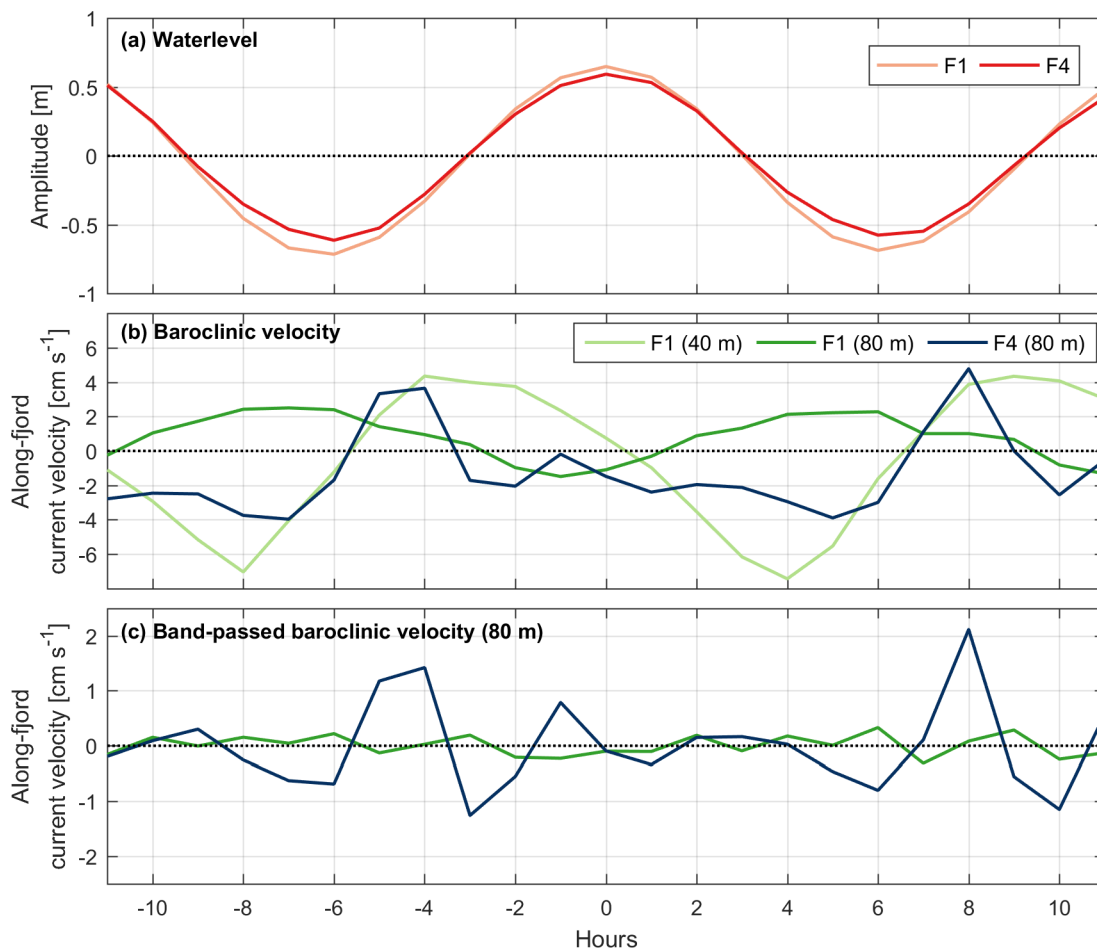


**Figure 5.16** – Time series of a typical flood cycle during spring tides, inferred from ensemble averaging of 10 events at moorings F1 and F4 of (a) barotropic tide from pressure measurements, (b) along-fjord baroclinic velocity, (c) 1–3 hours band-passed baroclinic velocity. The along-fjord current is represented by the north component at mooring F1 and the east component at mooring F4. The directions at mooring F1 is reversed, which means that positive and negative values for both moorings indicate in-fjord and out-fjord directed current, respectively. Note that the vertical axes of panel (b) and panel (c) are different.

## 5.6 Wind-driven circulation

### 5.6.1 Sill region

The local wind exerts a stress at the surface of the fjord, and depending on the wind strength and duration, the wind stress may initiate a surface current in the same direction. During the cruise, wind data recorded between February 6 and February 10, show strong westward wind in the Førdefjord. The wind is in the same direction as the ebb tide at the surface, and strong currents are observed at the Ålasund sill during ebb tide.



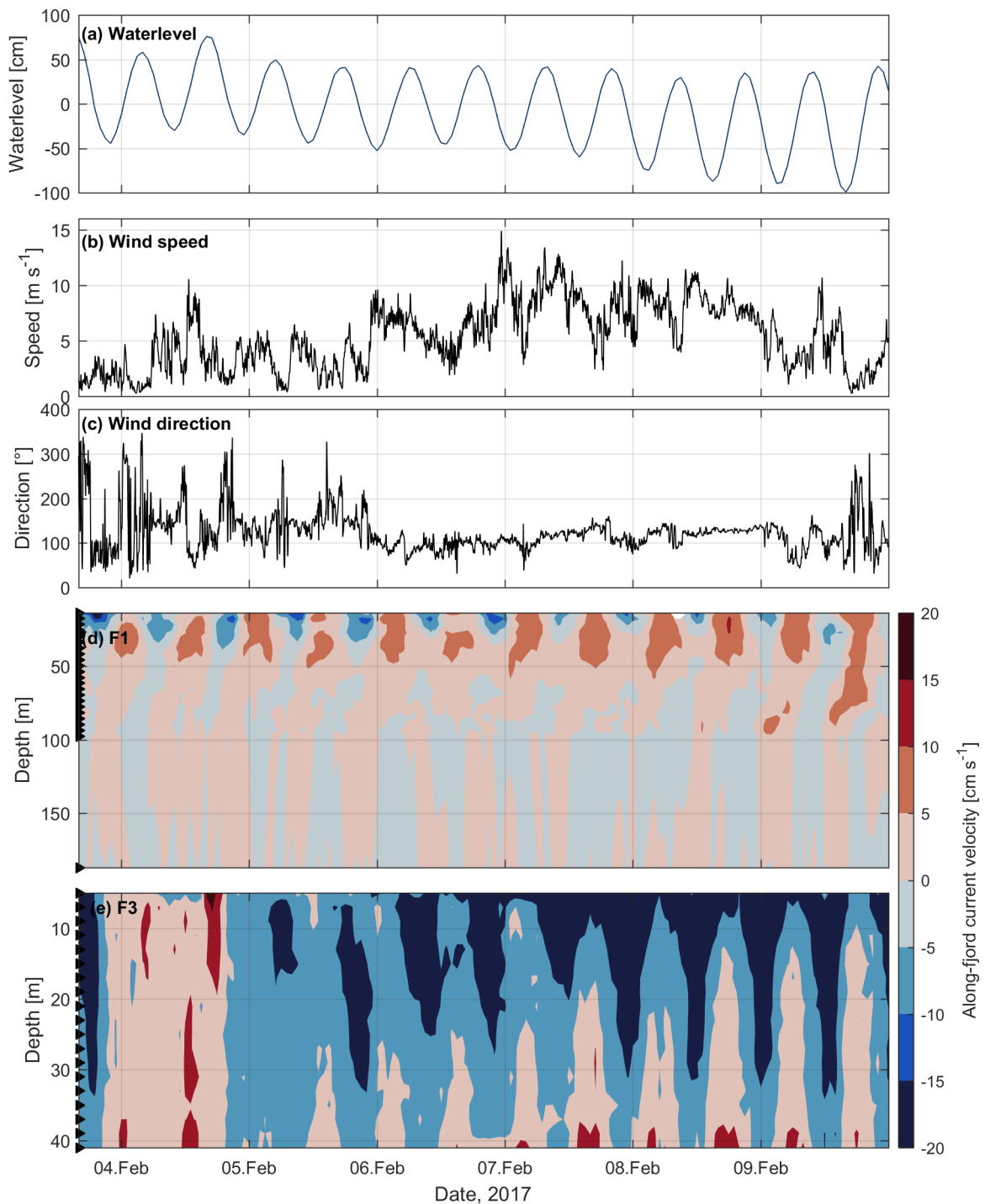


**Figure 5.17** – Time series of (a) water level at the Ålasund, (b) wind speed and (c) wind direction measured by ship, (d) total along-fjord velocity at F1, and (e) total along-fjord velocity at F3. The along-fjord current is represented by the north component at mooring F1 and the east component at mooring F3. The directions at mooring F1 is reversed, which means that positive (red) and negative values (blue) for both moorings indicate in-fjord and out-fjord directed current, respectively. The black triangles on the vertical axis in panel (d) and (e), indicate the depths of velocity measurements. Note that the vertical depth range is not the same in the panels. 0° and 360° indicate wind from the north, and 90° indicate wind from the east.

### 5.6.2 Deposit site

From February 19 to March 1, the vertical displacement of temperature surfaces at mooring F5 increases (Figure 5.18). At the same time, strong winds are measured at the Ytterøyane Lighthouse. In addition, the temperature surfaces fluctuate with a longer period, approximately 48 hours, as opposed to the 12 hour period usually observed in association with the semidiurnal tide. The largest displacements are seen toward the bottom (232 m depth), on February 28, when there are three large vertical isothermal displacements. At the same time, the water level at the surface has a range of approximately 1.5 m, and the surface current is directed out-fjord, while the current at 81 m depth is directed in-fjord. The same isothermal displacements are not observed at mooring F4, and the record at F1 ended on February 21, prior to the event. However, the temperature increased at moorings F2 and F3 in the same period (Figure 5.3).

In the same time period, from February 19 to March 1, the tidal currents are weak (neap tide in the Førdefjord, Figure 4.3), and strong winds of variable direction are observed at the Ytterøyane Lighthouse (Figure 4.2). Over a two day period (from February 20 to February 22), strong winds, of approximately  $12 \text{ m s}^{-1}$ , are directed in-fjord, followed by strong winds to the north and then to the south. The periodic change in strong wind direction can resonate in the channel-like fjord, which can cause large amplitude seiches. If the duration of the wind event is the same as one of the natural frequencies of the internal seiche modes, resonant amplification of the seiche may occur (Arneborg and Liljebladh, 2001a). The period of the mode one internal seiche for the Førdefjord is calculated from Merian's formula (Equation 2.6), using the phase speed estimated from CTD data obtained close to mooring F5,  $c_1 = 0.63 \text{ m s}^{-1}$ . The seiche period is 22 hours. Since this is a semi-enclosed basin the oscillation period will be twice the natural oscillation period, approximately two days, which is the same period as the wind event. Hence, resonance may have occurred and the vertical isotherm displacements observed at mooring F1 can possibly be related to a seiche event.

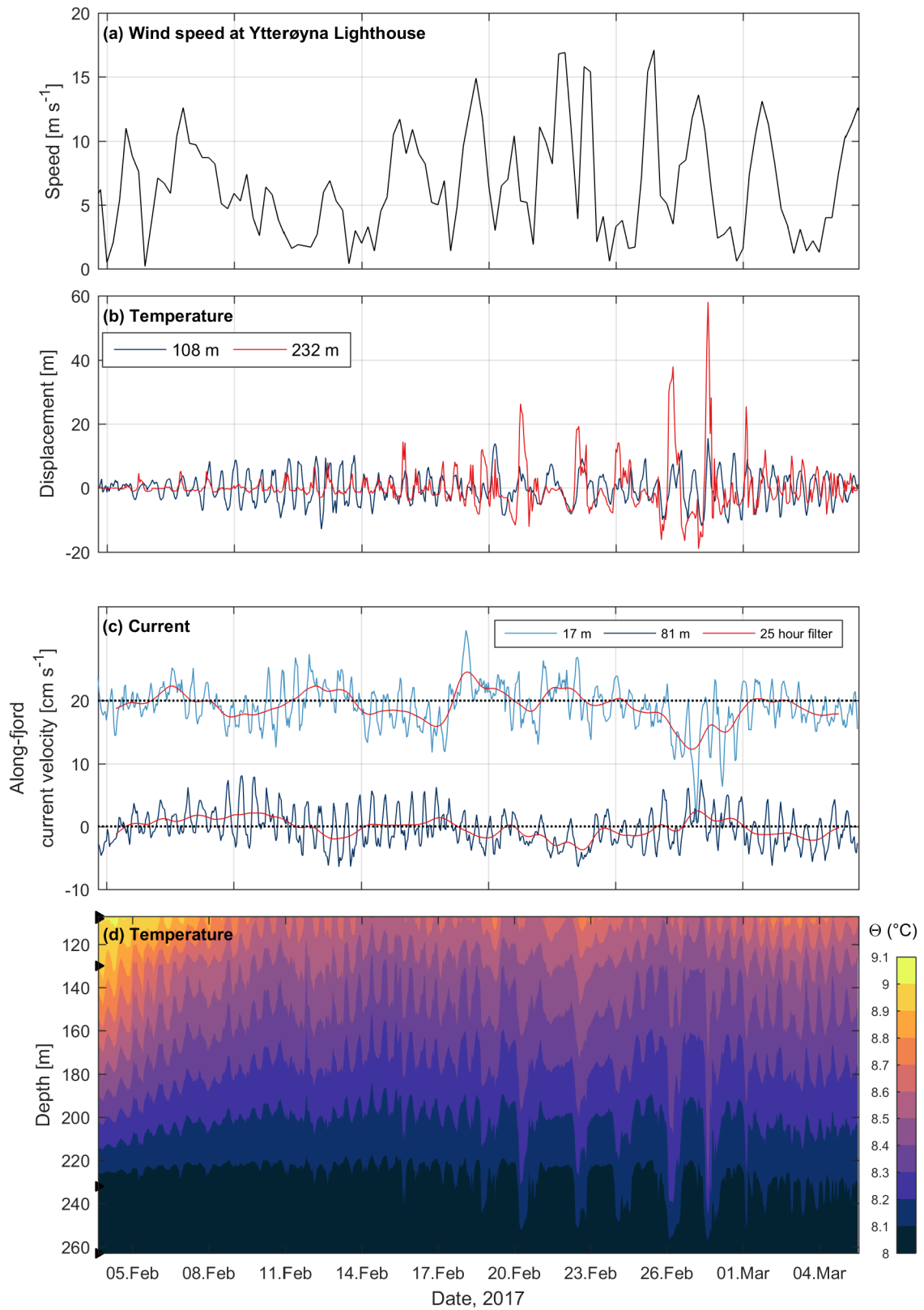


**Figure 5.18** – Time series of (a) wind from the Ytterøyane Lighthouse, (b) isotherm displacement, (c) total along-fjord velocity at 17 m depth (offset of +20) and 81 m depth, and (d) temperature from mooring F5. The along-fjord current is represented by the east component at mooring F5. The black triangles on the vertical axis in panel (d) indicate the depths of temperature recorders.



## 6 | Discussion

The following discussion will focus on how the physical forcings can be related to the observed processes in the Fjørdefjord. The effect of wind and tides cause changes in the hydrography, circulation, and vertical mixing in the fjord. The discussion addresses processes at the Ålasund sill and the suggested deposit site near the Engebø mountain. The effect of flow through a constriction, such as the Ålasund, is of interest with respect to vertical mixing in the fjord. Bottom currents and vertical mixing in the basin close to mooring F5, may lead to re-suspension of mining residual from the future mining activity in the Engebø mountain (Section 2.2.1). The study covers the late winter in the Fjørdefjord, and an attempt is made at evaluating the possibility of processes to occur during other seasons, and under different atmospheric and tidal conditions, than the ones observed in late winter. The main findings that will be discussed here, are the effect of local wind, the effect of non local wind (cold tongue intrusion and the seiche formation), the interaction between the barotropic tide and the sill, and the resulting sill processes in the Ålasund region.

### 6.1 Wind-driven circulation

#### 6.1.1 Surface wind stress

The local wind stress in the fjord acts on the surface water, and initiate currents in approximately the same direction as the wind, due to the narrow width of the Fjørdefjord. If the tidal currents are directed in the same direction as the wind, the currents are amplified by the wind stress, as observed at the Ålasund sill during ebb tide (see Figure 5.17). If the flow conditions at the Ålasund sill are near critical (Froude number approaching unity), an increase in current speeds due to wind stress may lead to supercritical periods. As a consequence, turbulence production at the sill would increase, which could impact the vertical mixing in the basin. It could be speculated that non-linear waves, trapped at the lee side of the Ålasund sill, in response to critical conditions, could be relaxed and left to propagate freely, possibly toward the deposit site, at slack tides. Such events have been reported in other fjord systems, such as the Knight Inlet (Farmer and Armi, 1999a,b; Cummins et al., 2006). Local wind data is only available during the cruise period, and the wind

direction at the Ytterøyane Lighthouse might not be representative for the wind condition in the fjord, therefore conclusions to other time periods cannot be made. However, it is likely that the effect of local wind, when aligned with the surface current, could lead to near-critical conditions at the sill during spring tides when the currents are stronger.

Surface wind stress may cause vertical mixing between the fresh surface layer and the layer below. The effect of vertical mixing by the wind stress in the Førdefjord, is seen in the downward tilt of the pycnoclines toward the mouth (Figure 4.5). The surface mixed layer deepens toward the mouth due to entrainment of the dense water below. The density in the water column decreases, facilitating deep water renewals.

### 6.1.2 Cold tongue intrusion

Strong northward winds were recorded at the coast at the Ytterøyane Lighthouse, prior to the student cruise in February 2017. Along the western coast of Norway, northward winds lead to Ekman transport of the surface water toward the right, which will cause a downwelling at the coast (Gill, 1982). If the coastline is interrupted by a fjord mouth, an in-fjord transport of the surface layer may occur, compensated by an out-fjord current in the deeper intermediate layer (Svendsen and Thompson, 1978; Asplin et al., 1999). Previous studies have shown that there is a significant exchange of water between the coast and fjords along the Norwegian coast, driven by e.g. wind, tides, and freshwater runoff (Svendsen and Thompson, 1978; Klinck et al., 1981; Aure et al., 1996). Svendsen and Thompson (1978) demonstrated that the coastal and local winds are an important forcing for the stratification outside the fjord mouth, and for the circulation in the surface and intermediate layer in the Jøsenfjord, in south-western Norway. They observed that during one week, all the water above sill level in the fjord was flushed out due to downwelling at the coast. It is also shown that the volume fluxes due to intermediary circulation can be significantly larger than the fluxes expected from the classical estuarine circulation (Asplin et al., 1999).

The effect of non-local wind in the Førdefjord is observed in the CTD transect, when a cold tongue enters the fjord at 50 m depth, stretching from the coast to the Ålasund (Figure 4.5). Prior to the cold tongue event, strong northward winds are observed at the Ytterøyane Lighthouse. The cold tongue is centred at a depth of 50 m, which is deeper than the typical Ekman depth. The Ekman transport is generated and strongest at the surface, and may effect the water down to 50 m depth, depending on the strength and duration of the wind (Gill, 1982). The intrusion of the cold tongue might therefore be a result of stratification differences between the coast and the fjord, aided by non-local winds. The difference in density between the coastal water and the fjord water induces horizontal pressure gradients, and consequently currents between the two locations, termed the intermediary

water exchange (Aure et al., 1996; Stigebrandt, 2012).

The surface water inside the fjord (upper 10 m), is significantly colder and fresher than the cold tongue, and must originate from the fjord. At the time when the transect was obtained, westward wind was recorded by the ship, which might indicate that the surface layer is directed out-fjord due to local wind stress. This leads to the conclusion that the cold tongue is directed in-fjord due to non-local wind forcing at the coast, and submerges under the surface layer directed out-fjord forced by local wind. Consequently, we observe an intermediary circulation in the Førdefjord at this time, and the water above sill level in the fjord is renewed. The response to a wind event can be rapid. Asplin et al. (1999) used an idealized model of the Masfjord, located on the western coast of Norway, to show that approximately 50% of the upper water layer was replaced within 1 to 2 days. Observations from the environmental assessment by (Endresen et al., 2014), show that the outer part of the Førdefjord experiences reoccurring renewals of the fjord water throughout the year. Strong northward winds on the west coast of Norway are not uncommon, and it is therefore likely that this process keeps the outer part of the Førdefjord, above sill level, well ventilated.

### 6.1.3 Seiche event

In fjords during neap tides, when the tidal forcing is weak, winds might play a more dominating role (Arneborg and Liljebladh, 2001a). If the frequency of the wind forcing and the natural frequency of the mode one internal seiche are approximately the same, resonance occurs and oscillations along the pycnocline start to form, resulting in internal seiches (Boegman and Ivey, 2012). A possible internal seiche event is observed in the Førdefjord at mooring F5 during neap tides, when the tides are weak (see Section 5.6.2). The period of oscillations in the wind forcing and the natural frequency of the basin coincide, and so does the period of vertical isotherm displacements of approximately 48 hours (Figure 5.18). Vertical isotherm displacements are largest at depth, where the stratification is weaker, and vertical displacements of 60 m are observed (Figure 5.1). The same vertical displacements and oscillations of the isotherms are not observed at other moorings, as mooring F1 stopped recording before the seiche event, and mooring F4 across the sill maintain a period of 12 hours throughout the measurement period. Internal seiches may contribute significantly to the energy available for turbulence and mixing in the fjord, as observed by Arneborg and Liljebladh (2001a) and Arneborg and Liljebladh (2001b) in the Gullmar fjord in Sweden. In the Gullmar fjord the tides are weak, and other motions, such as a seiche, can therefore be observed, as is the case during neap tides in the Førdefjord. Also, when resonance occurs, Boegman and Ivey (2012) showed that progressive non-linear internal waves formed on the internal seiche in a lake, and large amplitudes

caused Kelvin-Helmholtz instabilities to grow within the troughs, causing significant local diapycnal mixing within the interior of the fjord (Boegman and Ivey, 2012).

We do not observe a surface seiche in the Førdefjord. The speed of a surface seiche is considerably faster than the internal phase speed, and the surface seiche period of oscillation is 17 minutes, assuming a constant depth of 250 m in the Førdefjord (Equation 2.6). A surface seiche period is considerably shorter than the period of oscillation for the internal seiche. The meteorological station at the Ytterøyane Lighthouse provides measurements in 6-hour intervals, and can not be related to the period of oscillation for the surface seiche. However, we do not expect strong wind variability and resonance at one hour time scale, supporting the lack of surface seiche.

The occurrence of seiches will vary during the year, since the natural frequencies of seiches change according to the stratification, and since the forcing frequency is also variable. The phase speed of the first baroclinic mode during summer, is twice that during late winter, which would result in an oscillation period of the internal seiche of 20 hours in the fjord. If weak tides and strong, periodic wind with a frequency of 20 hours is observed, seiche events could also occur during summer.

## 6.2 Tidal forcing

In late winter, the tides dominate the current variability in the Førdefjord, supported by the findings in the environmental assessments by Sundfjord and Bjerkgeng (2008) and Endresen et al. (2014). Along the Norwegian coast, the  $M_2$  tide is the strongest tidal component (Kartverket, 2018), which is also observed by Staalstrøm et al. (2012) in the Oslofjord. The dominating tidal component is the semidiurnal tide,  $M_2$ , with a period of 12.42 hours. The Førdefjord is classified as narrow, since the width of the fjord is less than the Rossby radius of deformation (Cusman-Roisin et al., 1994). Consequently, the cross-fjord velocities are weak, as observed in the tidal ellipses in Figure 5.10 and Figure 5.11. The tides cause a complete reversal of the current direction approximately every 12 hours, mainly directed in-fjord and then out-fjord.

### 6.2.1 Tidal currents across the Ålasund

As the tide propagates in- and out-fjord, flow through a constriction alters the currents, and initiates processes at the Ålasund sill. Energy is extracted from the barotropic tide at a constriction, and a change in tidal elevation, or phase, is expected (Stigebrandt, 1980). However, no significant change in tidal amplitude, or phase, is observed across the sill, from moorings F1 to F4 (Figure 5.16), except for a small decrease in tidal elevation of approximately 5 cm. A possible reason for the lack of phase change across the sill, is that



the distance between the two moorings, 2 km, is much shorter than the wavelength of the barotropic  $M_2$  tide, 2000 km.

Instead of changes in tidal elevation, or phase, higher harmonics are energized as the tide crosses the Ålasund (observed in the frequency spectra in Figure 5.7). The velocity spectra from mooring F4, show energy peaks at harmonic overtones of the  $M_2$  tide, such as the  $M_4$  and  $M_6$  (also observed in the tidal ellipses in Figure 5.10 and Figure 5.11). In addition, there is an increase in energy in the frequency band between 1 and 3 cph. This suggests that the barotropic tide interacts with the sill, and generates internal tides of higher harmonics, and that there is an energy cascade toward higher frequencies. Sill processes are further discussed in Section 6.3.

### 6.2.2 The barotropic tide

The barotropic current is normally directed in-fjord during flood tide, and out-fjord during ebb tide as the tide enters and leaves the fjord. This is observed in the barotropic current at mooring F5. However, at moorings F1 and F4 the barotropic tidal signal is different. Moorings F1 and F4 represent the western (out-fjord) and eastern (in-fjord) side of the Ålasund, respectively. West of the sill, the barotropic current changes direction four times during one tidal cycle, which means that both in-fjord and out-fjord currents are observed during both flood and ebb tide. While east of the sill, the strongest barotropic currents are observed before and after low tide (Figure 5.15f-g). The barotropic current is directed in-fjord at the end of ebb tide and out-fjord at the beginning of flood tide, and in between, the barotropic current is weak.

It is customary in physical oceanography to estimate the barotropic current from depth averaging. However, when the contribution of internal tides are substantial, this method can be biased. Here, we used instead the zero-crossing of the vertical shape of the first baroclinic mode of horizontal currents (typically, away from generation sites, baroclinic tides are low mode). By definition, at the zero-crossing, the contribution of the first mode internal tide is zero, and the measurements would be representative of the barotropic currents. However, our observations are close to possible internal tide generation sites, and higher harmonics (possibly higher vertical modes) are also observed, casting doubt on the barotropic estimates. The two methods give different estimates of barotropic currents at each mooring (not shown). The barotropic currents calculated from the two methods at mooring F5 are different in both pattern and strength. At mooring F1 the barotropic current is approximately the same for the two methods, and at mooring F4 the pattern is approximately the same, but the strength of the barotropic current is weaker for the depth averaged current, especially during spring tides.

### 6.2.3 The baroclinic tide

The strongest baroclinic tidal currents are recorded during spring tides in the Førdefjord. The baroclinic signal is different on either side of the Ålasund sill (Figure 5.16 in Section 5.5). Note that the baroclinic currents are approximated as the residual from the total current after removing the barotropic current, as described above. Uncertainties can thus be large (unquantified) if the dominant baroclinic structure is not the first mode. Physical interpretations of the following observations are therefore uncertain.

On the western side of the sill, at 80 m depth, the strongest out-fjord and in-fjord currents are observed 1 and 6 hours before high tide, respectively. The baroclinic currents are approximately  $180^\circ$  out of phase with the surface elevation, and are directed in-fjord during most of the tidal cycle, except for a 4 hour window of out-fjord baroclinic current centred at 1 hour before high tide. At shallower depths (40 m), the baroclinic currents are stronger, and oppositely directed compared to at 80 m depth. The strongest out-fjord and in-fjord currents are observed 4 and 8 hours before high tide, respectively. The surface current is approximately  $90^\circ$  out of phase with the surface elevation. As a result, the currents at the surface are directed out-fjord during ebb tide and in-fjord during flood tide.

On the eastern side of the sill, baroclinic records are only available below 80 m depth, and we are therefore not able to resolve the uppermost layers. However, the baroclinic currents at 80 m depth are different than at the same depth on the western side. The tidal phase shows that the strongest out-fjord and in-fjord currents are observed 5 and 8 hours after high tide, respectively (Figure 5.15). This means that the strongest baroclinic currents are recorded as the tide turns from ebb to flood tide, and in between, the currents are weak and directed out-fjord.

The baroclinic currents at 80 m depth, on either side of the sill, are oppositely directed during ebb tide. On the western side the currents are directed in-fjord, while on the eastern side the currents are directed out-fjord. At the beginning of flood tide, the baroclinic currents on the western and eastern side of the sill are directed in-fjord, while weak out-fjord currents are recorded towards the end of flood tide. Again, our estimation of the barotropic tidal currents might not be representative, and could be affecting the baroclinic currents.

## 6.3 Processes at the sill

The processes by which energy is extracted from the barotropic tide at the sill, are important for currents and vertical mixing in the fjord. Energy from the barotropic tide can be extracted at the sill in three ways; friction against the boundaries, baroclinic wave drag, and barotropic form drag (Stigebrandt, 1999b) (Section 2.1.2). The dominating processes that occur at the sill can be determined by calculating the Froude number (Stigebrandt

and Aure, 1989). The estimated Froude number in the Førdefjord is below unity for the study period (Figure 5.14), classifying the Førdefjord as a wave fjord. This means that the current velocity is weaker than the phase speed of the first mode internal wave, estimated from the stratification. The fjord is in an internal wave regime, and the barotropic energy loss at the sill is dominated by baroclinic wave drag and internal tide generation. The classification of fjords into either jet- or wave regimes, based on their Froude number, is not necessarily mutual exclusive. Other studies have found that fjords can be both a wave and a jet fjord simultaneously (Inall et al., 2004; Stashchuk et al., 2007). The regime at the sill determines which processes will occur, and is important with respect to mixing. A jet fjord is efficient at mixing locally, but overall in the fjord system, efficiency of mixing is larger in a wave fjord. Local mixing near the sill homogenize the water column and consequently predispose the basin to deep water renewal, while non-local mixing may cause re-suspension of particles from the mining residual at the deposit site. The effect of sill processes on mixing is not resolved in the mooring observations, however, detailed turbulence measurements collected during the cruise (see (GEOF337 Students, 2017)), captured energetic mixing events. In the following, the microstructure (MSS) data from the cruise is shown to exemplify the dissipation rates in the Førdefjord.

MSS and CTD data show high dissipation rates and formations of hydraulic jumps in the Ålasund region, which could indicate that the fjord is in a jet-regime, oppositely to the conclusions drawn from the Froude number classification. Espenes et al. (2017) (student cruise report) used MSS profiles obtained during the cruise, to estimate the dissipation rate of turbulent kinetic energy,  $\epsilon$ . They concluded that the dissipation rates were generally low west of the Ålasund sill, while the sill was characterised by a lee-side hydraulic jump during flood tide (Espenes et al., 2017). This is illustrated by a MSS section obtained across the sill on February 9, during flood tide (lower panel in Figure 6.1). High dissipation rates are measured on the lee-ward side, and the density surfaces are displaced downward before they abruptly rebound. The same is observed in the Oslofjord and in the Knight Inlet, where Staalstrøm et al. (2015) and Klymak and Gregg (2004) calculated dissipation rates of the same order of magnitude as in the Førdefjord. At ebb tides, the currents are directed out-fjord, and the dissipation rates are significantly lower (upper panel in Figure 6.1). A potential hydraulic jump cannot be resolved in the mooring data set, but indications of a hydraulic jump is observed in the CTD data presented in Section 4.3.2 (Figure 4.5). The  $\sigma_{\theta} = 26.5 \text{ kg m}^{-3}$  isopycnal drops 30 m across the Ålasund, at the start of the flood tide on February 7.

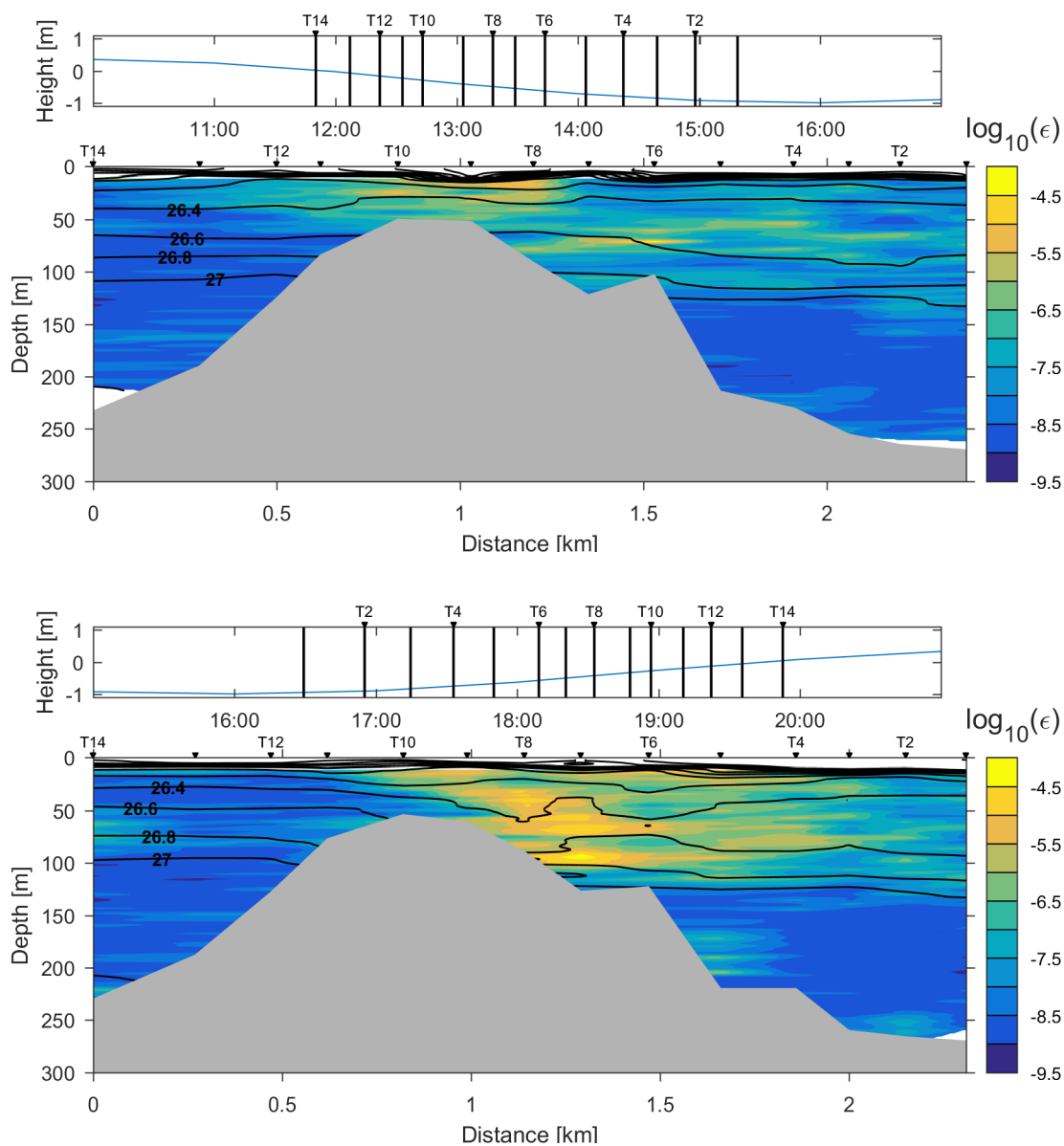


**Figure 6.1** – Along-fjord transect across Ålasund of dissipation rates,  $\epsilon$ , overlain with isopycnals modified from Espenes et al. (2017), on February 9 during (a) ebb tide, and (b) flood tide. Black triangles at the top show the locations of MSS casts. The sill is shown in grey, and the x-axis is the distance from the start of the transect,  $x = 0$  km is west while  $x = 2$  km is east of the sill. The upper panels show a time series of water level during the transect, together with the timing of the MSS casts (vertical lines).

The MSS data is only available during the cruise period, however, an attempt to infer the conditions at other times during the year is given.

The MSS data is obtained during neap tides, when the tidal currents in the fjord are weak. Still, the high dissipation rates recorded at neap tides, might indicate that the dissipation is even higher during spring tides when the currents are stronger. The stronger currents observed at spring tides in the mooring data set, means that the Froude number would be higher at this time (as observed in Figure 5.14 in Section 5.5.1). Higher Froude

numbers may lead the fjord into a supercritical state at spring tides, with increasing dissipation rates. The highest dissipation rates occur close to the sill, with the possible formation of hydraulic jumps and jets. However, our Froude number calculations (Figure 5.14), remain below unity also during spring tides, which could imply that the estimation of the phase speed is not correct. The phase speed used in the calculation, is sensitive to changing stratification and water depth, and might not be representative for the actual conditions in different parts of the fjord, or for the whole measurement period. In addition, the Froude numbers are calculated with the phase speed of the first baroclinic mode. Phase speeds of higher modes are smaller, which will yield near-critical or super-critical conditions. The higher harmonics observed on the eastern side of the sill is most likely described by higher vertical modes.

Processes at the sill during other times of the year, e.g. during summer and fall, can be inferred by estimating a hypothetical Froude number. The current measurements from late winter are assumed to be representative for the whole year, and the phase speed can be approximated by Equation 2.3, with summer and fall stratification. The stratification is calculated from CTD data obtained by NIVA (October, 2007) and DNV (July, 2013), close to the deposit site, and mooring F5 (Figure 2.2). The phase speeds are  $c_1 = 1.46 \text{ m s}^{-1}$  and  $c_1 = 1.35 \text{ m s}^{-1}$ , in July and October, respectively. For validation purposes, applying the same equation to the CTD data obtained at mooring F5 during the cruise, gives a phase speed that is 10% larger than the phase speed obtained by normal mode analysis. The phase speeds during summer and fall are higher than in late winter, as the surface layer is thicker during summer due to increased river run-off and heating at the surface. The summer surface layer is approximately 80 m deep, and during winter it is 15 m deep. Consequently, the Froude numbers, calculated with summer stratification and winter current measurements, are lower at other times of the year. This indicates that the potential for supercritical conditions in the Førdefjord during summer is low.

## 6.4 Processes at the deposit site

At mooring F5, located close to the deposit site, the bottom currents do not exceed  $6 \text{ cm s}^{-1}$  during the study period (Figure 5.4). Previous results from the environmental assessments by DNV and NIVA (Endresen et al., 2014; Sundfjord and Bjerkeng, 2008), using observations from approximately the same month and location as our data, show a mean speed of  $5 \text{ cm s}^{-1}$  and  $3.5 \text{ cm s}^{-1}$ , respectively. In late winter, the mean current direction at the deposit site is out-fjord in the deep basin and at the surface, while at mid depth (50 m) the mean current is in-fjord (Figure 5.5). The weak currents recorded in late winter indicate that there is little movement at the suggested deposit site. This leads to the conclusion that the currents have a low impact on the mine tailings, which supports the conclusions

from the environmental assessments by DNV and NIVA.

The internal waves, generated by the interaction of the barotropic tide with the sill, may cause turbulence and vertical mixing as they encounter critical slopes at the boundaries of the fjord (Section 2.1.2). If the topographic slope has the same slope as the internal wave beams, the slope is critical. In the Førdefjord, the slope of the internal wave beams are estimated for  $M_2$  internal tides generated at the sill and in a continuous stratification (Equation 2.9). The Førdefjord has few areas of critical slopes (not shown), in most places the slope of the internal wave beam is steeper than the slope of the bottom topography. The result is subcritical slopes, where the internal waves are reflected onshore, and limited energy is available for turbulence and mixing in the basin. It is therefore not likely that internal waves that encounter fjord boundaries in the vicinity of the deposit site, contribute to re-suspension of the mining residual. However, considerable vertical isotherm displacements are observed in the region at mooring F5 during neap tides.

The study period is short and only covers late winter in the Førdefjord, and the spatial coverage is also limited (e.g. lacking uppermost layer at mooring F4). Therefore some of the conclusions drawn in this chapter, especially with respect to the deposit site and surface currents east of the sill, remain uncertain, and the variability is unresolved.

## 7 | Conclusions

The late winter conditions in the Førdefjord are investigated using data from five moorings, deployed between February 3 and March 5, 2017. In addition, hydrographic and microstructure data, obtained during the deployment cruise (February 2-10, 2017), are utilized. The fjord has attracted attention because of the planned mining activity in the Engebø mountain, and the associated deposition of mine tailings in the Førdefjord. The response of the Førdefjord to atmospheric and tidal forcing has been discussed, with a special focus on the Ålasund sill region and the suggested deposit site.

The hydrography in the Førdefjord is characterized by a thin, fresh and dynamic surface layer, and a deep, quiescent layer below. The currents in the fjord are generally weak, but the strongest currents are recorded at the surface and in the vicinity of the Ålasund sill during spring tides. The Førdefjord is a narrow fjord, and the strongest currents are observed in the along-fjord direction, while the cross-fjord currents are weak. Tides dominate the current variability in the fjord, and the semidiurnal  $M_2$  tide is the dominating constituent.

Two distinct effects of non-local winds are observed. Intrusions of cold intermediate layers, extending to the inner part of the fjord, are forced by northward wind at the coast, and by changing stratification of the coastal water. This implies regular and frequent ventilation of the intermediate layer in the outer part of the Førdefjord. The second effect is the resonance of long internal waves and wind variability, leading to internal seiches during favourable conditions (weak tides combined with strong, periodic wind). One such example event is documented at the deposit site during neap tides, with vertical isotherm displacements of 60m amplitude, and a period of 48 hours in the deeper part of the water column.

In late winter, the Førdefjord is classified as a wave fjord. Internal tides, of semidiurnal frequency, are generated by the interaction of the barotropic tide with the Ålasund sill, in addition to overtides of higher harmonics, such as the  $M_4$  and  $M_6$  tide. The higher frequency associated with slower phase speeds, can lead to supercritical conditions leading to hydraulic jumps and energetic turbulence, as observed on the leeward side of the sill during flood tide. Favourable wind direction may accelerate the mean current, which can help approach and maintain such critical conditions, leading to increased mixing during

flood, in spring tides.

Several studies have been conducted in the Førdefjord, and most of them conclude, including this thesis, that the currents in the deep basin close to the deposit site are weak. However, this thesis show that processes that occur elsewhere in the fjord, may influence the deposit site. To my knowledge, these processes have not been previously studied in the Førdefjord. However, the data set in this thesis is not able to fully resolve all the features at the deposit site, and conclusions remain uncertain. Future studies, specifically designed to investigate how processes occurring elsewhere influence the deposit site, could provide a better understanding of the potential for re-suspension of mine tailings. Data that could be relevant in this regard, is current measurements covering the entire water column, local wind data in the Førdefjord, and observations from different seasons. Also, when the mining project starts, the behaviour of the mine tailings at the deposit site could be monitored, in order to investigate if the sediments influence the marine life in the Førdefjord.



## 8 | Bibliography

- Aanderaa Data Instruments AS (2008). TD 273 Operating Manual. Technical report, Aanderaa Data Instruments AS, Bergen, Norway. pp. 1-55.
- Arneborg, L. and Liljebladh, B. (2001a). The Internal Seiches in Gullmar Fjord. Part I: Dynamics. *Journal of Physical Oceanography*, 31:2549–2566.
- Arneborg, L. and Liljebladh, B. (2001b). The Internal Seiches in Gullmar Fjord. Part II: Contribution to Basin Water Mixing. *Journal of Physical Oceanography*, 31:2567–2574.
- Asplin, L., Vea, A. G., and Bent, J. B. (1999). Nonlocal wind-driven fjord-coast advection and its potential effect on plankton and fish recruitment. *Fisheries Oceanography*, 8(4):255–263.
- Aure, J., Molvær, J., and Stigebrandt, A. (1996). Observations of Inshore Water Exchange Forced by a Fluctuating Offshore Density Field. *Marine Pollution Bulletin*, 33:112–119.
- Boegman, L. and Ivey, G. N. (2012). The dynamics of internal wave resonance in periodically forced narrow basins. *Journal of Geophysical Research*, 117:1–16.
- Cummins, P. F., Armi, L., and Vagle, S. (2006). Upstream Internal Hydraulic Jumps. *Journal of Physical Oceanography*, 36(5):753–769.
- Cushman-Roisin, B. and Beckers, J. M. (2011). *Introduction to geophysical fluid dynamics: physical and numerical aspects*. Academic Press, 2 edition.
- Cushman-Roisin, B., Asplin, L., and Svendsen, H. (1994). Upwelling in broad fjords. *Continental Shelf Research*, 14(15):1701–1721.
- Drageset, T. A. (2000). Flomberegning for Jølstra. Technical report, Norges vassdrags- og energidirektorat (NVE), Oslo, Norway. [http://publikasjoner.nve.no/dokument/2000/dokument2000\\_06.pdf](http://publikasjoner.nve.no/dokument/2000/dokument2000_06.pdf) [Online; accessed 5-12-2017] pp. 1-34.
- Ekman, F. L. (1875). Om de strømninger som oppstå i nærheten af flodmynningar etc. *Ofvers, K. Vetensk. - Akad. Forhandlingar*.
- Ekman, V. W. (1905). On the influence of the earth's rotation on ocean currents. *Archives of Mathematics, Astronomy and Physics*, 2(11):1–53.

- Endresen, Ø., Gletten, T., and Volan, C. (2014). Strømforhold og partikkelspredning i Førdefjorden. Technical report, DNV GL. [http://www.nordicmining.com/getfile.php/134816-1412582788/Bilder/Operations/Engb%C3%B8/Engb%C3%B8%20norsk/Tilleggsunders%C3%B8kelser/Str%C3%B8mforhold%20og%20partikkelspredning%20i%20F%C3%B8rdefjorden\\_DNV%20GL.pdf](http://www.nordicmining.com/getfile.php/134816-1412582788/Bilder/Operations/Engb%C3%B8/Engb%C3%B8%20norsk/Tilleggsunders%C3%B8kelser/Str%C3%B8mforhold%20og%20partikkelspredning%20i%20F%C3%B8rdefjorden_DNV%20GL.pdf) [Online; accessed 12-12-2017] pp. 1-50.
- Espenes, H., Malila, M., and Vaule, M. (2017). MSS Report, 2017. Technical report, Geophysical Institute, University of Bergen, Bergen, Norway. pp. 1-13.
- Farmer, D. and Armi, L. (1999a). Stratified flow over topography: The role of small-scale entrainment and mixing in flow establishment. *Proceedings of the Royal Society London*, 455(1989):3221–3258.
- Farmer, D. and Armi, L. (1999b). The Generation and Trapping of Internal Solitary Waves over Topography. *Science*, 283(5399):188–190.
- Farmer, D. M. and Freeland, H. J. (1983). The Physical Oceanography of Fjords. *Progress in Oceanography*, 12:147–220.
- Farmer, D. M. and Smith, J. D. (1978). Nonlinear Internal Waves in a Fjord. In Nihoul, J. C. J., editor, *Hydrodynamics of Estuaries and Fjords*, volume 23, pages 465–493. Elsevier.
- Freeland, H. J. and Farmer, D. M. (1980). Circulation and Energetics of a Deep, Strongly Stratified Inlet. *Canadian Journal of Fisheries and Aquatic Sciences*, 37:1398–1410.
- Gade, H. G. (1970). *Hydrographic investigations in the Oslofjord. A study of water circulations and exchange processes*. University of Bergen, Bergen, Norway. pp. 1-193.
- Gade, H. G. (1973). Deep water exchanges in a sill fjord: a stochastic process. *Journal of Physical Oceanography*, 3:213–219.
- Gade, H. G. and Edwards, A. (1980). Deep Water Renewal in Fjords. In Freeland, H. J., Farmer, D. M., and Levings, C. D., editors, *Fjord Oceanography*, pages 453–489. Plenum Publishing Corporation, New York, NY.
- Gemmrich, J. and Klymak, J. M. (2015). Dissipation of Internal Wave Energy Generated on a Critical Slope. *Journal of Physical Oceanography*, 45(9):2221–2238.
- GEOF332 Students (2014). Førdefjorden and Sognefjorden Field work in GEOF332 January 31st - February 5th 2014. Technical report, Geophysical Institute, University of Bergen, Bergen, Norway. pp. 1-91.
- GEOF337 Students (2017). Cruise Report - Cruise KB 2017603 with R.V. Kristine Bonnevie. Technical report, Geophysical Institute, University of Bergen, Bergen, Norway. pp. 1-53.
- Gill, A. E. (1982). *Atmosphere-Ocean Dynamics*. Academic Press, San Diego, CA, USA.

- Gordon, R. (1996). Acoustic Doppler current profiler: Principles of Operation, A Practical Primer. Technical report, RD Instruments, San Diego, California. [http://misclab.umeoce.maine.edu/boss/classes/SMS\\_598\\_2012/RDI\\_Broadband%20Primer\\_ADCP.pdf](http://misclab.umeoce.maine.edu/boss/classes/SMS_598_2012/RDI_Broadband%20Primer_ADCP.pdf) [Online; accessed 15-02-2018] pp. 1-52.
- Helland-Hansen, B. (1906). Current measurements in Norwegian fjords, the Norwegian Sea and the North Sea in 1906. *Bergens Museums Arbok 1907*, 15:1–61.
- Inall, M., Cottier, F., Griffiths, C., and Rippeth, T. (2004). Sill dynamics and energy transformation in a jet fjord. *Ocean Dynamics*, 54(3-4):307–314.
- Inall, M. E. and Gillibrand, P. A. (2010). The physics of mid-latitude fjords: a review. *Geological Society, London, Special Publications*, 344(1):17–33.
- IOC, SCOR, and IAPSO (2010). The international thermodynamic equation of seawater – 2010: Calculation and use of thermodynamic properties. Technical report, Intergovernmental Oceanographic Commission. [http://www.teos-10.org/pubs/TEOS-10\\_Manual.pdf](http://www.teos-10.org/pubs/TEOS-10_Manual.pdf) [Online; accessed 20-02-2018] pp. 1-196.
- Kartverket (2018). Tidevannstabeller for den norske kyst med Svalbard. Technical report, Kartverket, Stavanger, Norway. <https://www.kartverket.no/sehavniva/tidevann-og-vannstand/tidevannstabeller/> [Online; accessed 20-05-2018] pp. 1-90.
- Kleiven, M. (2017). Fakta om Førde - Førde kommune. <https://www.forde.kommune.no/politikk-og-samfunn/om-forde/fakta-om-forde/> [Online; accessed 10-12-2017].
- Klima og Miljødepartementet (2015). Utslippstillatelse til gruvevirksomhet i Engebøfjell. <https://www.regjeringen.no/no/aktuelt/utslippstillatelse-til-gruvevirksomhet-i-engebofjell/id2406887/> [Online; accessed 11-12-2017].
- Klinck, J. M., O'Brien, J. J., and Svendsen, H. (1981). A Simple Model of Fjord and Coastal Circulation Interaction. *Journal of Physical Oceanography*, 11(12):1612–1626.
- Klymak, J. M. and Gregg, M. C. (2004). Tidally generated turbulence over the Knight Inlet Sill. *Journal of Physical Oceanography*, 34(5):1135–1151.
- Leppäranta, M. and Myrberg, K. (2009). *Physical Oceanography of the Baltic Sea*. Springer-Verlag Berlin Heidelberg, Chichester, UK, 1 edition.
- Lesto, A. L. (2016). Fakta om Naustdal - Naustdal kommune. <https://www.naustdal.kommune.no/kommune-og-politikk/om-naustdal/fakta-om-naustdal/> [Online; accessed 10-12-2017].
- Lilly, J. M. (2017). jLab: A data analysis package for Matlab, v. 1.6.5. <http://www.jmlilly.net/jmlsoft.html>. [Online; accessed 13-12-2017].

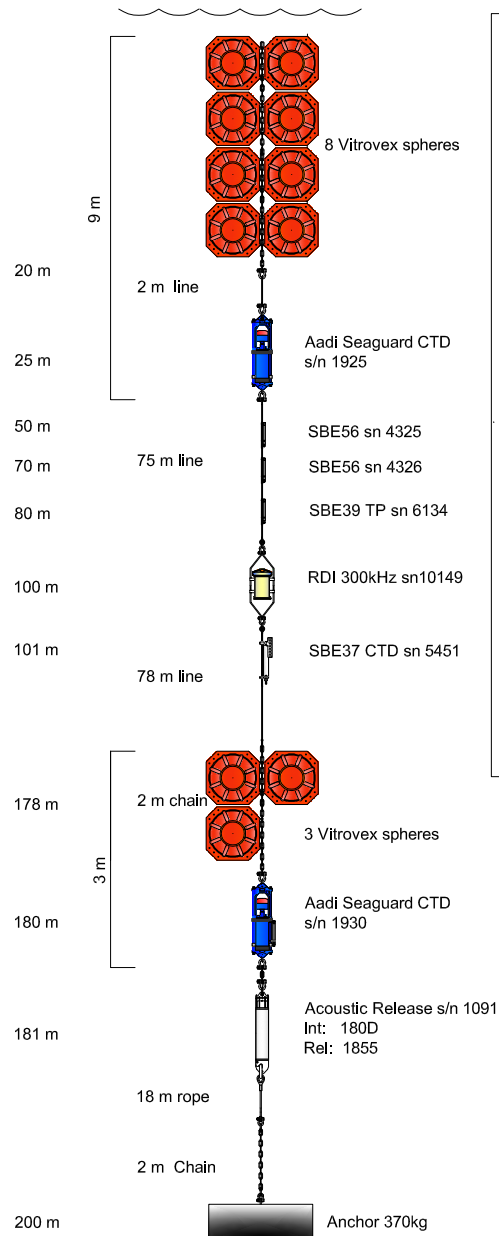
- McDougall, T. and Barker, P. (2011). *Getting started with TEOS-10 and the Gibbs Seawater (GSW) Oceanographic Toolbox*. SCOR/IAPSO WG127. pp. 1-28.
- Nordic Mining ASA (2017). Engebø Project - Nordic Mining. <http://www.nordicmining.com/engebo-project/category317.html> [Online; accessed 11-12-2017].
- Pawlowicz, R., Beardsley, B., and Lentz, S. (2002). Classical tidal harmonic analysis including error estimates in MATLAB using T\_TIDE. *Computers and Geosciences*, 28:929–937.
- Pettersson, L.-E. (2010). Flomberegning for Naustavassdraget. Technical report, Norges vassdrags- og energidirektorat (NVE), Oslo, Norway. [http://publikasjoner.nve.no/dokument/2010/dokument2010\\_14.pdf](http://publikasjoner.nve.no/dokument/2010/dokument2010_14.pdf) [Online; accessed 12-12-2017] pp. 1-21.
- Phillips, O. M. (1977). *The Dynamics of the Upper Ocean*. Cambridge University Press, Cambridge, UK, 2 edition.
- Pugh, D. and Woodworth, P. (2014). *Sea-Level Science: Understanding Tides, Surges Tsunamis and Mean Sea-Level Changes*. Cambridge University Press, Cambridge, UK. pp. 1-407.
- Saelen, O. H. (1967). Some Features of the Hydrography of Norwegian Fjords. In Lauff, G. H., editor, *Estuaries*, pages 63–70. American Association for the Advancement of Science, Washington, DC.
- SINTEF (2017). SINMOD. <https://www.sintef.no/ocean/satsinger/sinmod/{#}Tjenester> [Online; accessed 30-05-2018].
- Staalstrøm, A., Aas, E., and Liljebladh, B. (2012). Propagation and dissipation of internal tides in the Oslofjord. *Ocean Science*, 8:525–543.
- Staalstrøm, A., Arneborg, L., Liljebladh, B., and Broström, G. (2015). Observations of Turbulence Caused by a Combination of Tides and Mean Baroclinic Flow over a Fjord Sill. *Journal of Physical Oceanography*, 45:355–368.
- Stacey, M. W. (1984). The Interaction of Tides with the Sill of a Tidally Energetic Inlet. *Journal of Physical Oceanography*, 14:1105–1117.
- Stashchuk, N., Inall, M., and Vlasenko, V. (2007). Analysis of Supercritical Stratified Tidal Flow in a Scottish Fjord. *Journal of Physical Oceanography*, 37(7):1793–1810.
- Stigebrandt, A. (1976). Vertical Diffusion Driven by Internal Waves in a Sill Fjord. *Journal of Physical Oceanography*, 6:486–495.
- Stigebrandt, A. (1980). Some aspects of tidal interaction with fjord constrictions. *Estuarine and Coastal Marine Science*, 11:151–166.

- Stigebrandt, A. (1999a). Baroclinic wave drag and barotropic to baroclinic energy transfer at sills as evidenced by tidal retardation, seiche damping and diapycnal mixing in fjords. In Muller, P. and Henderson, D., editors, *Dynamics of Internal Gravity Waves, II, Proc. Aha Huliko'a Hawaiian Winter Workshop*, pages 73–82, Honolulu, Hawaii.
- Stigebrandt, A. (1999b). Resistance to Barotropic Tidal Flow in Straits by Baroclinic Wave Drag. *Journal of Physical Oceanography*, 29:191–197.
- Stigebrandt, A. (2012). Hydrodynamics and circulation of fjords. In Bengtsson, L., Herschy, R. W., and Fairbridge, R. W., editors, *Encyclopedia of Lakes and Reservoirs*, pages 327–344. Springer Science + Business Media B.V.
- Stigebrandt, A. and Aure, J. (1989). Vertical Mixing in Basin Waters of Fjords. *Journal of Physical Oceanography*, 19:917–926.
- Sundfjord, A. and Bjerkgang, B. (2008). Strøm, turbiditet og hydrografi i fjordbassenget utenfor Engebø, Førdefjorden. Målinger utført for konsekvensutredning for deponi av gruveavgang. Technical report, NIVA. [https://www.naustdal.kommune.no/\\_f/p1/i73a808e1-7a26-4e95-b5c1-098562f15bdd/3\\_stroem-turbiditet-og-hydrografi-i-fjordbassenget-utenfor-e.pdf](https://www.naustdal.kommune.no/_f/p1/i73a808e1-7a26-4e95-b5c1-098562f15bdd/3_stroem-turbiditet-og-hydrografi-i-fjordbassenget-utenfor-e.pdf) [Online; accessed 12-12-2017] pp. 1-36.
- Svendsen, H. and Thompson, R. O. R. Y. (1978). Wind-Driven Circulation in a Fjord. *Journal of Physical Oceanography*, 8:703–712.
- Thomson, R. E. and Emery, W. J. (2014). *Data Analysis Methods in Physical Oceanography*. Elsevier, Amsterdam, The Netherlands, 3 edition.
- Thorpe, S. A. (1974). Near-resonant forcing in a shallow two-layer fluid: A model for the internal surge in Loch New? *Journal of Fluid Mechanics*, 63(3):509–527.
- Tinis, S. W. and Pond, S. (2001). Tidal Energy Dissipation at the Sill of Sechart Inlet, British Columbia. *Journal of Physical Oceanography*, 31(12):3365–3373.
- Tokuyay, T., Constantinescu, G., and Gonzalez-Castro, J. A. (2009). Investigation of Two Elemental Error Sources in Boat-Mounted Acoustic Doppler Current Profiler Measurements by Large Eddy Simulations. *Journal of Hydraulic Engineering*, 135:875–887.
- Urke, H. A. (2008). Oppdrett og fiskeriaktivitet i Førdefjorden. Technical report, NIVA. [https://www.naustdal.kommune.no/\\_f/p1/i11d9f343-1695-4f75-8d6b-ebd061fca6da/21\\_oppdrett-og-fiskeriaktivitet-i-foerdefjorden.pdf](https://www.naustdal.kommune.no/_f/p1/i11d9f343-1695-4f75-8d6b-ebd061fca6da/21_oppdrett-og-fiskeriaktivitet-i-foerdefjorden.pdf) [Online; accessed 10-12-2017] pp. 1-35.
- van der Meeren, T. and Otterå, H. (2011). Vurderinger av data fra tokt samlet inn i Førdefjorden, 3.-6. mars 2011. Technical report, IMR. [https://www.hi.no/filarkiv/2011/03/toktrapport\\_fordefjorden-nr1-2011.pdf/nb-no](https://www.hi.no/filarkiv/2011/03/toktrapport_fordefjorden-nr1-2011.pdf/nb-no) [Online; accessed 12-12-2017] pp. 1-8.

- Vevring og Førdefjorden Miljøgruppe (2016). Fjordaksjonen.org. <http://www.fjordaksjonen.org/> [Online; accessed 11-12-2017].
- Wanis, P. (2013). Design and Applications of a Vertical Beam in Acoustic Doppler Current Profilers. In *Oceans - San Diego, 2013*, pages 23–26, San Diego, CA, USA. IEEE.
- Wiegand, R. C. and Chamberlain, V. (1987). Internal waves of the second vertical mode in a stratified lake. *Limnology and Oceanography*, 32(1):29–42.
- Wuest, A. J. and Farmer, D. M. (2002). Seiches. In Kauffman, G. B., Porter, R., and Ogilvie, M., editors, *McGraw-Hill Encyclopedia of Science & Technology*, pages 1–8. McGraw-Hill, New York, NY, 9 edition.

# **Appendix**

## **Schematic of the mooring set up**



UNIVERSITY OF BERGEN  
Geophysical institute

Project: GEOF337 cruise with M/S K.Bonnevie

Location: Førdefjord north of sill

Position: 61N28.202 /5E26.084

Depth: 200 m

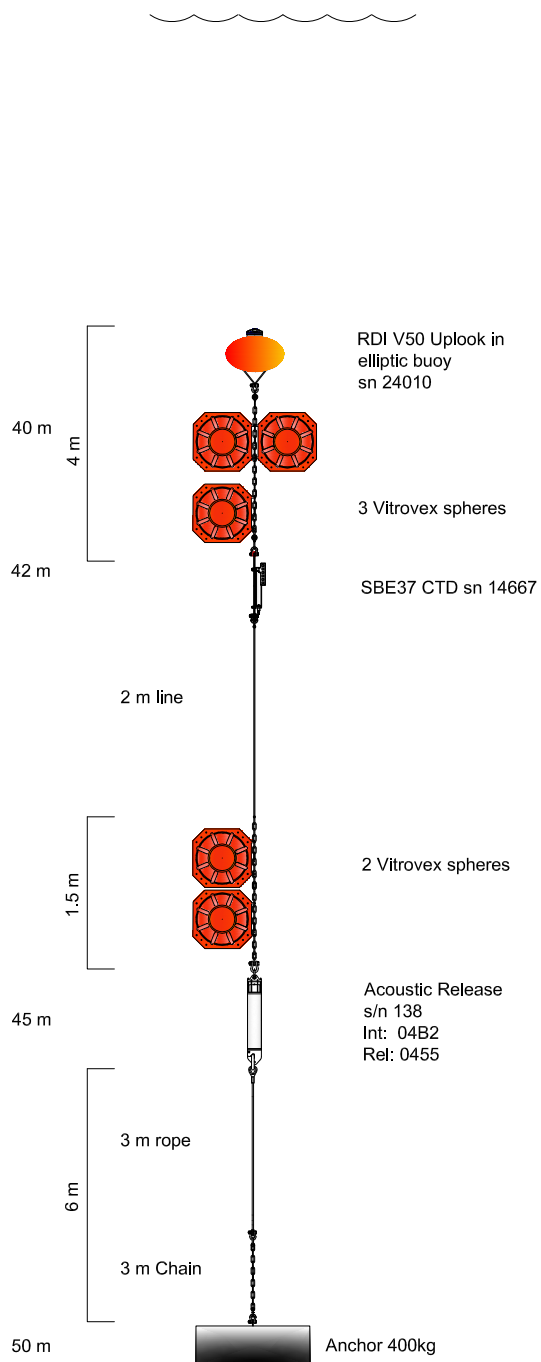
Deployment: 20170203 09:07 UTC

Recover: \_\_\_\_\_

Comments:

**F1**





UNIVERSITY OF BERGEN  
Geophysical institute

Project: GEOF337 cruise with M/S K.Bonnevie

Location: Førdefjord west of sill, Ålasundet

Position: 61N27.622 / 005E26.584

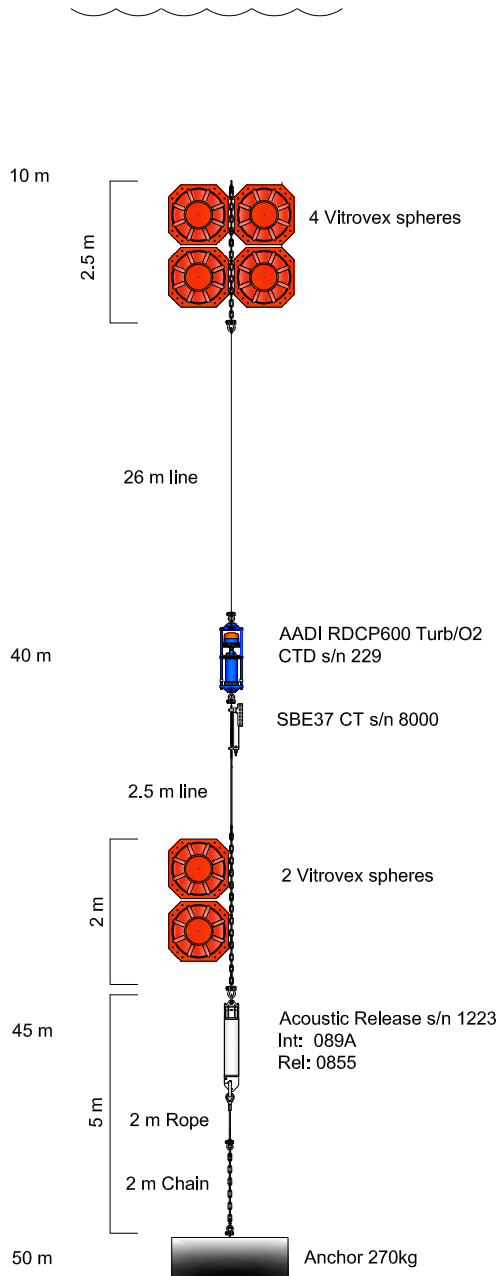
Depth: 50 m

Deployment: 20170203 10:36 UTC

Recover: \_\_\_\_\_

Comments:

F2



UNIVERSITY OF BERGEN  
Geophysical institute

Project: GEOF 337 cruise with M/S K.Bonnevie

Location: Førdefjord east of sill, Ålasundet

Position: 61N27.632 / 005E26.935

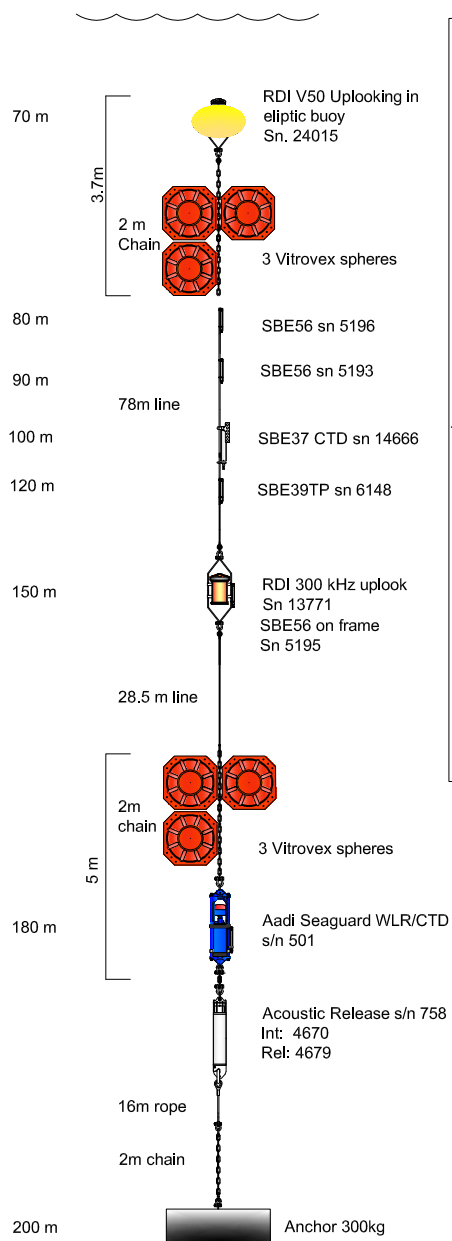
Depth: 50 m

Deployment: 20170203 11:51 UTC

Recover: \_\_\_\_\_

Comments:

**F3**



UNIVERSITY OF BERGEN  
Geophysical institute

Project: GEOF337 cruise with M7S K.Bonnevie

Location: Førdefjord, east of Ålasundet

Position: 61N27'666 / 5E27'570

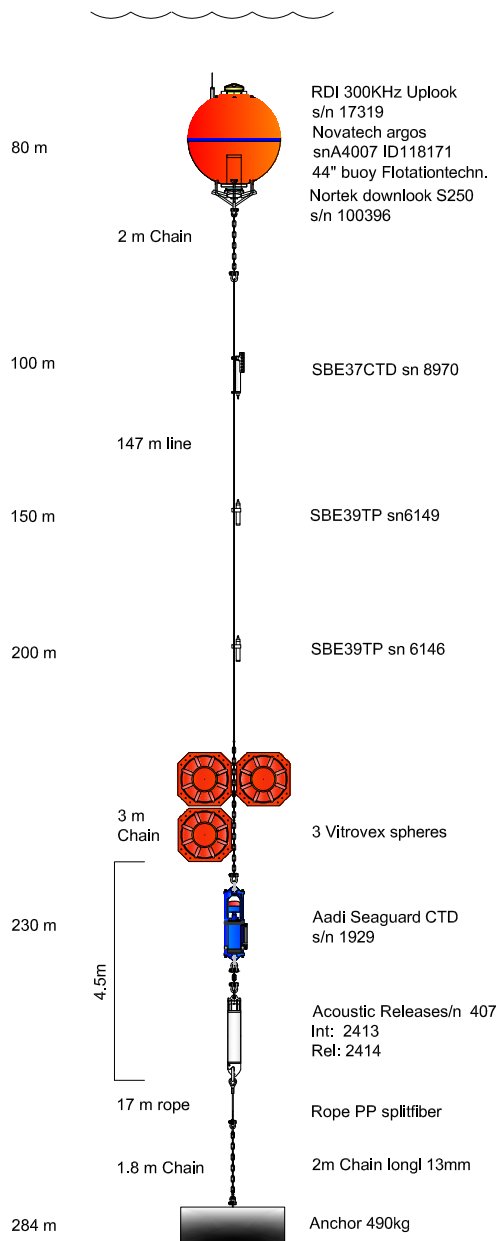
Depth: 200 m


Deployment: 20170203 12:58UTC

Recover: \_\_\_\_\_

Comments:

F4





**UNIVERSITY OF BERGEN**  
Geophysical institute

Project: GEOF337 cruise with M/S K.Bonnevie

Location: Førdefjord at basin north of Ålasundet

Position: 61N29.164 / 5E26.698

Depth: 284 m

Deployment: 20170203 14:28UTC

Recover: \_\_\_\_\_

Comments:

F5